Gonçalo Alexandre dos Santos Marcelo

Licenciado em Ciências da Engenharia Química
e Bioquímica

Synthetic Optimization Process of Mesoporous Nanoparticles for Protein Extraction in Biological Samples

Dissertação para a obtenção do Grau de Mestre em Engenharia Química e Bioquímica

Orientador: Dr. Elisabete Oliveira (FCT/UNL)
Co-orientador: Dr. José Paulo Mota (FCT/UNL)

Composição do Júri:
Presidente de mesa
Prof. Doutor Mário Eusébio (FCT/UNL)
Orientador
Doutora Elisabete Oliveira (FCT/UNL)
Arguente
Prof. Doutor Jorge Parola (FCT/UNL)

FACULDADE DE CIÊNCIAS E TECNOLOGIA
UNIVERSIDADE NOVA DE LISBOA

Setembro 2017

Gonçalo Alexandre dos Santos Marcelo

Licenciatura em Ciências da Engenharia Química
e Bioquímica

Synthetic Optimization Process of Mesoporous Nanoparticles for Protein Extraction in Biological Samples

Dissertação para obtenção do Grau de Mestre em Engenharia Química e Bioquímica

Orientador: Dr. Elisabete Oliveira (FCT/UNL)
Co-orientador: Dr. José Paulo Mota (FCT/UNL)

Composição do Júri:
Presidente de mesa
Prof. Doutor Mário Eusébio (FCT/UNL)
Orientador
Doutora Elisabete Oliveira (FCT/UNL)
Arguente
Prof. Doutor Jorge Parola (FCT/UNL)

FACULDADE DE CIÊNCIAS E TECNOLOGIA UNIVERSIDADE NOVA DE LISBOA

LAQV @ REQUIMTE

UCIBIO @ REQUIMTE

www.bioscopegroup.org
BIOSCOPE in the forefront of science

Setembro 2017

‘ It is about the fact that our lives are absurd. There is no God there is no Morality. Society invents rules to keep us from happiness, but every minute of every day we are free to decide who to be and how to live. ‘

Tom Spezialy

Acknowledgments

I would like to express my sincere gratitude to my supervisor Dr. Elisabete Oliveira for the continuous support on my MSc study and research, for her patience, motivation, enthusiasm, laugh and sincerity. Her guidance and insight were essential for the development and finishing of this work. My deepest thanks also go to Prof. José Mota, who co-supervised this work with always a cheering prospect and enthusiasm.

My sincere thanks also go to Prof. Carlos Lodeiro, Prof. José Luís Capelo and Dr. Hugo Santos for their constant advices and wise words. I thank my fellow lab mates from the Bioscope Group for the ever-present stimulating discussions, for their uncountable teachings and for all the fun we have had. I also thank the group for their investment and trust on my abilities and for their continuous care for my growth within the scientific world.

Last but not the least, I would like to thank my family and close friends for their constant support and counselling on the most tougher decisions and situations throughout this stage; especially to my parents Paula Rocha and João Marcelo, for being the wardens of my motivation, and my friends Ana Patricia, Inês Ferreira, Gonçalo Martins and Guilherme Nunes, for making every day easier, happier and for being the source of the most maddening and inspiring ideas.

Resumo

O trabalho aqui apresentado serve como “prova de conceito” a um sistema capaz de extrair proteínas de meios biológicos, com recurso a nanoparticulas de sílica funcionalizadas.

Apostando num desenvolvimento de raiz, foi tido como primeiro passo a síntese de nanoparticulas de sílica mesoporosas, seguido de uma caracterização física através de análises espectroscópicas de infravermelhos e de difração de raios X, bem como de isotérmicas de azoto a 77 K. Visou-se ainda a modelação do tamanho do poro e da interação partícula-partícula, através do uso respetivo de agentes expansores e de açúcares, de onde resultaram poros de 4 e 5 nm com S_{BET} de 343 e 534 cm^2/g e um rácio ótimo de açúcar : partícula de 1:1. Os poros foram funcionalizados com um derivado de rodamina B (RhNHS), com afinidade para com aminas primárias presentes em proteínas, e um máximo de encapsulação de 44 mg/g obtido. Consequentes testes de libertação em diferentes pH demonstraram que uma maior libertação é favorecida por meios ácidos.

Os testes de extração de proteínas foram levados a cabo em condições fisiológicas, para tempos de incubação de 30 minutos e 2 horas. A quantidade incubada (% L) e a capacidade de extração do sistema (mg/g) foram calculados após uma quantificação, por teste de Bradford, dos sobrenadantes. O aumento do rácio proteína : partícula em conjunto com o uso de RhNHS, levam a um aumento na quantidade de proteína adsorvida (464-519 mg/g), bem como na uma seletividade para proteínas ricas em grupos NH_2 (i.e. ovalbumina).

Por fim, o sistema foi ainda testado na extração e deteção a olho nu de iões metálicos tóxicos (Hg^{2+}, Cu^{2+} e Pb^{2+}) de meios aquosos contaminados. A incorporação de uma porfirina e/ou de RhNHS permitiram ao sistema devolver uma resposta colorimétrica aquando a deteção destes iões, com sensibilidade até concentrações de 5 ppm. A sua capacidade de extração foi ainda avaliada por ICP, bem como a sua reversibilidade e reutilização.

Palavras-Chave: nanoparticulas mesoporosas de sílica; RhNHS; tamanho de poro; proteínas; porfirina; iões metálicos; deteção e extração

Abstract

In this present work, it is proposed the development of a proof of concept for a solid-state device capable of extracting proteins from either artificial or biological media, based on functionalised silica mesoporous nanoparticles.

Following a “from scratch’ approach, cubic-phased SBA-16 silica nanoparticles were firstly synthesised. Their characterisation was achieved by infrared and X-ray diffraction spectroscopic techniques, along with N_2 physio sorption isotherms, at 77 K. Pore modulation and dispersion behaviour were controlled using expanding agents and sugar coatings, respectively. Studied pore widths were of 4 and 5 nm, with S_{BET} of 343 and 534 cm^2/g, and an optimal sugar : protein ratio for minimal agglomeration was of 1:1 (wt.). Pore functionalisation was attained through the adsorption of a NHS-based rhodamine B derivative (RhNHS), with affinity towards amine groups in proteins. A pore width-independent loading maximum of 44 mg/g was achieved and release tests were performed for different pH values, with acidic conditions favouring a stronger release.

Protein extraction assays were run on PBS 7.4 to mimic physiological conditions, with incubation times of 30 minutes and 2 hours. Loading yields (% L) and capacities (mg/g) were obtained after supernatants quantification by Bradford assay. An increase on the protein : particles ratio (i.e 1:1), as well as the use of RhNHS, had a general positive effect on the total amount of loaded protein (464-519 mg/g) and a selectivity towards NH_2 residue-rich proteins (i.e ovalbumin) was also observed.

Lastly, an environmental extension of the work aimed for a colorimetric detection and the extraction of toxic metal ions (Hg^{2+}, Cu^{2+} and Pb^{2+}), from aqueous and biological media (urine), with porphyrin and RhNHS doped silica nanoparticles successfully working, at naked-eye, down to 5 ppm concentrations. Extracted quantities were quantified by an induced coupled plasma technique. Reversibility and reusability were also tested for both systems.

Keywords: SBA-16 mesopores silica nanoparticles; RhNHS; pore size; protein; porphyrin; toxic metal ions; detection and extraction

Scientific Communications

G. Marcelo, E. Oliveira, H. M. Santos, José Paulo Mota, J.L. Capelo and C. Lodeiro
"Synthetic optimization process of mesoporous nanoparticles for protein extraction in biological samples"
XXV Encontro Nacional da Sociedade Portuguesa de Química; Lisboa, Portugal – 12-15th July 2017
Type of Contribution: Poster Communication - http://xxvenspq.eventos.chemistry.pt/

Gonçalo Marcelo, Elisabete Oliveira, Sónia Pires, M. Graça P. M. S. Neves, José Paulo Mota, José Luís Capelo, Carlos Lodeiro
"Mesoporous Silica Nanoparticles functionalized with Porphyrins as a reusable solid-state system for metal detection via emission and colorimetric effects "
Jena Symposium on Remediation 2017; Friedrich-Schiller University of Jena, Germany – 5th October 2017
Type of Contribution: Poster Communication

G. Marcelo, E. Oliveira, H. M. Santos, José Paulo Mota, J.L. Capelo and C. Lodeiro
"Development of reusable solid-state chemosensors based on fluorophores for Hg2+ detection in aquatic media"
2nd International Caparica Conference on Pollutant Toxic Ions and Molecules (PTIM); Costa da Caparica, Portugal – 6-9th November 2017
Type of Contribution: Poster and Shot-gun Communication - http://www.ptim2017.com
Awards: **Excellent Shotgun Communication Award**

G. Marcelo, E. Oliveira, H. M. Santos, José Paulo Mota, J.L. Capelo and C. Lodeiro
"Synthetic optimization of mesoporous silica-based nanosystems for protein extraction in biological samples"
2nd International Caparica Christmas Congress on Translational Chemistry (IC3TC); Costa da Caparica, Portugal – 4-7th December 2017
Type of Communication: Poster and Shot-gun Communication - http://www.ic3tc2017.com/

Scientific Paper

Gonçalo Marcelo, Elisabete Oliveira, M. Graça P. M. S. Neves, Sónia Pires, José Paulo Mota, Carlos Lodeiro, José Luís Capelo
"Mesoporous SBA-16 nanoparticles with dual Porphyrin and Rhodamine cargos as new colorimetric probes for toxic metal ions detection / extraction"
Submitted to the Journal of Hazardous Materials.

Index

Figures Index

Tables Index

Abbreviations List

CTAB	Cetyltrimethylammonium bromide
EO	Ethylene oxide
EDTA	Ethylenediaminetetraacetic acid
EtOH	Ethanol
FTIR	Fourier Transform Infrared Spectroscopy
ICP	Induced Coupled Plasma
LCT	Liquid Crystal Templating
L5	Porphyrin chromophore
L5@SBA	Porphyrin chromophore doped SBA silica nanoparticles
MeOH	Methanol
MCM	Mobil Composition of Matter
NHS	N-hydroxysuccinimide
PO	Propylene oxide
RhB	Rhodamine B
RhNHS	NHS-modified rhodamine-based chromophore
RhNHS@SBA	NHS-modified rhodamine-based chromophore doped SBA silica nanoparticles
RhISO	Rhodamine B isothiocyanate chromophoro
RhISO@SBA	Rhodamine B isothiocyanate doped SBA silica nanoparticles
S_{BET}	Specific BET surface area
SBA	Santa Barbara Amorphous
SEM	Scanning Electron Microscopy
TBOS	Tetrabutylorthosilicate
TEOS	Tetraethylorthosilicate
TEM	Transmission Electron Microscopy
TMOS	Tetrametylorthosilicate

1

Introduction

1.1 Motivation

Since early 1970's the discovery and development of easy-to-control and tuneable inorganic material framework [1-4] has gained its place among most of the top industries and study areas around the world. Namely, the synthesis of silica particles has been one of the most thoroughly sought technique for the creation of many catalytic supports, [2, 5] drug delivery systems, [6] bioimaging probes [7, 8] or sorption devices, just to name a few examples. As it is currently proven and seen, even after 40 years this family of materials finds itself among the most requested building blocks for novel and innovative ideas [9, 10]; thus, vindicating its usage and improvement.

1.1.1 Mesoporous Silica Nanoparticles

Silica materials are known for being nontoxic, thermally / hydrothermally resistant inert materials [3] formed of repetitive tetrahedral SiO_4 units. The assemble these 'monomeric' units leads to the formation of either crystalline or amorphous structures that can grow from tens of nanometres up to hundreds of millimetres, in diameter [4]. Whilst crystalline structures present a well-defined repetitive arrangement, and thus low available surface-area, amorphous ones are made up of a complex matrix of porous (acting as sponges) that give them large surface-areas of 100 to 1000 m^2g^{-1} [3].

From an structural point a view, the above mentioned ceramic oxide 'monomer' (SiO_4) promotes the formation of siloxane groups (*R*-**Si-O-Si**-*R*) that are responsible for the growth of silica materials, and of silanol surface groups (*R*-**Si-OH**) that control their interaction with the surrounding media, as well as its reactivity (Figure 1.1) [11].

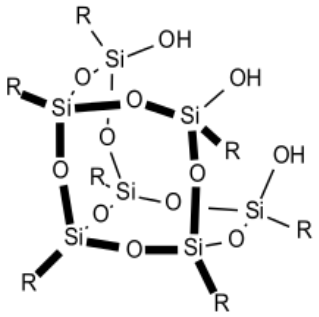

Figure 1.1 | Spatial arrangement of siloxane (Si-O-Si) and silanol (Si-OH) groups within silica materials matrixes.

The conditions of growth of these materials along with the right choice of reagents, has allowed for the development of easy and reproducible methodologies [12-14] to tune this arrangement, and consequently its mean pore-size; ranging from microporous (d < 20 Å) [2, 4], to mesoporous (20 Å < d < 500 Å) [3, 15, 16] and up to macroporous (d > 200 nm) [17]. It is then of utter importance to, depending on the material's application (e.g. biological molecules internalisation), find the best approach to synthesize the right structure.

In 1992, researchers from *Mobil Oil Research and Development* [2, 18] found a way to synthesize what is now one of the most commonly used mesoporous silica structures, the MCM-41. This one belongs to the M41S family of mesoporous silica materials which have large surface-areas and highly ordered mesoporous molecular sieves [19, 20]. A welcoming addition, at the time, to classical zeolites and still one of the most pertinent materials in industry. M41S family members have had their denomination after their pore spatial arrangement and are briefly described below (Figure 1.2).

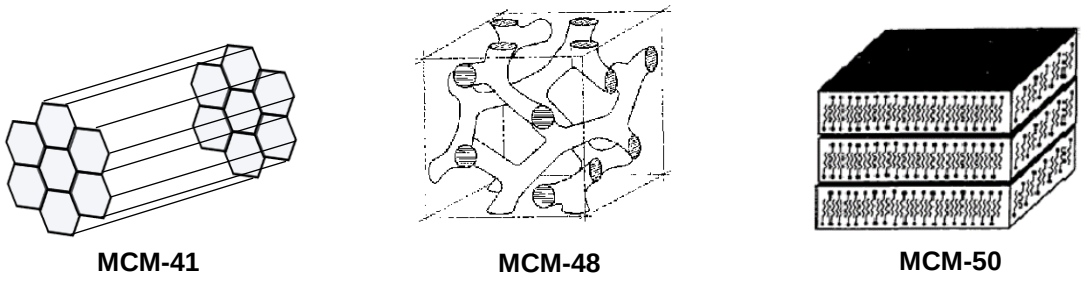

MCM-41	**MCM-48**	**MCM-50**
Unidimensional hexagonal pore display	Three-dimensional cubic pore display	Parenthetic display of layers of silica and surfactant

Figure 1.2 | M41S family of mesoporous silica structures, with its members named after their conformation. Adapted from [21].

The development of these porous structures within silica nanoparticles (10 nm up to 1000 nm, in diameter) is based on a micellar approach and uses as structuring agents cationic or anionic surfactants (e.g. CTA+), in basic media [4, 18-20, 22]. Besides, surfactants hydrophobic chains size is also an important factor to take in consideration, for it preordains the display of our porous structures (MCM-41, MCM-48 & MCM-50); with long chains favouring layered silica structures [22].

Several models are thought to describe the assembly mechanisms of mesoporous silica nanoparticles, namely the co-condensation (or self-assembly) of opposite charged species of silica precursors and surfactants ($S^+ I^-$ or $S^- I^+$), and the counter-ions mediated mechanism, which depends on ions of opposite charge of that of the head of the surfactant ($S^+ X^- I^+$) [3, 4, 22] Nonetheless, all of them are based on the principle that surfactants are responsible for the formation of this final porous structure.

Being made of both an hydrophilic end (head) and an hydrophobic tail, when in aqueous solution, surfactants tend to aggregate and form micellar structures, whose form is mediated not only by its concentration but also by extrinsic factors as temperature, pH, presence of electrolytes and solvents [2, 4, 5, 12, 19, 20, 23].

It is over such structures that silica precursors will grow and form the rigid silica skeleton of nanoparticles. Thus, it has been proposed by *Mobil* researchers, that the growing mechanism follows what is called a *Liquid Crystal Templating* (LCT) [2], where an initial liquid crystal phase composed of semi-ordered structures of surfactant is fixed (and ordered) by the addition of silica precursors species. In detail, when in optimal conditions of pH and temperature, and in the presence of highly concentrated surfactant solutions, this liquid crystal phase self assembles and serves as base for silica aggregation, growth and pore walls formation; however, when in low concentrations of surfactant, silica precursors (Tetraethylorthosilicate – TEOS – or tetramethylorthosilicate – TMOS) also act as directing and structuring agents helping the formation of micelles. To both approaches we call, self-assembly and cooperative pathways, accordingly (Figure 1.3) [24].

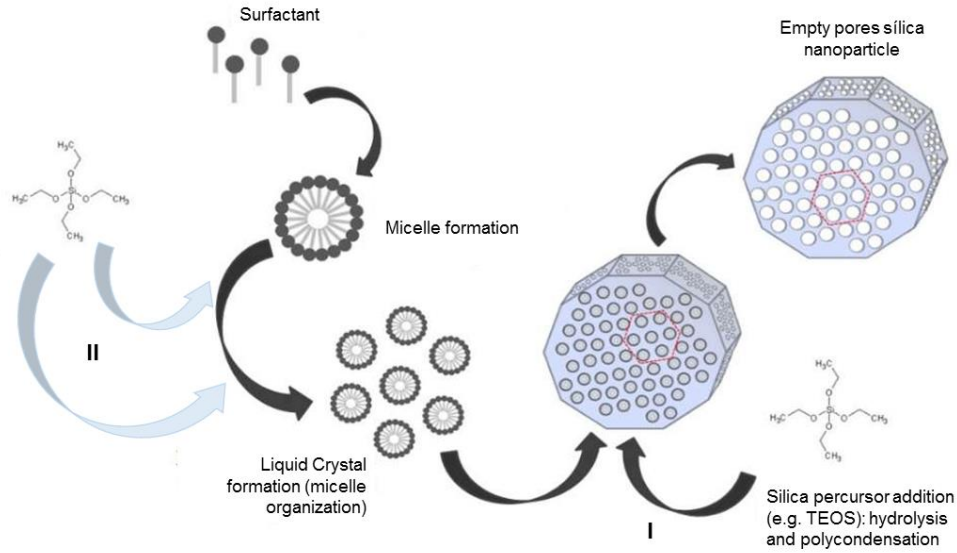

Figure 1.3 | Synthetic procedure for silica nanoparticles, following the LCT mechanism: I - self-assembly and II - cooperative paths. Adapted from [25].

In a last step, the as-synthesised nanoparticles are then submitted to template (surfactant) removal techniques, be them calcination at temperatures near 500 ºC or chemical removal with solvents, to obtain empty pores. Even though calcination is known for being one the most used methodology to completely remove templating molecules, it is also taken to be a very sensible heating technique where a strict control over a rising temperature is needed in order to avoid overheating and consequent higher cross-linking degrees between mesoporous materials, as well as lower surface areas, pore volumes and surface available hydroxyl groups. Conversely, solvent-based extraction is a mild and effective surfactant removal technique that is able to not only promote a full recovery of these, but also assure the attainment of homogeneous pore structures along the materials [26]. Fortunately, since its discovery many others mechanisms have been developed and optimised, namely acidic and microwave assisted routes [27, 28].

Summarizing, due to their unique organization, large surface-areas (of approx. 1000 m^2g^{-1}), and high porous volumes, this group of materials, MCM-41 included, has found a large spectrum of applications through various research and industrial fields. However, production of pores of 1 – 10 nm width [3, 4,

18], as is the case of MCM-41 structures, find no real application in biological / biochemical fields for most molecules of interest (proteins, antibodies, drugs) are themselves some nanometres long.

Therefore, along with exhaustive studies developed over this kind of materials at the time, a new family of mesoporous silica nanoparticles was discovered – *Santa Barbara Amorphous* (SBA) type material. In 1998, large surface-area (600-1000 m^2g^{-1}) hexagonal *Micelle-Templated Silicas (MTS)* were reported by *Zhao et al.*, with pore sizes between 5 - 30 nm [3, 4]. This new kind of silica nanoparticles, named after the institute where they were synthesised (SBA-15), not only showed larger pores, and higher thermal and hydrothermal stability, due to their thick pore walls (with 3.5 – 6.4 nm), but also made use of a non-ionic amphiphilic surfactant – Pluronic P123 ($EO_{20}PO_{70}EO_{20}$). Besides, pore size and wall thickness can both be tuned by varying reaction temperature and time (from 35 ºC to 140 ºC and 11 to 72 h, for SBA-15 case) [3, 4, 16]. This surfactant, a triblock copolymer with a central Ethylene Oxide (EO) hydrophobic block and two Propylene Oxide (PO) hydrophilic ends [29, 30], is to react with silica precursors through the assistance of a counter-ion pair species – usually denominated as co-surfactant. In detail, it has been proposed that the surfactant S^0 (non-ionic) and the positively charged silica precursor I^+ interact in acidic medium through an ionic pair $S^0\,H^+\,X^-\,I^+$, forming relatively week hydrogen bonds [16]. This leads to the formation of the most various forms of nanoparticles, which might be and not be a good asset.

It has been confirmed that the addition of a salt to the reaction mixture (e.g. cetyltrimethylammonium bromide – CTAB – or NH_4F) is a crucial step when chasing sharper shapes and well-defined nanoparticles sizes [16, 31] . Whether in its absence, only undefined shapes and a wide range of sizes are obtained. This corroborates previous statements, that particles morphology is reigned mostly by the $S^0\,X^-\,I^+$ interaction [32].

Similar to M41S materials, the size and shape of the chosen surfactant is one of the most important factors when designing SBA mesoporous silicas. It has been observed that the EO:PO ratio plays a decisive role, resulting in hexagonal or lamellar dispositions at low ratios (for concentrations of 0.5-1 % (w/w) and 2-5 % (w/w), accordingly) and in cubic conformations at higher ratios (Figure 1.4) [3].

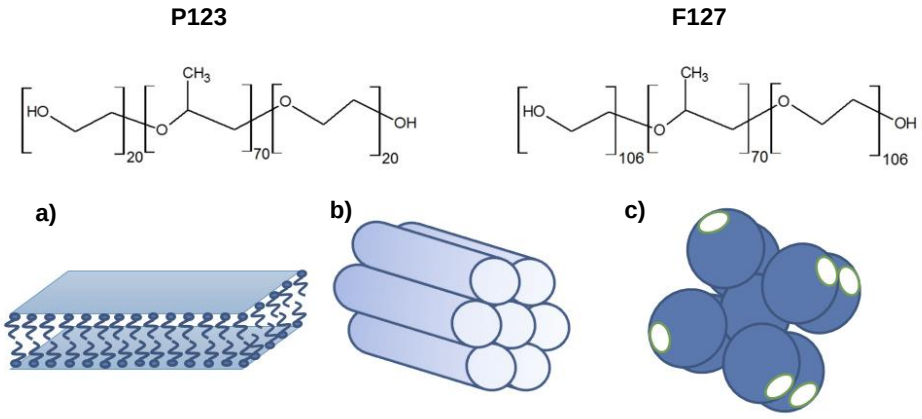

Figure 1.4 | Structures of pluronic P123 (EO20PO70EO20) and F127 (EO106PO70EO106) directing agents and some of the resulting mesoporous structures: a) laminar, b) hexagonal and c) cubic arrangements, depending on EO:PO ratios and pluronic concentrations. Adapted from [31].

A most immediate example of this influence is the synthesis of SBA-16 silica mesostructures that, using a more hydrophilic pluronic - F127 - as structuring agent, promotes the formation of body-centered nanocages with cubic arrangement [33] . While SBA-15 particles display well-ordered parallel hexagonal arrangements of pores that allies micro and mesoporosity with thick walls (Figure 1.5), SBA-16 creates a complex matrix of mesoporous channels (with each hollow sphere connected to eight other hollow spheres) that favours the internalisation of biomolecules [26, 31, 34].

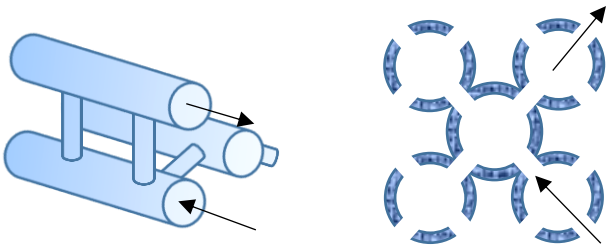

Figure 1.5 | Close view of SBA mesoporous silicas of SBA-15 (left), with microporous connecting its macroporous channels, and SBA-16 (right) side view of its intricate matrix of macroporous channels. Adapted from [31].

It is important to recall that this family of materials is also dependent of external conditions such as temperature and pH, which are theorised to interfere directly with the protonation and hydrophilicity of EO blocks [3], as well as silica isoelectric point and condensation rate [35] . With amorphous materials favoured by neutral pHs (~ 7) and crystal ones by strong acidic media (pH ~ 2).

Another improvement that has been reported, is the reusability of pluronic surfactants once template removal is achieved. Washing the as-synthesised nanoparticles with ethanol at 78 ºC allows the organic copolymer to completely dissolve in the solvent and be reused in future synthesis [3] .

Table 1.1 | Main properties of most used silica mesoporous nanoparticles [3, 4, 14, 19, 26, 36, 37].

	MCM-41	**SBA-15**	**SBA-16**
Surfactant type	Cationic / Anionic	Pluronic P123 (ion assisted)	Pluronic F127 (ion assisted)
Medium	Basic	Acidic	Acidic
Pore-size	2-10 nm	5-30 nm	5-30 nm
Pore wall thickness	~ 1 nm	3.5 – 6.4 nm	3.5 – 6.4 nm
Stability	Thermal	Thermal & Hydrothermal	Thermal & Hydrothermal
Mesophase structures	2D hexagonal (*p6mm*)	2D hexagonal (*p6mm*)	3D cubic (*Im3n*)
Main application	Zeolites, Catalysts, Delivery systems	Zeolites, Catalysts, Delivery systems	Zeolites, Catalysts, Delivery & Extraction systems

In conclusion, although M41S mesoporous synthesis methodologies are easily reproducible and less time-consuming than those of SBA mesoporous material, these last are able to overcome some of the problems that come with the synthesis of MCM-41; namely, small mean-pore diameters (up to 10 nm), thin pore walls (translating into less thermal or no hydrothermal stability) and low capability of internalisation of biomolecules (Table 1.1).

Therefore, allying large surface-areas, three-dimensional ordered mesoporous structures, thicker framework walls, high thermal and hydrothermal stability, super-large cages, complementary textural porosity with a more favourable mass transfer than that of unidirectional pore systems (due to their three-dimensional channel connectivity) [26] makes SBA-16 structures one of the best candidates for proteins, or other biochemical active species, loading and extraction from biological media.

1.1.2 SBA-16 and Applications

SBA-16 silica nanostructures are considered one of the most interesting mesostructures due to their unique 3D cubic arrangement of mesoporous (*Im3m* spacing) and the presence of large spherical cages that promote an optimal environment for catalytic reactions (acting as nano-reactors), molecules adsorption and metals/dyes extraction [31, 38-41], to name a few applications.

However, a limited number of SBA-16 synthesis methods have been so far reported, mostly due the narrow range of conditions that these cage-like structures can be obtained [3, 31, 33, 38, 42].

In 1988, along with SBA-15 discovery, it was reported that the existence of long hydrophilic EO chains within the triblock copolymer was crucial for the formation and development of cubic-phased SBA materials (Figure 1.6) [3].

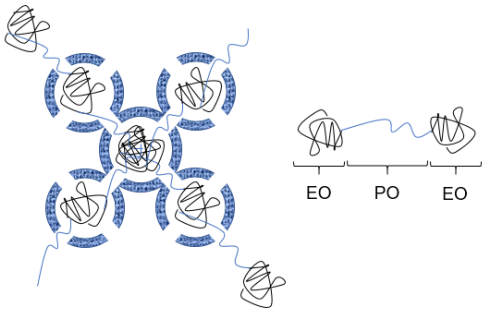

Figure 1.6 | Pluronic EO_xPOyEO_x arrangement inside cubic-structured silica material, where x > y.

However, improvements on its synthesis only appeared later in 2002, when single crystal particles (with a mean size ~1 μm) were synthesised, under static conditions, using triblock copolymer F108 ($EO_{133}PO_{49}EO_{133}$) as structuring agent, assisted by K_2SO_4 and HCl [42]. Concluding that crystal structures are favoured by highly charged counter-ions, whilst heterogeneous morphologies were attained for single charged ions (e.g. Cl^-). It has also been reported by Kleitz *et al.* the synthesis of SBA-16 using F127 copolymer in a mixture of butanol-water, at low HCl concentrations [43]; where a relationship between silica precursor, co-solvent and cubic *Im3m* predominant phase is demonstrated. Additionally, the presence of acidic species promotes the already mentioned $S^0 X^- I^+$ interactions, enhancing tunability of shape and pore as well as ensuring some reproducibility to the process [26].

Hence, it was proposed that both morphology and particle size are strongly affected by the regularity of the poly-condensation degree of silica species over surfactant micelles, which in turn is mainly determined by media temperature and pH [32, 36, 44]. A solution that helps regulate shape and easily control morphology was attained when synthesising SBA-16 with the help of ionic co-surfactant CTAB [16, 32, 36].

Unfortunately, a significant issue that arises from the synthesis and strongly hinders SBA-16 large scale applications is its time-consuming reaction (approx. 72h). The use of SDS or CTA+ co-surfactants is thought to shorten micellation time of pluronic species, acting as micellation promoters [33], and has already been demonstrated that it can produce SBA-16 nanoparticles within one hour of reaction [45].

Henceforth, although cubic-phase materials were already a current occurrence in mesoporous structures (MCM-48), the discovery of SBA-16 has brought a new solution to previous hitches of relatively week stability, small pore sizes and low mass transfer capacity. Still a scarcely studied mesoporous structured it has showed so far a very prominent material with a broadening spectrum of applications; from a 'ship-in-a-bottle' nanoparticle synthesis catalyst [40], FCC Diesel hydrogenation catalyst [46], O_2 producing (H_2O oxidation) cells [34], poorly-soluble drug carriers [39, 47], removal devices of neutral, cationic and anionic dyes [38], to biomolecules adsorption & enzymatic reactions supports [16, 48].

1.1.3 Mesoporous nanoparticles for protein extraction

Parallel to advances on mesoporous silicas synthesis, a significant interest in the development of protein encapsulation nano-devices has helped understand the importance of surface control and pore modulation on biomolecules adsorption and desorption mechanisms.

Interactions between proteins and mesoporous silicas are thus of utter interest due to the extensive range of applications that arise from their adsorption / binding, including drug delivery, biochemical synthesis, biosensoring, and bioseparation.

In regards to the binding (chemical interactions) of proteins to ceramic nanomaterials, several resulting conformations have been reported [6, 7, 48-52], ranging from functionalised particle's surfaces (improving or modulating surface biological interactions, as well as extending these systems' life span within living organisms), to inner pore walls (acting as specific binding sites, catalysts or imaging probes) and to pore gateways (working as entry molecules, sensing devices or controlled drug delivery systems). Conversely, physical interactions have been usually applied on the development of isolation, preconcentration or purification through-adsorption (surface or pore adsorption) devices for later internalisation on size-selective or affinity chromatography, important techniques in the pharmaceutical industry.

However, a key challenge in designing mesoporous silica vehicles for tailor-made protein interaction is the differentiation of protein interactions at the surface of the particle from those within pores [16, 31, 53, 54]. It has been reported, so far, that this distinction is strongly influenced by a series of factors extending to silica particles' size [55, 56], pore size [54, 57-59], surface net charge (zeta potential) [60,

61], specific surface area [62], protein size and spatial conformation [57, 63, 64], pH [31], terminal functional groups, solubility [61] and protein-protein interactions [16].

From the few publications concerning the designing of tailor-made silica nanoparticles for the effective scavenging of a set of biomolecules from biological media, small pore size (<3 nm) has been highlighted as one of the main variables responsible for the drop of internalised protein amounts and the formation of a surface corona [53, 58]. On this outer structure proteins are prevented from using the protective environment and the large internal surface area provided by pores. Aware of this situation, the production of large pore materials (>5 nm) was proposed by several authors [16, 31, 48, 53, 54] as a way to overcome inaccessibility issues, with Katyiar *et al* [16] being able to generate silica particles with pores up to 12 nm and achieve loaded quantities (using lysozyme as model protein) above those reported for smaller diameters. Interestingly, Schlipf *et al* [54] have also demonstrated that although large pores promote indeed a more effective extraction of proteins, a threshold pore size exists for each species with dimensions around that of the biomolecule cross section.

However, the development of such large pore structures has often been associated with micrometric particles, 1-15 um, from which additional dispersion and adsorption issues arise. It has been reported that heterogeneous interactions between particles (intrinsically related to surface zeta potential and a consequence of wide size distributions) promote assorted surface-protein interactions and induce some conformational changes on adsorbate molecules, with significant vicissitudes for particle diameters above 200 nm [65]. Lundqvist *et al* [66] have also reported a relationship between conformational changes on adsorbate molecules and spherical-like particles size, with larger particles inducing up to six-fold changes on the secondary structure of adsorbed molecules and increasing surface adsorption.

Thus, as emphasised by Tu *et al* [53], a compromise between large pores and smaller (< 1 μm) particles is desired to obtain a high density of entrances and ensure preferential encapsulation of proteins within the mesoporous structure.

Nevertheless, the research for other methods to trace and modulate particle-protein interactions has fallen over the employment of intermediate molecules able to link with those of interest and rapidly give visual insight. The tagging of proteins with chromophores, or fluorophores, whose terminal functional groups showed considering affinity towards peptide side or terminal groups, brought the possibility to easily image and understand the diffusion of proteins within and around particle pores and surface, respectively.

Chromophores and fluorophores belong to a family of organic molecules that, due to the existence of π delocalised bonds along their structure, can interact with near-UV or visible radiation to make their valence electrons easily jump between excited and ground states, resulting in the emission of light (normally coloured) in the same range. Although some of them might lack the possession of linkage elements towards any type of biomolecules, simple organic manipulations on their terminal groups can produce substances with tailored affinities, that can later be internalised in nanometric vehicles designed for protein imprisonment [49-51, 54].

The tracing of any peptic activity on the vicinities of nanoparticles is then highlighted by changes in the behaviour or luminescence of the already loaded chromophores. These changes include either inward and outward flows, with direct consequences on internal or external concentrations and luminescence intensity, or shifts in the maximum absorption wavelength, result of possible bindings between target proteins and chromophores.

The development of these methodologies along with considerations of previews studies is a determining mediator towards the improvement of many conventional purification, or identification methodologies and also the designing of new techniques and devices able to selectively interact with target biomolecules.

1.1.4 Mesoporous nanoparticles for metal detection

One of the primary issues that comes with the increasing human activity and ever rising handling of natural resources is the uncontrollable release of unknown quantities of toxic substances to either natural environments [67] or straight to human habitats [68]. The problem aggravates when these human habitats belong in undeveloped countries where sanitation and health care are still precarious services [69-71].

Metallic ionic species present one of the most endangering sources of toxicity and poisoning, due to their relatively easiness to infiltrate and accumulate in other media, especially aqueous ones [67, 68], on which once ingested by small animals, can enter the rest of the food chain. Some examples of such ionic species are Hg^{2+}or Pb^{2+} ions that, in regards to their oxidation state, easily react with other molecules, including biological molecules specialised to capture in-body metallic atoms [72, 73]. Just to name another example, during fossil fuel or waste burning [73, 74] inorganic Hg usually tends to react with organic molecules and form methylmercury 2+ (CH_3Hg^{2+}), which by instance is a bio accumulative environmental toxicant [73]. Even though it can be found in many natural environments [67], including living beings, excesses of this substance usually lead to the formation of strong binding CH_3Hg-protein, or CH_3Hg-amino acid, complexes that mimic other biomolecules activities and end up inducing malfunctions [75]. Additionally, it has also been linked to increased risk of certain diseases [76, 77] and autoimmune effects in sensitive individuals [78]. These are just some of the reasons to why toxicological studies are of utter importance and of why has there been such a huge development of new tailor-made materials for toxicants fast detection and extraction, especially of Hg^{2+} species.

Seeking a way to overcome expensive conventional techniques [73], the introduction of nanotechnology has brought, trough out the last two decades, the ability to hastily and selectively sensor toxic ionic substances in not-so expensive ways, by making use of fluorescent / colorimetric probing devices [79-86].

The use of chromophores has been one of the main key-points when selectively coordinating and detecting metallic ions. This family of organic or bioinorganic molecules, suffer visual significant changes when its structure is somehow changed during complexing of ionic species. The magnitude of those optical changes can vary on a long range of concentrations, going from a usual 1 M to 10^{-3} M

scale to ppm's [80, 81], or even ppb's [79, 82, 83, 86] (within the limits established for drinkable water by the US Environmental Protection Agency, EPA [73, 87, 88]).

However, the handling of these substances is usually associated with dissolutions in aqueous media (or biological complex media) which difficult any possibility of extraction and cleaning of contaminated areas. This is where nanotechnology acts, by producing solid-state vehicles where the above-mentioned molecules can be immobilised while still interacting with metallic species in solution. Some examples of such vehicles are tailor-made gold nanoparticles, silver / gold-doped paper-based devices or mesoporous silica nanoparticles whose surfaces, channels or pores have been functionalised [80, 82, 83, 89-91].

The difference in sizes (between solute molecules and nanoparticles) allows for an easier separation with the simple use of conventional, cheap and easy separation techniques (e.g. centrifugation). Most recent developments have, nonetheless, produced devices that are sensible to magnetic fields and can be easy isolated from any supernatant, when under its influence [91].

Thus, it is most obvious the importance that these materials have gained within legal organisations' efforts towards a safer and healthier environment. Prospects of large scale productions are strongly related to economic viability, and the ever-growing interest in the development of cheaper and faster and more efficient devices is the strongest driver for the construction of new approaches; as it is proposed in this work.

1.2 Synthetic pathways

The synthesis of silica based mesoporous materials is known to follow different possible routes, from sol-gel techniques [3, 4, 14, 26] to hydrothermal or microwave assisted ones [27, 28].

1.2.1 Sol-Gel Method

By far the most commonly used synthetic route, and the one used in this work, sol-gel is a homogeneous processing that promotes the full transformation of a solution into an hydrated solid precursor, through mechanisms close to that of condensing polymerisation. An initial 'monomeric' solution leads to the formation of a sol (a dispersion of colloidal polymeric-like particles of 1 - 100 nm) with a later establishment of a gel, after sol's cross-linkage. For silica-based materials these 'monomeric' units, or precursors, are usually alkoxysilane species like tetramethyl-, tetraethyl-, tetrabutylorthosilicates (TMOS, TEOS and TBOS, accordingly).

The sol-gel constitutes nowadays a unique pathway to the synthesis of mesoporous silica without the deployment of extreme temperatures. Additionally, such technique is known for allowing the user to manipulate, to a certain extent, some structural parameters [26, 92].

Succinctly, this technique is well known for allowing: 1) the synthesis of highly pure products; 2) tune morphological aspects of the final product, such as pore-size, pore volume and particle size; 3) obtain through a 'one-pot-route' tailor made materials, at low temperatures and specific shapes; and 4) control

the material's molecular composition. Moreover, the sol-gel technique is usually divided into four main steps [92-103]:

1) Hydrolysis and polycondensation of alkoxide precursors;

2) Aging;

3) Drying;

4) Thermal treatment.

However, once working at the nanoscale, it is important to point out that for the formation of silica mesoporous nanoparticles the process is to be stopped before sol cross-linkage, promoting sol's precipitation and resulting in uniform particles (Figure 1.7) [96].

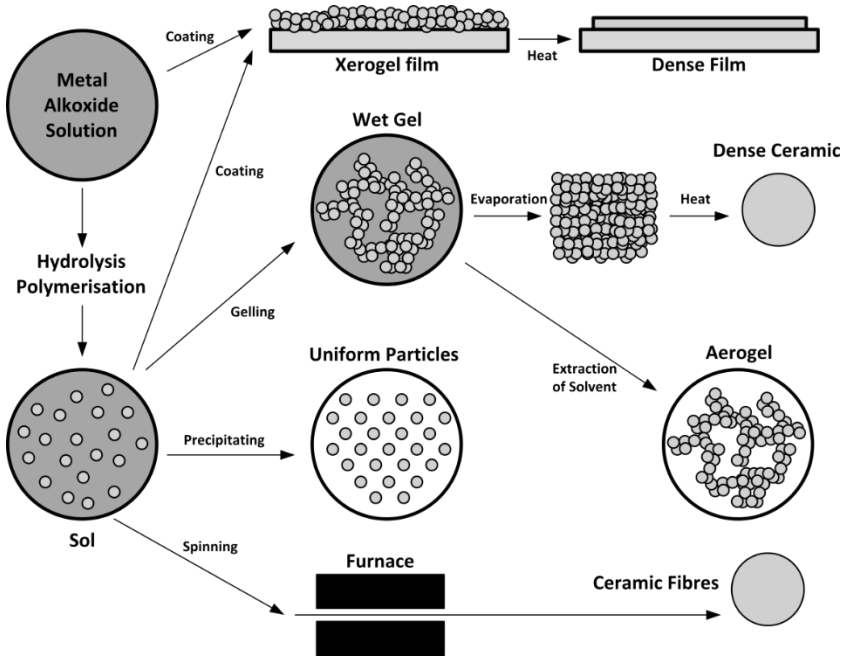

Figure 1.7 | Schematic summary of sol-gel process and its many final products. Uniform particles formation along a precipitation pathway is evident. Adapted from [93-106].

Nonetheless, detailed information on each of the technique's steps follows below:

1) Hydrolysis and polycondensation of alkoxide precursors

The above-mentioned precursors, or 'monomers', that will later form a sol can be from either molecular or non-molecular sources. Whether the first (dissolved metal alkoxides) produce homogeneous products, the later (usually already polymerised colloidal materials) lead to the formation of non-homogeneous solutions. Thus, explaining the common usage of the first [26].

Much like polymeric reactions the formation of a sol is based on a system of reactions where initiation is followed by polymerisation and subsequent growth. The initiation step is usually catalysed by either an acid or a base, that promotes the hydrolysis of silica precursors when in contact with water, giving

form to silanol groups. Groups those, that will polymerize (by condensation) and grow into larger structures [92-106].

Briefly,

Initiation reaction (Hydrolysis)	≡Si−OR + H2O → ≡Si−OH + ROH
Silanol-Ester Condensation	≡Si−OH + ≡Si−OR → ≡Si−O−Si≡ + ROH
Silanol-Silanol Condensation	≡Si−OH + ≡Si−OH → ≡Si−O−Si≡ + H2O

Where, R stands for a hydrogen atom or an alkyl group.

It is then obvious this step's dependence on medium's pH. Variances on the acidic profile of its surroundings change polymerisation kinetics and, consequently, the final product features (Figure 1.8).

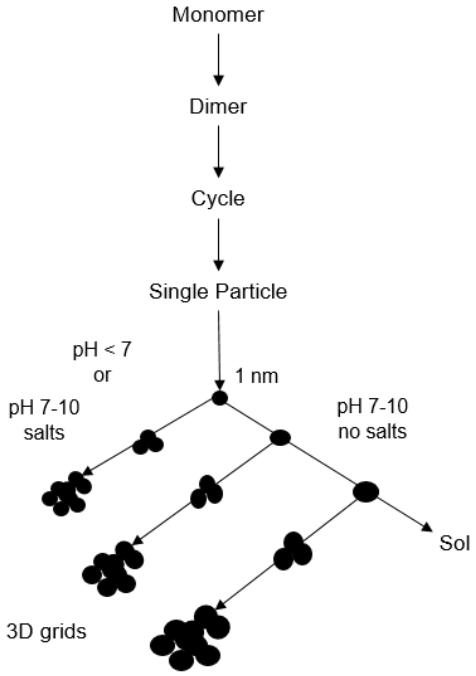

Figure 1.8 | Polymerisation pathways and its final products, from 3D reticulated grids to sols. Adapted from [107].

2) Aging

Once the gel is established, the presence of an evaporating reaction solvent inside pore-like structures leads to several modifications that are susceptible to external variables. Again, these may be temperature, solvent's pH and aging time [98].

Several phenomena are theorised to occur during aging, namely polycondensation, syneresis, coarsening, and phase transformation. Whilst with polycondensation the gel network keeps growing as long as neighbouring silanols are close enough to react (increasing connectivity of the network and its fractal dimension), syneresis translates into a natural shrinkage of the gel and expulsion of solvent from its pores. Additionally, coarsening is a consequence of dissolution and reprecipitation processes, that result in the irreversible decrease of surface area [92].

3) Drying

Generally seen as a simple elimination - by evaporation - of the solvent locked inside silica pores, the drying process might be one of the most important steps of sol-gel method. This technique usually starts by a previous separation of the solid from its aqueous media, either by filtration or centrifugation, accompanied by several washes to remove possible impurities and solvent vestiges.

An already uneventful procedure in crystal drying, this step becomes crucial when dealing with mesoporous materials where an equilibrium between gel shrinkage and solvent evaporation must be met to ensure the material's initial properties and morphology. For this, vapor-liquid interface formation is to be avoided, as much as possible, in order to reduce capillary pressure and lessen the establishment of ruptures and deformations within porous structure [92, 100, 108].

4) Thermal Treatment

This last step of the sol-gel method is usually related with calcination techniques and allows for the fixation of certain intrinsic variables of the material, such as porous volume, pore-size distribution and specific area. Under inert or ambient atmosphere, with the use of high temperatures, the material undergoes several transformations that lead to surfactant and precursors disintegration, thus helping define material's porosity and mechanical resistance. Additionally, changes in the material's crystalline framework might occur, resulting in either amorphous structures or stable crystalline matrixes [92, 101, 108].

In this work, solvent-based template removal techniques were used in detriment of calcination techniques, although a mix of both has been reported as an ideal methodology [109]. Solvent-based template removal procedures usually use alcoholic acidic media (e.g. EtOH/HCl blends) to help dissolve and wash away remnants of any surfactants or swelling agents [3, 4, 14, 109].

1.2.2 Hydrothermal Method

Although not used in this work, this method has gained its importance in nanomaterials synthesis and is now seen as one of the best to ensure reproducibility and homogeneity of its final products. Result of technological developments, this technique found its origins in the 21st century and uses supercritical fluids (usually water) to help with the processing of highly homogeneous and monodispersed materials/nanoparticles.

Briefly, the hydrothermal process is defined by a mix of reactions, under high pressure and temperature conditions, that promote a controllable dissolution and recrystallisation of relatively insoluble materials. This brings important advantages over other synthetic pathways, for it allows the easy monitorisation of the final physio-chemical properties of nanomaterials, through the highly controlled diffusivity in solvents and easy establishment of sharp temperature gradients [110].

The use of supercritical technology, due to its high pressures and temperatures, makes it impossible to follow regular research procedures and requires the usage of very resistant vessels, such as

autoclaves. Therefore, autoclaves must be: i) Inertness to acids, bases and oxidizing agents; ii) easy to assemble and disassemble; iii) long enough to obtain sharp temperature gradients; iv) leak-proof with limitless aptitudes to the required temperature and pressure range; and v) rugged enough to bear high pressure and temperature tests, for long periods [110].

1.3 Characterisation Techniques

The determination and quantification of a certain material's set of properties is only possible through the application of a wide and specific range of practical and analytical techniques. With the right system, textural and spectroscopic profiles can be traced and intrinsic variables/properties determined. The same applies for behavioural and time dependent events, that can be outlined and studied. For the case herein proposed, structural variables – such as specific area, porous volume, pore size distribution, particle size, atomic/molecular composition, crystalline lattice, zeta potential – and spectroscopic parameters – as absorbance and emission – are some of the essential characteristics to be analysed or determined to better understand our system.

1.3.1 X-Ray Diffraction

Commonly referred as XRD, this technique is of utter importance for it allows the determination of a material's crystalline structure. It makes use of a monochromatic radiation, of fixed and know wavelength (λ), the is beamed over a solid sample (the studied material) that is mainly constituted of randomly oriented crystallites [111].

When the beamed radiation hits the material framework, it is expected that part suffers a diffraction phenomenon, which only occurs along very defined directions that follow angles of *2θ* from that of the beamed radiation (Figure 1.9).

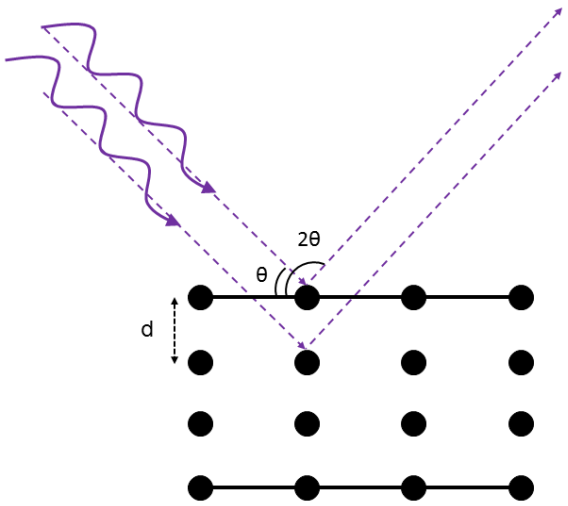

Figure 1.9 | XRD schematics. Single λ radiation incidence over a crystalline structure of defined interplanar distance (d), at a defined incidence angle θ.

As it is clear from Figure 12, this *2θ* angle is wavelength and lattice dependent. This results in a relationship that is translated into Bragg's Law (Equation 1).

$$n\lambda = 2 \cdot d \cdot \sin\theta$$

Equation 1 | Bragg's Law

Where, an integer multiple of the beamed wavelength (nλ), is related to the previously mentioned *θ* angle of the incident radiation and the crystal lattice distance (d), given by the *hkl* Miller indexes for crystallographic planes.

Summarizing, due the fact that X-rays are of the same order of magnitude as that of crystallographic bonds and that diffraction phenomena occur, with XRD it is possible to determine a set of unique and specific characteristic that constitute the fingerprint of a crystalline material. These characteristics are the establishment of diffraction planes, interplanar distances (d) and atomic density [111].

1.3.2 (Scanning & Transmission) Electron Microscopy

Both Transmission and Scanning electron microscopy (TEM and SEM, accordingly) are two high resolution techniques, of utter importance, that use a beam of electrons to produce high-res images of materials from the scale of a micron down to several angstroms. The beam of electron interacts with the sample, that must be somehow conductive, producing a flow of transmitted electrons from the same sample that are afterwards collected and transformed into an image.

Whilst, transmission ones direct a broad static beam through an ultrafine sample, allowing us to have an idea of the structure of a material and its inner disposition [112], scanning microscopes are able to, using a sharp beam that scans the sample line by line, create three-dimensional images that are perfect for the determination of particles shape and size [113].

1.3.3 Dynamic Light Scattering and Zeta Potential

Dynamic light scattering (DLS), also referred as Quasi-Elastic Light Scattering (QELS), is a well-established technique when measuring the size and size distribution of molecules / particles within the submicron region (nanometre).

The DLS allows for the characterisation of particles, emulsions or molecules, that have previously been dispersed or dissolved in a liquid. The Brownian motion of these particles in a suspension causes laser light to be scattered at different intensities. The analysis of these intensity fluctuations yields the velocity of the Brownian motion and hence the particle size, using the Stokes-Einstein relationship [114].

Additionally, the Zeta potential is a measure of the electrostatic interactions between particles, and is one of the fundamental variables known to affect stability. Its measurement brings detailed insight into the causes of dispersion, aggregation or flocculation, and can be applied / modulated to improve the formulation of dispersions, emulsions and suspensions [114].

1.3.4 Fourier Transform Infrared Spectroscopy

The Fourier transform infrared spectroscopy (FT-IR) technique is used to obtain the infrared absorption or emission spectra, associated with the vibration of intramolecular bonds. This analysis can be applied to either solid, liquid or gas samples and allows for the prediction of molecular structures and validate certain binding stretches.

1.3.5 UV-Visible Spectroscopy

Maybe the most used spectroscopic technique, it takes into account the interaction of UV and Visible radiations with molecules, namely their absorption and emission promoted by the passage of electrons from their fundamental to excited states, vice-versa.

Currently the quantification of this interaction is given by the Lambert-Beer Law that correlates the concentration of a certain molecular specie, in solution, with the intensity and composition of the outcoming spectrum (Transmittance), or its difference to the initial incident radiation (Absorbance). Absorbance and concentration are then directly proportional to each other and follow a linear tendency (Equation 2), within a firm window usually given by a calibration curve.

$$Abs = \varepsilon \cdot b \cdot C$$

Equation 2 | Lambert-Beer's law.

Where, ε represents the molar extinction coefficient ($M^{-1}cm^{-1}$), b the optical pathway (cm) and C the above-mentioned concentration of the sample, in solution.

1.3.6 ^{1}H / ^{13}C Nuclear Magnetic Resonance Spectroscopy

It is well known that all nuclei have an electrical charge, associated with an internal magnetic field, and that may or may not have spin. The NMR technique promotes an insight over these assets' behaviour by using an external magnetic field as energy source, that promotes an energy transfer (equivalent to radio frequencies) and a transition between lower and higher energy levels.

This technique is usually applied to either ^{1}H or ^{13}C isotopes that, contrary to even nuclei isotopes (e.g. ^{12}C), have an overall spin. However, the interactions of such nuclei within molecules differs from that of single atoms due the additional influence of neighbour nuclei and electrons magnetic fields, that result in shifts from their typical absorption frequency. This obligates for the establishment of a reference resonant frequency (usually that of tetramethylsilane, TMS), from which the mentioned shifts can be quantified [115].

Differences, in a part-per-million (ppm) scale, from the ground TMS point are displayed as peaks and give insight on nuclei positions and molecules structure [116].

1.3.7 BET (Brunauer-Emmett-Teller) / BJH (Barrett-Joyner-Halend) Theory

The BET (Brunauer-Emmett-Teller) theory, an extension of the Langmuir theory, tries to explain the physical adsorption of gas molecules on a solid's available surface and works as an important tool for the measurement of a material's specific surface area, porous volume and mean pore size [117].

Whilst Langmuir theory applies for a monolayer molecular adsorption, BET theory favours the multilayer adsorption following three main hypothesis: 1) infinite layers of physically adsorbed molecules, over a solid; 2) There is no interaction between each of those layers; 3) the Langmuir theory is applied to each of the layers [117]. This results in the BET equation presented in Equation 3.

$$\frac{1}{v\left[\frac{P_0}{P}-1\right]}=\frac{c-1}{v_m c}\cdot\frac{P}{P_0}+\frac{1}{v_m c}$$

Equation 3 | BET equation.

Where, P and P_0 are the saturation and the equilibrium pressures of adsorbates, at a specific adsorption temperature, v is the adsorbed quantity (volume) of adsorbate, v_m the adsorbate quantity adsorbed by monolayer, and c the BET constant that relates heats of consecutive adsorbed layers with the adsorption temperature.

The tracing of the whole sorption process results in the elaboration of isotherms able to translate both adsorption and desorption phenomena. With the adsorption branch it is possible to, applying the BET theory, define v_m and consequently the total surface area (S_{Total}) and specific surface area (S_{BET}), as given by Equation 4 and Equation 5 [117, 118].

$$S_{Total}=\frac{Ns}{v_m}$$

Equation 5 | Determination of the total surface area (S_{total}).

$$S_{BET}=\frac{S_{Total}}{a}$$

Equation 4 | Calculus of the BET specific surface area (S_{BET}).

Where N is Avogadro's number, s the adsorption cross section of the adsorbing species, V the molar volume of the adsorbate gas and a the mass of the solid sample or adsorbent.

However, only BJH (Barrett-Joyner-Halend) analysis, a pore size distribution determination method that uses the N_2 desorption branch, at 77 K (liquid N_2), is able to relate the amount of adsorbed gas removed from the pores of the material to the size of the mesopores. This extension of BET technique uses a proper modification of Kelvin equation, where liquid density, evaporation phenomenon and pore size (mesopores) are taken into consideration [118, 119].

Isotherms are visual representations of an existing relationship, at fixed temperatures, between adsorbate's partial pressure and the adsorbed quantity. These are usually determined experimentally

through processes of degasification of solids and are classified according to the adsorption mechanism at work. These are currently classified in six types (Figure 1.10) and are as follows:

Type I: Known for reaching a saturation stage at low relative pressures, this type of isotherm is strongly linked to microporous materials and for that reason with chemical adsorption. This stage is associated with the total charging of micropores and is representative of the total microporous volume of a material.

Type II and III: Both types of isotherms are common when dealing with multi-layered adsorption and can either be observed in non-porous materials, macroporous materials or mesoporous materials. Their existence is strongly dependent on the solids geometry and can only occur when the former compels condensation to only happen at its specific pressure.

Type IV and V: Distinguished by their defined stage at high relative pressures, this type of isotherms is related to the phenomenon of capillary condensation, a unique feature of mesoporous materials. The stage is the result of condensation phenomena induced by relative pressures below 1 and can change according to mesopores shape and size.

Type VI: This last family of isotherms is known by its step-by-step shape and is connected to layer-by-layer adsorption phenomena on non-porous uniform surfaces.

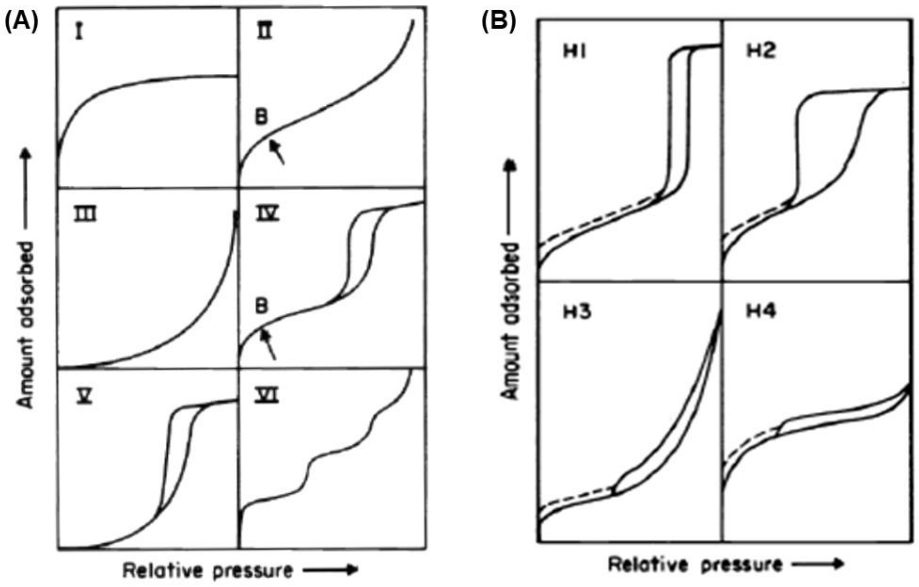

Figure 1.10 | Representation of **(A)** all six types of isotherms and **(B)** types of hysteresis. Adapted from [107]

Another important feature worth mentioning, are the existing hysteresis on Type IV and V isotherms usually associated with the different condensation and evaporation pressures during the adsorption-desorption cycle [120]. According to *IUPAC* there are four families of possible hysteresis:

H1 Type: Distinguishable for their almost vertical parallel branches, this type of hysteresis is usual in rigid porous materials made of the agglomeration of near-to-spherical particles of uniform shape and

size. Their associated standard type of pores is of pipe-like shaped cavities. Pore distribution is also known to influence hysteresis arrangement, with narrow distributions favouring more vertical branches.

H2 Type: With a broad and well-defined plateau, and a near to vertical desorption branch, this hysteresis family is usually found on rigid materials and is strongly linked to condensation and evaporation phenomena on cage-like mesoporous structures.

H3 Type: Known for the existing asymptotic progression of both adsorption and desorption branches towards relative pressures equal to 1, this kind of hysteresis is a consequence of the layered disposal of non-rigid particular aggregations that give origin to fissure-like pores.

H4 Type: This family of hysteresis usually present both adsorption and desorption branches horizontally parallel to each other for a broad range of relative pressures and are connected to fissure-like pores. Its similarity to type I isotherms points out the existence of micropores in a material's structure.

1.3.8 Bradford Protein Assay

Developed by Marion M. Bradford, the Bradford assay, a colorimetric protein assay, bases itself on an absorbance shift of the Coomassie Brilliant Blue G-250 dye (Figure 1.11).

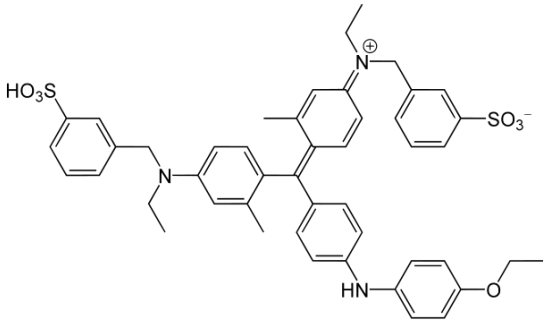

Figure 1.11 | Coomassie Brilliant Blue G-250 dye native form.

In detail, the usually brownish-red form of the dye (native form) is converted into its bluer form, after binding to the assayed protein. The binding promotes the formation of a strong, noncovalent complex with proteins' carboxyl groups, by Van der Waals forces, and amino groups, through electrostatic interactions [121].

During the formation of this complex, the brownish-red form of Coomassie dye creates an electrostatic interaction with the ionisable groups of the protein, causing a disturbance on the protein's native state, exposing its hydrophobic wells. Whilst these wells, present in the protein's tertiary structure, bind non-covalently to the non-polar region of the dye, via van der Waals forces, positive amine groups are moved to the proximity of the negative charge of the dye. Consequently, the bond is further strengthened by a second ionic interaction between dye and protein [121].

Therefore, the stabilisation of the blue form of Coomassie dye, by proteins' binding, allows for the measurement of protein concentration by estimation of the amount of complex in solution through simple absorbance readings, against a standard curve.

The brownish-red cationic (unbound) form has an absorption spectrum maximum at 465 nm, while the blue anionic (bound) form of the dye has an absorption spectrum maximum at 595 nm. The increase of absorbance at 595 nm is proportional to the quantity of bound dye, and hence to the total concentration of protein present in the sample [121].

1.3.9 1D PAGE Electrophoresis

One dimension polyacrylamide gel electrophoresis (1D PAGE) is one of the most commonly employed techniques when separating macromolecules such as DNA, RNA, or proteins.

Briefly, 1D PAGE electrophoresis is a size exclusion technique, where equally charged macromolecules are separated by their molecular weight when under a well-defined electric field. The mobility of a charged molecule is directly proportional to its net charge and resistance to motion through a certain medium, with smaller molecules running longer distances than larger ones.

To ensure that the molecules of interest are homogeneously charged an anionic detergent is used. Sodium dodecyl sulphate (SDS) is the elected detergent for this step, as its molecules have a net negative charge within a wide pH range, when dissolved. The binding of SDS to polypeptide chains is molecular weight dependent and the presence of negative SDS charges has a denaturing effect over proteins, as complex tertiary proteins' structures tend to be destroyed. This results in rod-like negatively charged proteins, whose mobility depend singly on their molecular weight [122, 123].

Separation of homogeneously charged proteins occurs through a polyacrylamide meshed gel, that can be optimised to meet the size range of molecules present in the analysed sample. The loading of such negatively charged proteins onto the gel is performed at its interface, where the sample is neatly stacked in a narrow band. Since smaller proteins usually tend to start their migration through the grid, even before the whole loading of the sample, the polyacrylamide gel is created in two layers commonly designated by 'stacking gel' (upper, smaller layer) and 'running gel' (bottom, larger layer) [124, 125].

Both stacking and running gels contain a buffer made of HCl and have an exact pH of 6.8 and 8.8, respectively. Besides, reservoirs at the top and bottom of the whole gel are dunked in a 8.3 pH buffer solution made of tris base and glycine [124, 125]. During electrophoresis, current flows through the gel with the assistance of moving negatively charged molecules or ionic species.

In first instance, since only about 10% of glycine molecules are negatively charged at buffer solution's pH 8.3, the current is mainly carried by Cl^- ions present in the stacking buffer. This leads Cl^- species to move towards the bottom of the stacking gel, ahead of proteins, and SDS-coated protein molecules to be sandwiched between slower glycine molecules (above) and faster Cl^- ions (below) [124, 125]. With this we make sure that, by the bottom of the stacking gel, samples are compressed into a narrow loading band ready to enter the running gel; thus, achieving a better separation in the next phase. With the continuity of the process, as proteins move into the running gel, glycine molecules in the resolving gel buffer at pH 8.8 become negatively charged and move faster than in the stacking gel. Nearly keeping up with the Cl^- ions, glycine molecules leave proteins trailing behind [125]. Thus, proteins entering the

running gel carry now the current flowing through the gel, with their mobility a function of molecular size alone. With the 1D PAGE electrophoresis run, proteins are separated according to their molecular weight and the gels stained (with Coomasie Blue dye R250) for further protein size determination, protein identification, sample purity examination, disulphide bonds identification or protein quantitation.

2

Objectives

2.1 Focus

Considering all previous statements, here in it is proposed the development of a nanometric silica mesoporous solid-state system that allows for the easy and tuneable extraction of proteins from complex biological media, with the assistance of a N-hydroxysuccinimide (NHS)-modified Rhodamine B chromophore (**RhNHS**) [126]. Detection and extraction of metal ions from aqueous media is also one of the main objectives of this work.

Based on already defined synthetic pathways [16], we aim to produce and tune SBA-16 silica mesoporous nanoparticles, whose diameter ($d < 1000$ nm) and pore-size ($d > 10$ nm) have been modulated by changing reaction temperature, swelling agent concentration and surface functionalisation [16, 31].

The well-known NHS interaction and affinity towards proteins' amine groups and its tendency to rapidly form relatively stable amide bonds with proteins (in approx. 30 min, at pH 7.4 and room temperature) [127, 128], are assets that we looked forward to put to work along with an already high mass transfer of SBA-16 silica network of mesoporous. Allying both mechanisms it was though that it was possible to develop a device capable of selectively extract proteins from either biological pure or complex samples; in spite of media conditions (pH and temperature), SBA-16 pore size, surface zeta-potential [129], NHS-chromophore concentrations and proteins isoelectric point and diameter (Figure 2.1).

The once adsorbed **RhNHS** chromophore, is to have the two-way function of serve as an optical probe to easily track protein fluxes and act as a bonding site where proteins are to be locked and stored (Figure 2.2).

This system has its advantages, since it is based on a cheap solid-state material that can easily be isolated and dried. Therefore, we hope it might still find some applications within purification techniques (using of both size-exclusion and affinity phenomena together), dry storage (within mesoporous structures with surface-areas of approximately 1000 m^2g^{-1}) and fast non-evasive analysis.

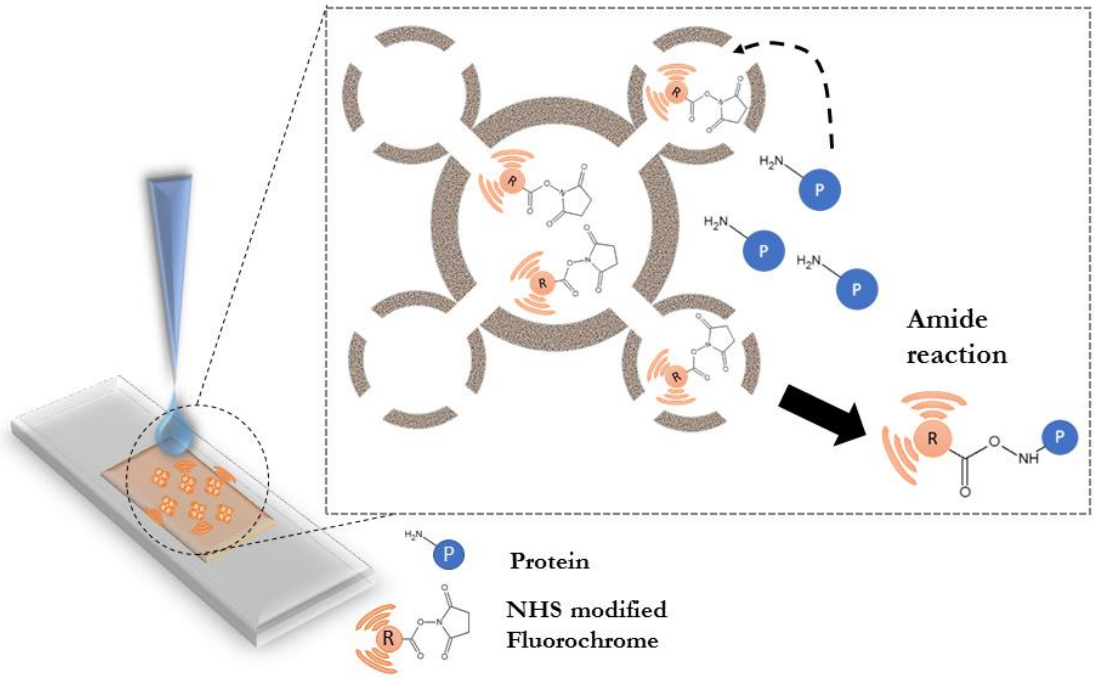

Figure 2.1 | Schematic representation of the here in proposed SBA-16 system for proteins extraction from biological media, using an NHS-modified chromophore.

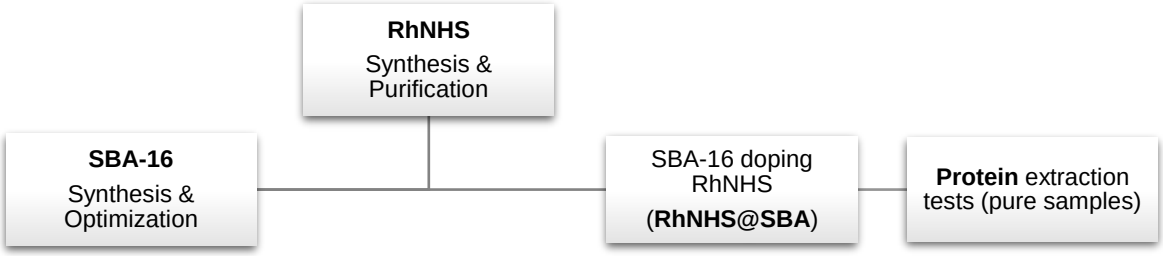

Figure 2.2 | Brief schematics of the synthetic path of the here in proposed system.

Extending the systems application range to the environmental field, we sought to make the very same SBA-16 mesoporous material, now doped with a porphyrin chromophore (**L5,** 1198.46 g/mol) with a strong metal affinity heme group, capable of sensing and extracting toxic metal ions (e.g. Hg^{2+}, Cu^{2+} and Pb^{2+}), from aqueous solution. The **L5 porphyrin** is a cationic porphyrin with high selectivity towards Hg^{2+}, Cu^{2+} and Pb^{2+} ions and was synthetised in Prof. Graça Neves group, by Dra. Sónia Pires. It should be stated that this work is in collaboration with the Organic Chemistry Group, PNQA, from the University of Aveiro, Portugal.

This same compound is to be encapsulated within SBA-16 nanocages, through physical adsorption, and to be used as a reversible solid-state detector/extractor (making use of its coordination chemistry) of toxic metallic ions from contaminated media. Additionally, the mechanism is also to be compared with a similar one that uses the previously mentioned **RhNHS** and its reversibility tested (Figure 2.3).

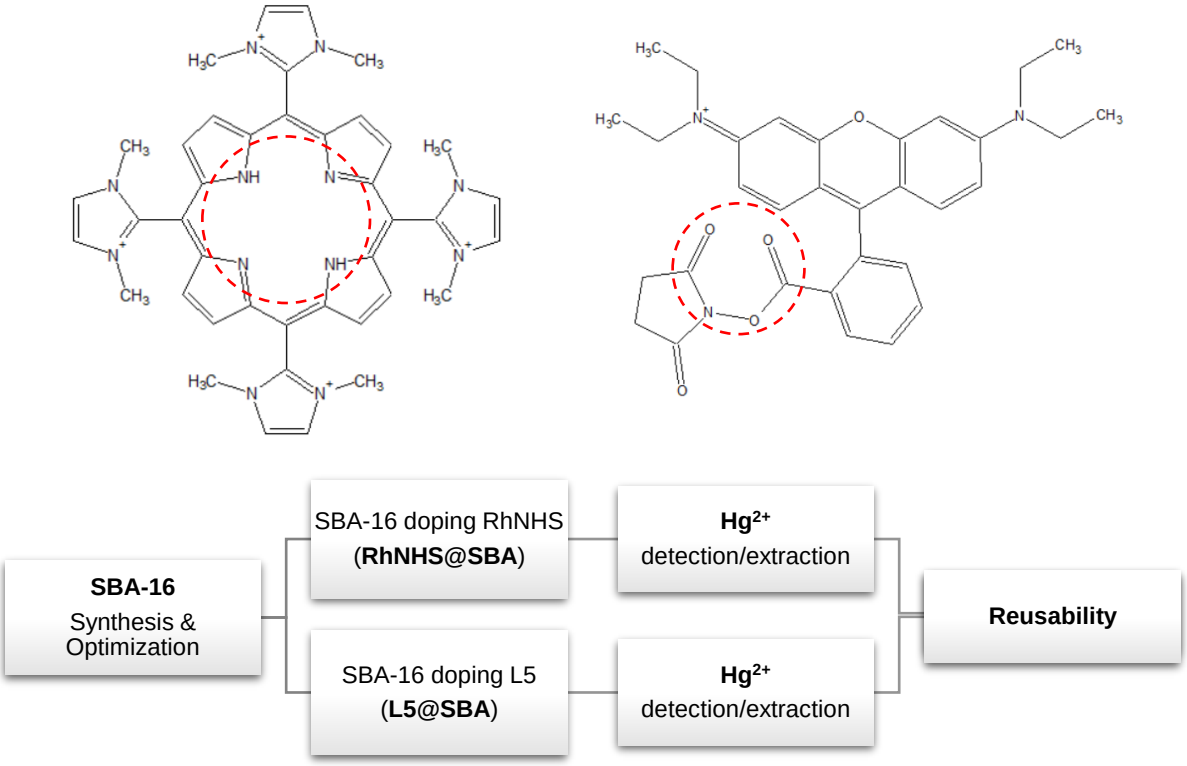

Figure 2.3 | Brief schematics of the here in proposed device, from its synthesis to doping - with **L5** porphyrin (upper left) and **RhNHS** (upper right) - and application. Coordination centres signalled by red dotted line.

2.2 Structure

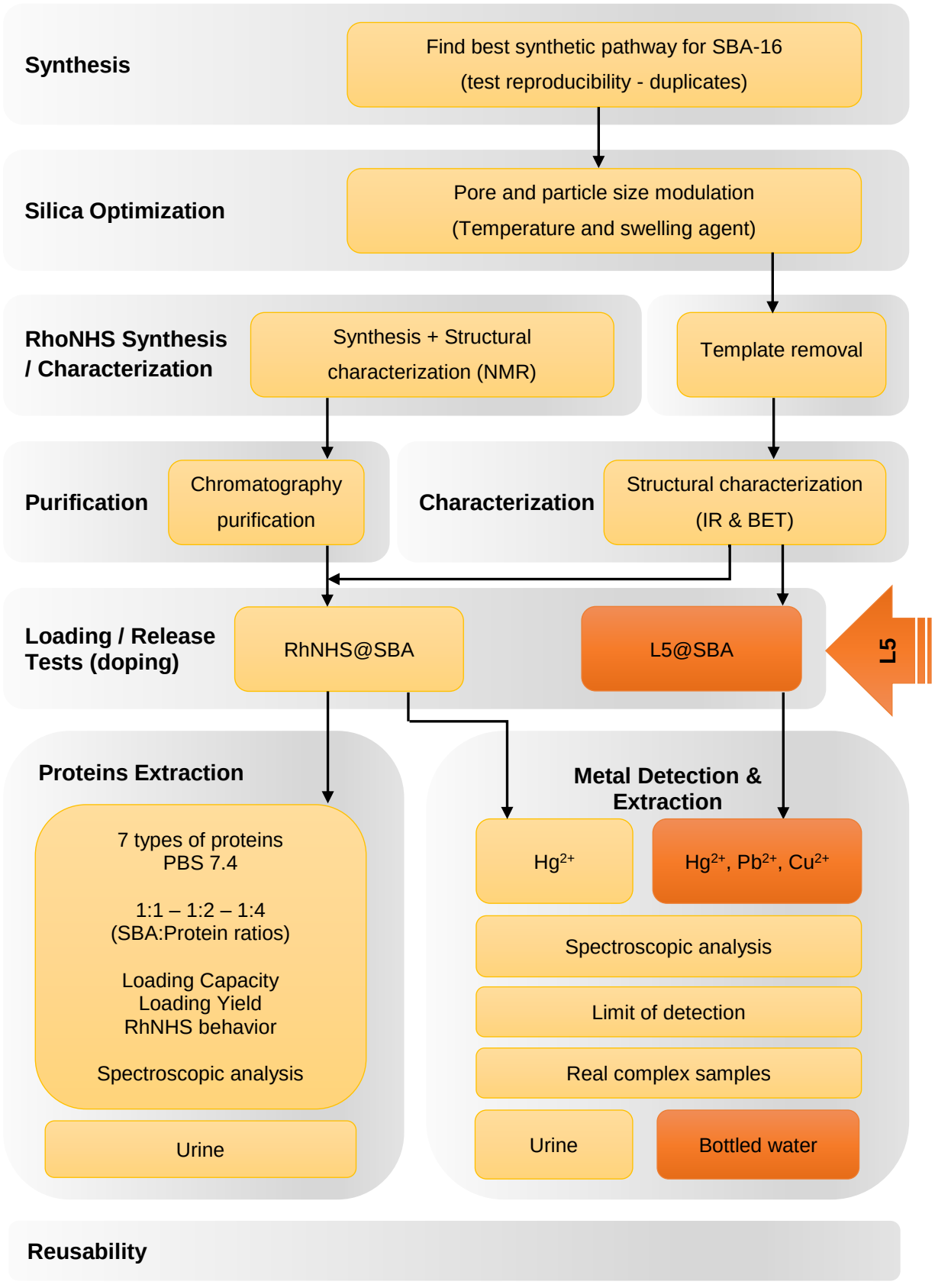

3

Synthesis and characterisation of pluronic (SBA-16) mesoporous nanoparticles

In this first step, the elaboration of an optimal sol-gel synthetic pathway of SBA-16 silica nanoparticles is described, with further understanding over its structural arrangements and assets towards an optimal interaction with molecules or biomolecules. Optimisation of such assets is also discussed with focus on its colloidal properties, such as in-solution stability, zeta potential, particle size and pore width.

Keywords: SBA-16, silica nanoparticles, synthesis, pore size, zeta potential

3.1 Synthesis

In light of previews statements and as a first step towards the elaboration of the aimed system, we sought the production of solid SBA-16 mesoporous silica particles, within the nanometric range, whose pores could be easily modulated to the right size (over 10 nm) for further internalisation of proteins or other biomolecules. Due to the relative low number of reported sol-gel synthetic methodologies for cubic-phased SBA-16 mesoporous silica materials [26], this work based itself on three sol-gel SBA-15 synthesis approaches reported by Katiyar et al. [16], dos Santos et al. [31] and Zhao et al. [3], denominated as **Method 2**, **Method 1** and **Method 0**, respectively. All materials were characterised according to both its structure (through, IR spectroscopy and XRD analysis) and interactive assets (zeta potential, particle size and pore width).

These methods, thoroughly detailed in Section 7, landed on a cooperative assembly between the organic amphiphilic Pluronic F127 ($EO_{106}PO_{70}EO_{106}$) surfactant and inorganic silica precursors (TEOS and TMOS) for the production of spherical, well-dispersed, nano to micrometric silica materials. Acidic conditions were used on all approaches, as these are known to promote lower condensation rates of silica precursors over still assembling surfactant micellar structures [3, 4, 14, 16]. Moreover, since similar morphologies were intended, stirring was kept equal for all methods (at approximately 500 rpm) during their early reaction stage (also known as ripening), as the former has been reported as an

important morphology modulating variable, with smaller particle diameters being favoured by more intensive stir rates [130].

Initial trials were performed with aging steps at 80 ºC and under static conditions (except for Method 0 where stirring was kept), without any use of pore size modulating agents (e.g. TMB), as similar pore sizes of between 5 - 10 nm were aimed [3, 4, 16, 31].

All SBA-16 samples were obtained in the form of dry white powders and identified according to its synthesis original method: **SBA-16 M0** for Method 0, **SBA-16 M1** for Method 1 and **SBA-16 M2** for Method 2. Attained amounts of as-synthesised SBA-16 material and silicon-based weight yields are summarised in Table 3.1.

Table 3.1 | Reaction yields, in % (wt.), based on initial weighted silica precursors, and corresponding SBA-16 mass.

SBA-16 M0	Yield (% wt.)	35 %
	Total mass (mg)	299.8
SBA-16 M1	Yield (% wt.)	63 %
	Total mass (mg)	242.4
SBA-16 M2	Yield (% wt.)	58 %
	Total mass (mg)	580.5

Although no thorough analysis was found in literature over reaction yields, it is interesting to highlight the similarity between both M1 and M2 techniques yields (~60%). In a matter of fact, a careful study on both synthetic procedures not only showed us a similar core between the two methodologies, but also that surfactants and silica precursors initial masses in Method 1 were half of that needed in Method 2. As it is evident, this reverberated on final recover product masses with SBA-16 M1 approximately half of that of SBA-16 M2. This corroborated already reported conclusions that the additional insertion of co-surfactants (e.g. CTAB) and co-solvents (as EtOH) serve only as morphology modulators and do not interfere on conversion yields [16].

At this stage, no valid comparison was done between Method 0 and the remaining methods as different initial conditions were used; namely, the use of TEOS as silica precursor and a TEOS : F127 (wt.) ratio of approx. 2, against the usage of TMOS as silica source and a TMOS : F127 ratio of approx. 3. The last of which, playing a significant role on particles structure and being a possible origin of future observable disorders [131, 132].

Nonetheless, an apparent 35 % (wt.) yield for Method 0 technique stands way below the previously reported ~98 % yields for SBA-15 [3, 26] and might result of a handling error during washes, with some of the final product being loss during phase separation (pellet from supernatant.). This occurrence could also have been aggravated by using methanol and water as washing solvents, since the extensive usage of alcohols, along with water, has been reported to promote destabilisation and erosion of silica mesostructures, with consequent shrinkage and reduction of surface area [132]. Moreover, the usage of a surfactant (F127) different from that reported in literature (P123) might also the source of such

discrepancy. In this way, an improvement on the yield of Method 0 is mandatory, by submitting it to future optimisation procedures.

However, as in most works regarding silica mesoporous structures, a template removal is also essential for future applications as it cleans pores, widening pore diameters, and increases specific surface areas. Therefore, supported by the literature, template removal was achieved by means of an efficient ammonium nitrate ionic-exchange-based extraction [133] over the traditional calcination. It is worth noticing that this last is known for easily encourage inter-particle condensation, loss of hydroxyl groups, future dispersion problems [51] and pore shrinkage [109]. Attained amounts of treated SBA-16 material and template removal yields are summarised in Table 3.2.

Table 3.2 | Template removal yields, in % (wt.), based on initial as synthesised dry-powder, and corresponding SBA-16 mass.

SBA-16 M0	Yield (% wt.)	83 %
	Total mass (mg)	249
SBA-16 M1	Yield (% wt.)	75 %
	Total mass (mg)	182
SBA-16 M2	Yield (% wt.)	74 %
	Total mass (mg)	428

The success of this template removal technique was confirmed by solid-state FT-IR analysis, with a significant decrease in transmittance intensity (%) on the F127 template characteristic 1342 cm^{-1} (in-plane, O–H bend) and 1279 cm^{-1} (CH_2 bending) bands [134]. For SBA-16 M2 samples, an additional decrease of intensity was also observed at 2835 cm^{-1} and 2915 cm^{-1}, matching the removal of the CTAB co-surfactant [135] (Figure 3.1).

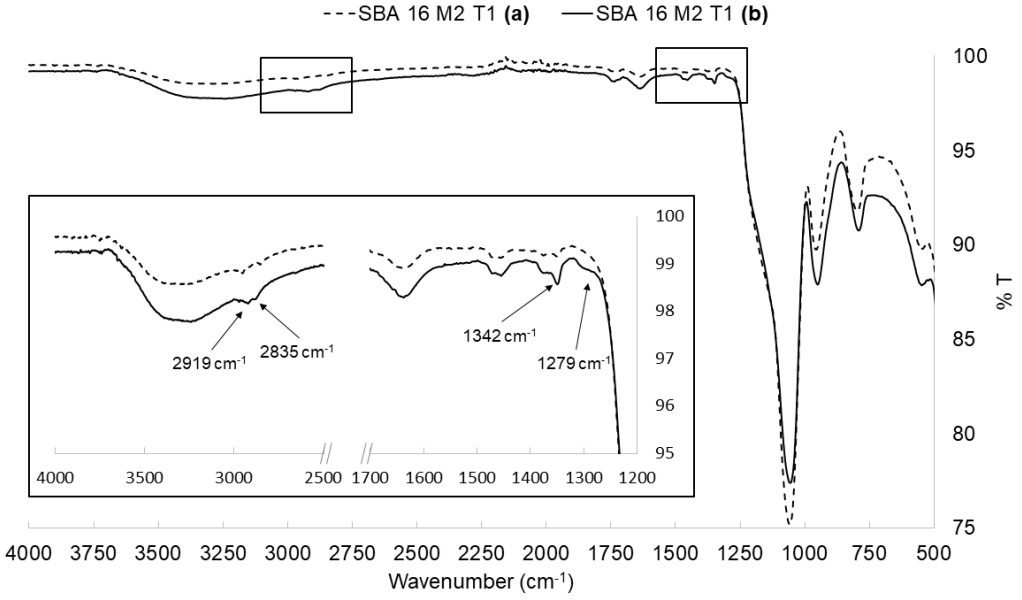

Figure 3.1 | FT-IR spectra of SBA-16 M2 T1 sample after (a) and before (b) template removal. A diminish in transmittance % (%T) is highlighted for F127 characteristic 1342 cm^{-1} and 1279 cm^{-1} bands; and for CTAB 2919 cm^{-1} and 2835 cm^{-1} typical bands.

Moreover, the employment of a FT-IR analysis allowed us too to confirm the successful synthesis of our SBA-16 mesoporous silicas, for they matched those already reported in literature for the same material [134, 136]. All synthesised SBA-16 materials FT-IR spectra are display in Annex I.

Notwithstanding, the processing of a template removal is also known to have significant influence on another important variable. The variation of particles stability is intrinsically correlated with its zeta potential, a measure of the surface net charge and thus a regulating factor towards a system's dispersion. Therefore, in a way to evaluate the consequences of a template removal over our particles stability, zeta potential measurements were performed, in triplicates, on all dry SBA-16 samples, with DMSO as a good dispersing media (Table 3.3).

Table 3.3 | Zeta potentials, after and before template removal, obtained by dynamic light scattering, in DMSO.

Sample ID	Zeta Potential ± σ (mV)
SBA-16 M0 w/ template	-26.6 ± 1.8
SBA-16 M0 w/out template	-13.5 ± 1.9
SBA-16 M1 w/ template	-19.1 ± 0.5
SBA-16 M1 w/out template	-17.1 ± 0.5
SBA-16 M2 w/ template	-42.8 ± 0.3
SBA-16 M2 w/out template	-27.3 ± 1.6

In accordance to literature, previously expected negative zeta potentials were obtained for silica nanoparticles [3, 60, 129], with M2 samples, both before and after temple removal, showing higher stability (more negative potentials) than those of M0 and M1. These results are consequence of a more efficient dryness of M2 samples.

From Table 3.3 we can also conclude that the removal of F127 surfactant has a general destabilizing effect on all SBA-16 samples and an aggravating one for M0 and M1 samples, with resulting zeta potentials bellow the considered stability zone of ±30 mV for silica nanoparticles. Zeta potentials of approximately ±30 mV, or higher, are know from literature to be part of good colloidal solutions, conferring better dispersion properties and less susceptibility to particles flocculation and deposition. This last list of assets is confirmed through dynamic light scattering (DLS) when measuring the average hydrodynamic particle size.

Once more, measurements were done in triplicates and with DMSO as dispersion medium. As predicted, strong agglomeration issues are visible for both M0 and M1 samples, with low zeta potentials (Table 3.4) corresponding to large unstable dimeter structures. Conversely, M2 nanoparticles with potentials of near to -30 mV after template removal presented stability enough to counter particles agglomeration, as smaller particles of approximately 1733 nm (micrometric) were obtained. It is interesting to emphasize that the washing of any template molecules present in particles surface is itself a stabilizing action since it reduces any pre-polymerisation between F127 surfactant molecules and

consequent aggregation issues [29]. This phenomenon allied to still strongly negative zeta potentials are the main reasons why M2 systems are able to reduce aggregation and produce better colloidal solutions.

Table 3.4 | Hydrodynamic average pore diameters, after and before template removal, obtained by dynamic light scattering, in DMSO.

Sample ID	$d_{Hydro.\ avg.}$ w/ template (nm)	$d_{Hydro.\ avg.}$ w/out template (nm)
SBA 16 M0	4623	4386
SBA 16 M1	1727	2012
SBA 16 M2	3518	1733

Unfortunately, it should be referred that high polydispersity indexes (PdI) were also obtained for all measurements and that the above diameters are not the exact measure of our particles size. Additionally, zeta potential measurements for M2 samples were once again repeated, this time in water, since the herein sought device is supposed to act in aqueous media (be it in protein extraction or in metal ions detection and extraction). Opportunely, no significant changes were observed with this swap of solvent, as an acceptable -25 mV zeta potential was recorded (not far from the -27 mV in DMSO).

Notwithstanding, we are safe to admit that from all synthesised silica nanoparticles, SBA-16 M2 particles were the best candidates for the development of well dispersed systems for later extraction of other chemically and biochemically active molecules.

With a now well set synthetic pathway, we proceeded to the employment of reproducibility tests. However, as mentioned above, we were not able to reproduce the unknown occurrence of total evaporation of the reaction solvent, for this happenstance was a consequence of an uncontrollable uncovering of the reaction pot. A thorough analysis on the reaction mechanism revealed that the use of TMOS as silica precursor promoted the production of methanol, as by-product, (similar to TEOS producing ethanol), which by instance has a boiling point below the highest temperature used during the reaction.

To outcome this unknown drawback, the reaction was made under refluxing conditions and the M2 synthetic pathway repeated twice. Again, this time no TMB was used as pore swelling agent. It should be noted that the formerly synthesised sample was now denominated as **SBA-16 M2 T1** and the new ones as **SBA-16 M2 T2** and **SBA-16 M2 T4**.

Both samples followed the same methodology used above. Template removal was confirmed after FT-IR analysis, having a similar response to that seen for **T1** samples (Spectra in **Annex I**). The effect of this last stage over morphological and mobility assets of the resulting particles was again corroborated with the use of DLS to determinate both hydrodynamic particle size and zeta potential, in H_2O. All previously analysed parameters were determined for both new **T2** and **T4** samples and are listed in Table 3.5.

Table 3.5 | Comparison table between main parameters of SBA-16 M2 T1, T2 and T4 synthesis. No hydrodynamic diameter was included, since PdI values were of approximately 1 and obtained diameters above the range of measurement of the apparatus.

	T1	**T2**	**T4**
Reaction Yield (%wt.)	58 %	63 %	71 %
T. Removal Yield (%wt.)	74 %	90 %	78 %
Total dry SBA-16 mass (mg)	428	583	563
Zeta potential ± σ (mV)	-27.3 ± 1.6	-22.2 ± 1.6	-18.9 ± 0.6

No hydrodynamic values were included and compared, since high PdI values (near to 1) were obtained once more. From Table 3.5 we can conclude that the introduction of a refluxing mechanism causes but small fluctuations on the obtained results for T2 and T4, when compared to T1. Slightly lower values of T2 and T4 zeta potentials could be the result of a non-total dryness of the reaction pot and consequent non-calcination of template molecules. Nonetheless, pairing both T2 and T4 results it was clear that the use of refluxing conditions, during the whole reaction, was an essential improvement to ensure the system's reproducibility.

3.2 Pore Modulation

As stated before, the above-developed synthesis based themselves on the postulate that the obtained silica nanoparticles confined in their structure mesopores within the range of 5 to 10 nm. Namely, Method 2 as processed above was focused on producing SBA-16 systems whose pore diameters were of 6 nm. Then, using the same method a pore enlargement was sought with the aid of swelling pore modulating agents. In this case, Trimethylbenzene (TMB) was used to promote the production of larger micelles that will eventually be the skeleton to all mesopores.

Focusing on a maximum pore width of 12.7 nm, as reported with Method 2, TMB was added to the reaction pot along with CTAB co-surfactant on a weight-based TMB : F127 ratio of 0.5. This modification on the protocol does not come alone, since an increase on the aging temperature is need, from the usual 80 ºC to 125 ºC. Notwithstanding, the aging time was kept identical.

Therefore, in light of the mentioned changes and following the synthetic Method 2 new samples were produced, in duplicates, and denominated of **SBA-16 M2 T3** and **SBA.16 M2 T5**. Synthesis results are summarised on Table 3.6. The acquirement of larger amounts of final dry powders is the result of a deficient dryness of both materials, as some water molecules were still entrapped within the mesoporous matrix during weighting. Luckily, this was a pre-confirmation of the successful production of larger pore materials, for larger pores imply larger specific surface areas and thus larger amounts of adsorbed molecules.

Table 3.6 | Comparison table between main parameters of SBA-16 M2 T1, T3 and T5 synthesis. No hydrodynamic diameter was included for T5 samples, since PdI values were of approximately 1 and obtained diameters above the range of measurement of the apparatus.

	T1	**T3**	**T5**
Total dry SBA-16 mass (mg)	428	940	1086
Zeta potential ± σ (mV)	-27.3 ± 1.6	-21.3 ± 0.7	-9.1 ± 2.8
***d* *Hydro. avg.* w/out template (nm)**	1733	304	-

In light of the above collected results, it is obvious the presence of a more porous material in T3 samples as almost no aggregation occurred. This affirmation is made on the basis of the already reported correlation between pore size and surface charge, that results from the coupling of an internal zeta potential with its external homologous when pores are penetrated with liquid [137]. In this way particle's stability is increased, even though no changes were observable on the external potential.

The determination of T3 porous structure, surface area, pore size and available porous volume was conducted through a N_2 physio sorption technique, with later understanding by the application of the BET / BJH theory. T2 and T1 porosity was also verified with the same technique with the aim of not only understand their true structure and morphology, but also corroborate the reproducibility of the whole process. The resulting N_2 isotherms, at 77K (Figure 3.2) showed distinct tracings, typical of isotherms of type IV and type II.

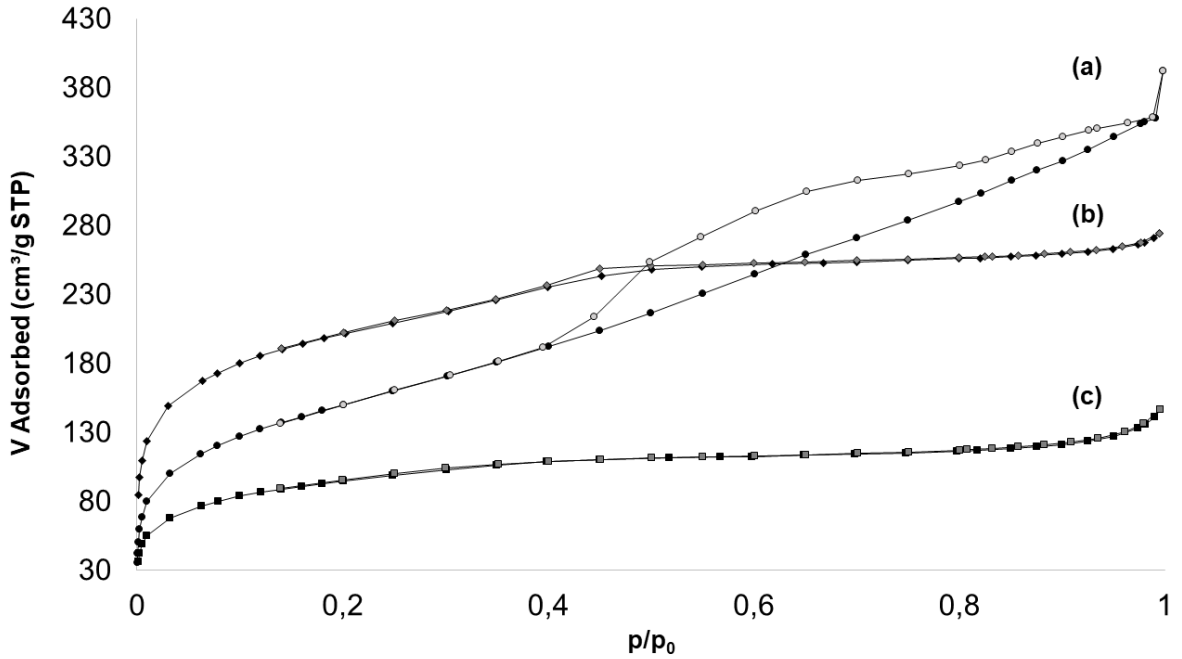

Figure 3.2 |N2 physio sorption isotherms, at 77 K, for (a) SBA-16 M2 T3, (b) SBA-16 M2 T1 and (c)SBA-16 M2 T2 samples.

Both SBA-16 M2 T1 (Figure 3.2-b) and T2 samples (Figure 3.2-c) were related with type II isotherms, indicating the presence of a mesoporous structure as was expected. However, the lack of significantly

observable hysteresis loops points out to a prevalence of micropores over macropores within the material's structure. Such result was corroborated by the obtained BJH pore widths that fall near to the currently definition of micropores (~2 nm) with approximately 3 and 4 nm, for T1 and T2 samples respectively. Notwithstanding, T1 isotherm presents a hysteresis that, although small, is shaped like a H2 type hysteresis, characteristics of cubic-phase like mesoporous structures. In addition, the existence of a gap between both plateaus is representative of the different total porous volume of each material, with T1 and T2 samples having a total of 0.4 cm^3/g and 0.2 cm^3/g, respectively. Specific BET surface areas (S_{BET}) of 730.6 m^2/g and 342.6 m^2/g (again, for T1 and T2 respectively) are a function of the above mentioned porous volumes and follow then the same tendency. A quick comparison with the results reported by Katiyar *et al* lead us to conclude that the employment of refluxing conditions might be behind the diminishing of the available specific surface area, since the non-refluxing T1 material S_{BET} was of the same magnitude as the 756 m^2/g by them obtained.

Conversely, T3 sample type IV isotherm show us a distinguishable hysteresis loop that might be qualified as in-between type II and type III. Whilst this kind of tailing ensured us that the material had indeed pores within the mesoporous range, it also taught us that their structure wasn't as rigid and defined as initially though. The existence of fluctuations along the hysteresis tracing is a representation of the conjugation of larger pores (mesopores) with narrow empty vesicles and their effect on evaporation / condensation phenomena of the absorbed N_2. Similar results have been reported before and associated with the possible existence of silica plugs or constrictions along the porous net [131, 132]. Both S_{BET} and pore width, of 533.6 m^2/g and 5 nm respectively, were below those reported SBA-15 nanoparticles of 768 m^2/g S_{BET} and 12.7 nm of pore size [16].

The acquirement of pore widths smaller than the initially expected is indeed a drawback on the whole process and may be the result of an inappropriate set of initial variables, namely the chosen surfactant or the TMOS : F127 ratio, as higher ratios often lead to the hydrolysis and condensation of TMOS (or TEOS) excesses within pores structure and the formation of the above mentioned obstructions or plugs. Additionally, the employment of a surfactant's solvent extraction can also be responsible for the acquirement of small pore sizes, for this technique is known to be a not-complete methodology, usually leaving remnants of surfactant molecules within porous structures [132, 138, 139].

Detailed reports on the BET / BJH assay can be found on **Annex II**.

3.3 Additional Characterisations

In a way to extent our knowledge on some structural and morphological aspects of the herein synthesised materials, additional X-ray diffraction (XRD) and scanning electron microscopy (SEM) analysis were performed.

As is visible in Figure 3.3, the XRD spectra of both T2 and T3 samples are in accordance to most reported amorphous silicas, with the characteristic SiO_2 broad band and its equivalent Bragg angle at 22 º present [140].

Further confirmation and information on the lattice arrangement and spacing would be possible should the collected spectra have started on 0º, for ,due to SBA-16 exhibiting larger cubic *Im3m* unit cells, important typical (110), (200), and (211) diffraction peaks are shown at smaller 2θ angles [3, 4, 14, 132, 139].

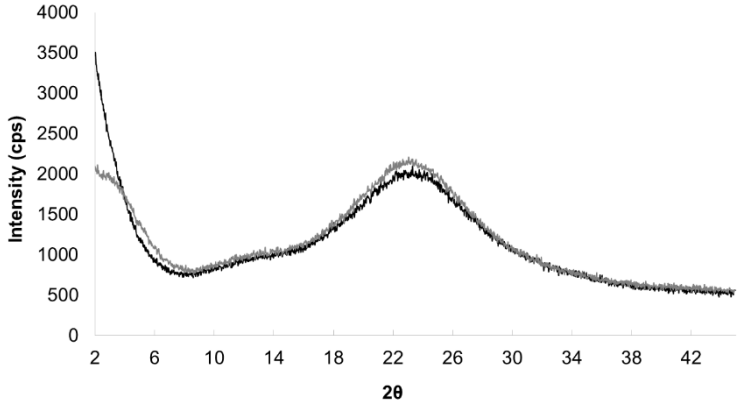

Figure 3.3 | XRD patterns of both T2 (grey) and T3 (black) samples.

Fortunately, the visible and significant gap between intensities at smaller 2θ angles, points out a difference on both materials structures. As reported from literature, higher intensities at smaller angles are often associated with the emptying of pores (enlargement of active pore width) and thus with larger vesicles in the materials lattice [3, 37, 38, 139]. Therefore, this information comes as a complementing result to those given by the physio sorption of N_2, where SBA-16 M2 T3 samples were confirmed to have larger pore diameters than SBA-16 M2 T2 ones.

SEM analysis were also performed on T2 and T3 samples and the resulting images (Figure 3.4) confirmed the presence of sphere-like nanoparticles with mean diameters of 31.9 ± 5.4 nm and 33.5 ± 6.4 nm, with high tendency to form large aggregates on the micron scale.

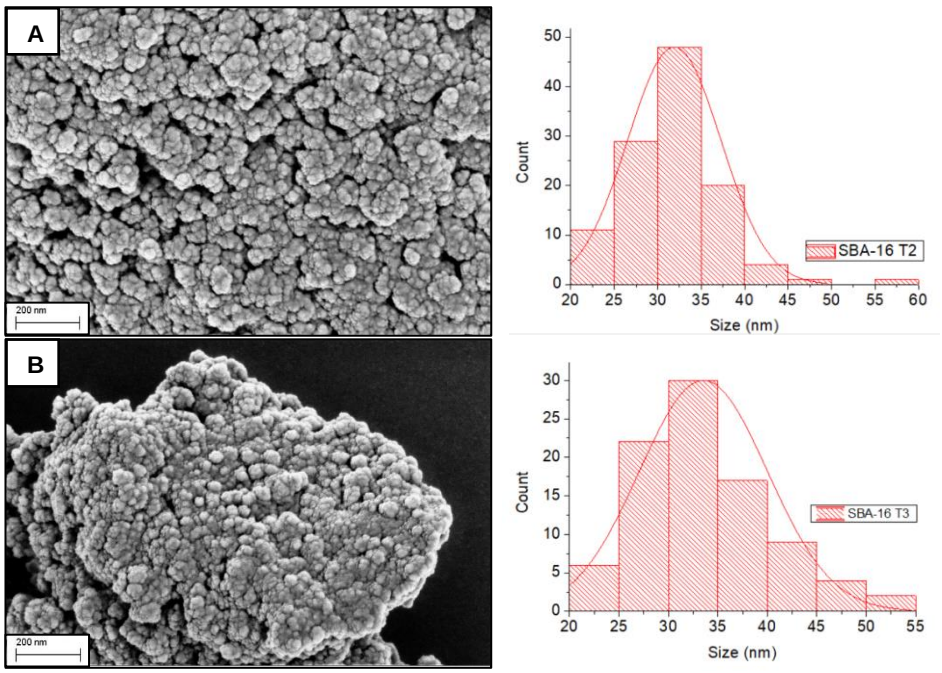

Figure 3.4 | SEM images and particle size distributions of both (A) SBA-16 T2 and (B) SBA-16 T3 samples.

3.4 Surface Functionalisation

The ever-present aggregation problem is a situation that may prove disadvantageous when proceeding to the adsorption of other substances, for it is known to cause significant reduction of the accessibility to the porous and a destabilizing effect over chemicals-particles interactions.

From literature, we know that when dealing with wet silica colloids, the excess water molecules interact with free surface hydroxyls groups by means of hydrogen bonds. When the hydrated particles get close, these water molecules draw on neighbouring particles and form bigger particles. This situation gets worst when, after a drying process, these hydrogen bonds give place to chemical bonds and rigid agglomerates appear [141].

In a way to overcome this difficulty a surface functionalisation, in deionised water, with sugar molecules was proposed, since sugars have been reported to, to some extent, have stabilizing effects over other nanoparticles interactions [108, 142, 143]. Therefore, three different sugar molecules (sucrose, fructose and trehalose) were used to try stabilizing SBA-16 M2 T2 nanoparticles. The validation of this model was given after DLS measurements of the resulting nanoparticles' average hydrodynamic size and zeta potential.

The effect of sugar concentration was also evaluated, with three different sugar : SBA ratios (wt.) of 1, 2 and 3 and following the functionalisation technique proposed by Zhou *et al* [143], detailed in Chapter 7. Batches of 5 mg of SBA-16 M2 T2 samples were used in all trials. All resulting data is thoroughly displayed in Table 3.7, and was collected after a one-time wash with deionised water.

Table 3.7 | Obtained average hydrodynamic diameters, zeta potentials and corresponding PdI for all T2 samples surface functionalisation, in water, with sugar molecules, at different sugar : SBA ratios of 1:1, 2:1 and 3:1. Sucrose, fructose and trehalose were used as sugar sources.

	$d_{Hydro.\ avg}$ (nm)	Zeta Potential ± σ (mV)	PdI
SBA 16 M2 T2	4703	-22.2 ± 1.6	0.612
1:1 ratio			
SBA 16 T2 Sucrose	851	-21.2 ± 1.3	0.419
SBA 16 T2 Fructose	879	-20.8 ± 0.7	0.466
SBA 16 T2 Trehalose	899	-24.7 ± 1.3	0.462
2:1 ratio			
SBA 16 T2 Sucrose	862	-28.6 ± 0.7	0.380
SBA 16 T2 Fructose	2148	-20.3 ± 1.1	0.372
SBA 16 T2 Trehalose	5215	-9.7 ± 0.6	0.922
3:1 ratio			
SBA 16 T2 Sucrose	864	-27.2 ± 0.1	0.466
SBA 16 T2 Fructose	1331	-29.4 ± 0.8	0.302
SBA 16 T2 Trehalose	2515	-26.4 ± 0.5	0.755

With a quick overview, we can sustain the idea that the addition of sugar molecules to the surface of our silica nanoparticles has a preferable stabilizing effect at lower concentrations, rather than for higher

ones. Significant changes on both hydrodynamic diameters and zeta potentials were visible, along with a decrease of all obtained PdI values, now near the acceptable range for monodispersed colloidal solutions of 0.3.

For ratio 1:1 the strong diminishing of particles diameter is a proof of the efficient surfactant effect that sugar molecules have when functionalizing our SBA surfaces and ripping apart any existing agglomerates. The resulting uniform hydrodynamic dimeters indicate the true proportion of our T2 nanoparticles places itself between 850-900 nm. Although there is a slight decrease on their zeta potentials, due to non-uniform coverage of the whole surface, a significant and uniform PdI is obtained around 0.45.

This tendency is inverted with the increase of total added sugar mass (2:1 ratio), promoting particles growth and destabilisation (decrease in zeta potential). Fructose and trehalose functionalised samples are evident examples of this situation, with the last facing strong aggregation issues between growing particles; translated into a zeta of -9.7 mV, a PdI of 9.22 and clusters of about 5000 nm. Notwithstanding, the growth of sucrose follows a total distinct predisposition, with almost no particle growth and its average size around the same 850 nm. This suggests that sucrose has reached an adsorption equilibrium plateau where all particles are evenly functionalised and repulsing each other equally. This is supported by the acquisition of a zeta potential of approximately -30 mV and a PdI of 0.38.

Regarding 3:1 ratio trials, fructose samples follow the same observed evolution of sucrose samples in 2:1 ratio, with a sudden increase in stability (a zeta potential of approx. -30 mV plus a PdI of 0.3) and a corresponding reduction of the average particle size to 1331 nm. This cut in size corresponds to the possible break of unstable aggregates, with further functionalisation with fructose that gives place to smaller and more stable particles able to repulse each other evenly. Concerning trehalose samples, although the formation of a possible plateau is visible through the diminishing of particle size and the increase in zeta potential, the lack of an acceptable PdI still marks an ongoing functionalisation process.

The capacity to reach a plateau is intrinsically related with functionalizing molecules size. With larger molecules usually occupying larger volumes above nanoparticles' surfaces, a lower number of molecules per functionalised particle is then obtained. Additionally, continuous growth of trehalose functionalised particles is supported by the already reported capacity of adsorbed trehalose to easily polymerize *in situ* with other in-solvent trehalose molecules and thus form longer polymeric chains [144].

The procedure above was also tried in a 50 % (v/v) acetone-water solution, in accordance to the protocol herein followed, but larger particles of 1100 nm were obtained for 1:1 ratio, along with higher values of PdI between 0.5-0.6.

From the results above, we can affirm that the use of sucrose as surface functionalizing and stabilizing agent is the best choice when seeking the improvement of SBA nanosystems solubility in water, for it promotes the diminishing of particles average size by interfering with aggregation phenomena and increasing nanoparticles stability in aqueous media. Also confirmed by SEM micrographs of the resulting nanoparticles (Figure 3.5). Additionally, this was the only sugar capable of maintaining its

behaviour constant for no significant interference on particles original size was observed with the increase of added sugar. A ratio of 2:1 is advised since higher values of zeta potential and PdI were observed. Any sugar excesses are easily washed with a one-time water wash.

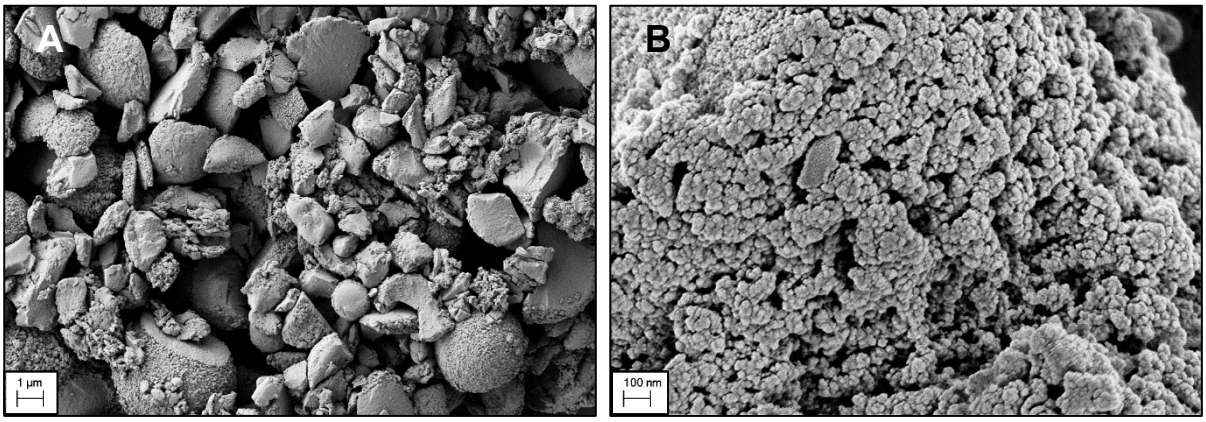

Figure 3.5 | SEM micrographs of sucrose functionalised SBA-16 nanoparticles (2:1 ratio) with clear (A) disruption of aggregates and (B) occurrence of vesicles between nanoparticles.

3.5 Concluding Remarks

Briefly, the development and selection of mesoporous silica nanoparticles for later interaction with chemically or biochemically active molecules based itself on the analysis of structural and interactive variables intrinsic to SBA-16 systems.

After the development of distinct synthetic pathways, assets like relative in-solution stability, acceptable partible sizes and reproducibility have pointed out Method 2 as the best synthetic methodology for the production of SBA-16 mesoporous materials.

Pore modulation was attained with the use of the swelling agent TMB aiming for the production of 12.7 nm pores. Unfortunately, further analysis confirmed the presence of smaller pores than those reported by Katiyar *et al*, for all M2 samples. The same result was obtained for other variables such as S_{BET} and porous volume, and might have an impact on future experiments. All results are briefed in Table 3.8.

Table 3.8 | Summary of all collected data from N_2 physio absorption assays, for T1, T2 and T3 SBA-16 samples. Reported data from literature is also display as a comparison element.

	TMB : F127 (g/g)	**S_{BET} (m^2/g)**	**Porous volume (cm^3/g)**	**BJH pore diameter (Å)**
S-4 *	0	756	1.18	64.4
S-5 *	0.5	768	1.63	127.4
T1	0	731	0.4	30.5
T2	0	343	0.20	39.2
T3	0.5	534	0.57	49.6

* Data from literature for SBA-15 nanoparticles, as reported by Katiyar *et al* [16]

Future improvements on these properties might lean on a more extensive template removal technique, or even the use of a calcination-extraction conjugated methodology as proposed by Grudzien *et al* [109].

Additionally, in order to overcome existing instabilities, and thus formation of aggregates, surface functionalisation has proved itself a good tool. The creation of a sugar-based surface had produced more stable and less aggregated colloidal particles, with sucrose showing the right performance at keeping the original particles size while increasing (towards more negative values) their zeta potential. A summary of the procedure and its results is present at Figure 3.6.

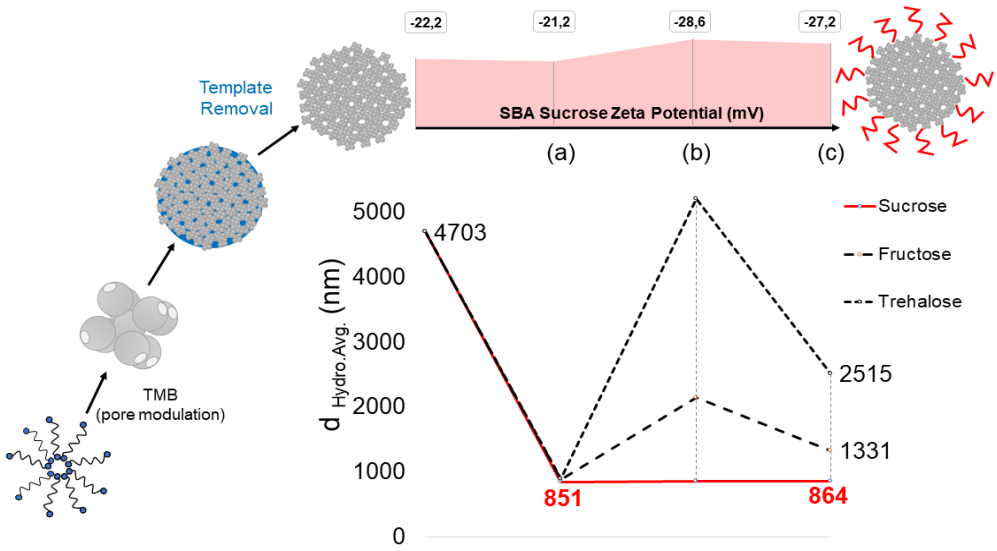

Figure 3.6 | Brief schematics of the whole synthesis procedure, from particles formation to its surface functionalization, with (a) 1:1, (b) 2:1 and (c) 3:1 sugar : SBA ratios.

4

Synthesis and characterisation of NHS-Rhodamine-based derivative. Encapsulation studies of luminescent chromophores into mesoporous nanoparticles

Following the synthesis of solid supports for protein adsorption, the development of luminescent rhodamine B-based probes (RhNHS and RhISO) with affinity towards biomolecules for later doping of all silica materials is herein discussed. Structure and purity were important analysed characteristics, with the aid of ^{1}H and ^{13}C NMR techniques.

Loading and releasing behaviours were also evaluated, varying parameters as pH, loading media and pore size. The encapsulation of a second porphyrin-based chromophore (L5) is also discussed in this section.

Keywords: Rhodamine B, NHS, porphyrin, doping, release profile

4.1 Synthesis

With a proper couple of SBA-16 silica mesoporous nanoparticles to work as solid supports for the extraction of proteins, the second phase of this work fell upon the development of a tailor-made chromophore for the interaction with proteins.

For this purpose, and taking in consideration that further studies will develop in aqueous media, rhodamine B dye was chosen as a good candidate. This chromophore is known for its relative stability in water and its large spectra of known applications in the tracing of rate and direction of flow and transport of biomolecules [145, 146]. Besides, this chromophore is also known for its characteristic pink colour and intense orange fluorescence, when under UV light, with fluorescence quantum yields as high as that of fluorescein and other common labelling dyes [126, 145]

However, the enhancement of rhodamine B (RhB) chromophore's capacity of labelling and binding proteins relies on the introduction succinimidyl esters within its native structure carboxyl group(s) [126]. Succinimidyl esters are proven to be the best reagents for amine modifications since resulting amide

bonds are identical to, and as stable as that of natural peptide bonds [127, 147]. Thus, justifying the selection of a N-hydroxysuccinimide (NHS)-modified rhodamine B chromophore (**RhNHS**) to work as a labelling and binding probe for the extraction of proteins within this work.

The synthetic mechanism for the above-mentioned compound followed a Steglish esterification (Figure 4.1), as reported by Xu *et al* [148], and is thoroughly detailed in Chapter 7. It is worth mentioning, that along with RhNHS synthesis Dicyclourea (DCU) is also formed as a by-product of the reaction, due to the use of Dicyclohexylcarbodiimide (DCC) catalyst.

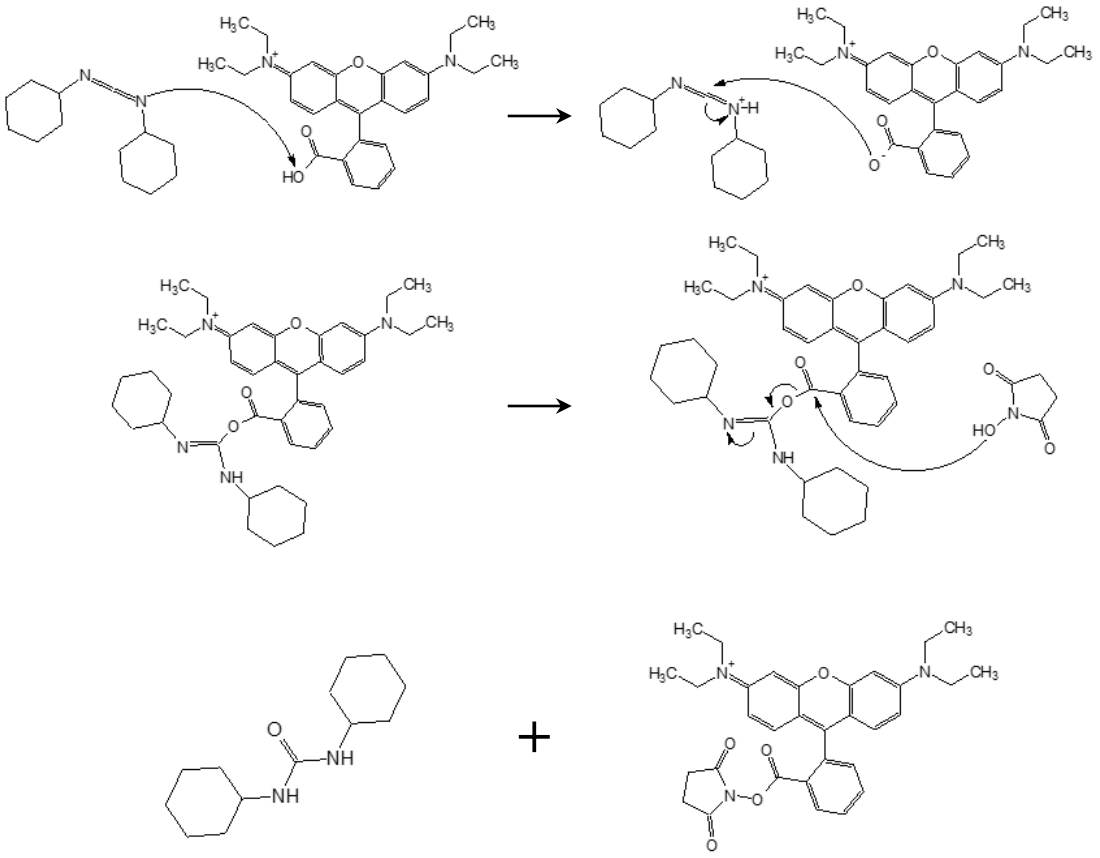

Figure 4.1 | Step-by-step reaction pathway of a DCC catalysed Steglish esterification for the synthesis of RhNHS (right), with the co-production of DCU (left).

In order to obtain a maximum of conversion and avoid possible side competing reactions, not only dichloromethane (DCM) was used as reaction solvent, but the initial mixture was let to react for a long period, only stopping after 6 full days (followed by thin layer chromatography). By the end of the reaction and a dark-purple coloured dry powder, with reddish-orange fluorescence under a 365 nm UV-light, was obtained with a yield of 85%.

The RhNHS compound was characterised by ^{1}H and ^{13}C NMR (see Figure 4.2). As in is seen in the figure below, the ^{1}H NMR spectra showed a clear characteristic signal of the NHS group at 2.7 ppm. Additionally, the inexistence of a peak corresponding to an -OH functional group, around 11 ppm, corroborates the successful incorporation of the NHS group.

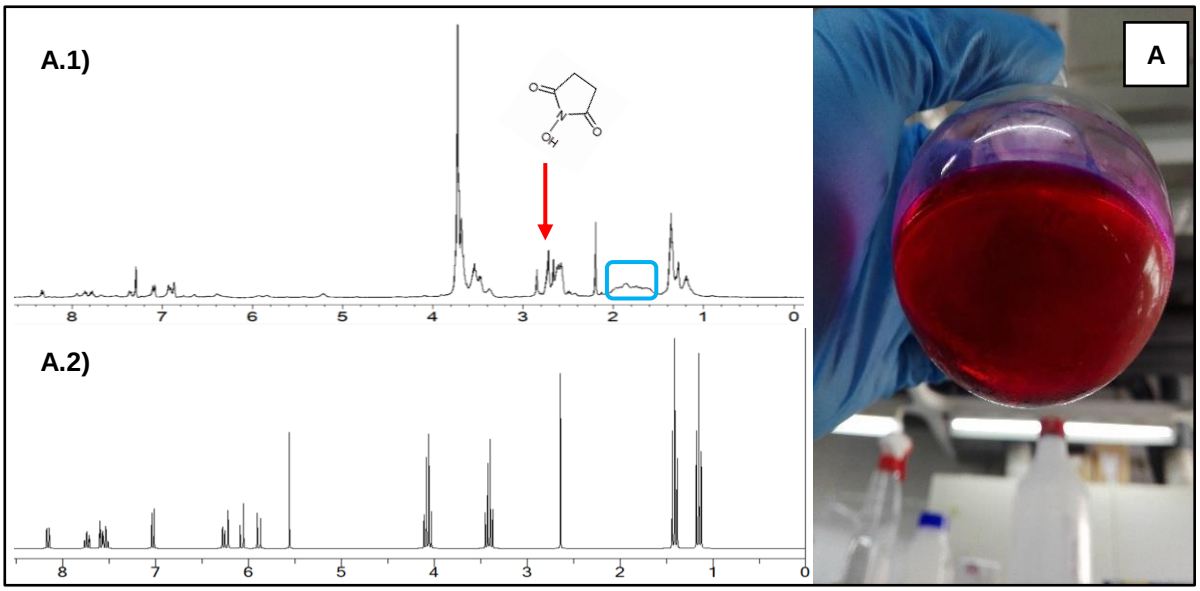

Figure 4.2 | A) Post DCU precipitation RhNHS product solution (in acetone) with its experimental ^{1}H NMR spectrum **(A.1)**, in $CDCl_3$, *vs* RhNHS theoretical spectrum **(A.2)**. 2.7 ppm NHS peak is highlighted, in red, and DCU interfering peaks, in blue.

In addition, through the obtained ^{13}C spectra, carbons from NHS group were also visible at 36.0 and 36.6 ppm, again confirming the existence of such group within the molecule.

The obtained results by ^{1}H NMR spectra are then in agreement with those reported by Wei *et al* [126]. Furthermore, as noticed in ^{1}H NMR spectra, the washing steps with cooled acetone are crucial to decrease the number of interfering peaks between 0-2 ppm, usually associated to the side product of the Steglish esterification, the DCU (pre-washing spectra in Figure AIII.2, **Annex III**).

Finally, it should be noticed that the manipulation of RhNHS during and post its synthesis was performed under hydrophobic conditions to avoid competing side reactions, for it is known from literature that NHS esters hydrolyse within hours or minutes, depending on water-content and pH of the reaction solution (e.g. NHS esters have a half-life of 4-5 hours, 1 hour or only 10 minutes for pH of 7.0, 8.0 and 8.6, respectively).

4.2 Loading of Rhodamine B-Based Chromophores

The loading, or adsorption, of chromophores onto SBA-16 M2 nanoparticles was employed over all T1, T2 and T3 synthesised samples, following the methodology proposed by Wang *et al* [149] for the physical adsorption of biomolecules. Besides, the doping of second rhodamine B-base chromophore, Rhodamine B Isothiocyanate (**RhISO**), was also considered and tested as a commercial competing agent against RhNHS (Figure 4.3). The experimental procedure can be found, detailed, in **7.3.4**.

With the above statement in mind that all chromophores manipulations should be performed in organic media, a first loading test with 1 mg of each RhNHS and RhISO onto two 20 mg SBA-16 M2 T1 batches was made in Dimethyl Sulfoxide (DMSO).

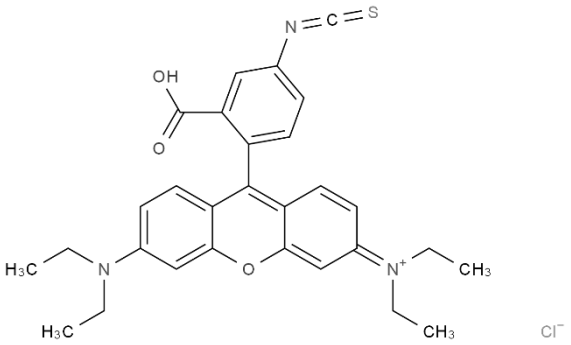

Figure 4.3 | Rhodamine B Isothiocyanate structure.

As expected, due to the high density of DMSO no pellet formation after centrifugation was observed and the addition of methanol (MEOH), an assisting agent on pellet formation, was made on a ratio of 1:1 (v/v) to the initial blend. While in one hand the improvement allowed for the so sought pellet formation, on the other a slight decolouration of the latter was also observed. This led to the elaboration of the hypothesis that, due to the relatively high solubility of RhB chromophores in MeOH (10 mg/mL), consecutive washes with this solvent, or MeOH composing solvents, might promote a total desorption of chromophores from SBA-16 pores. Luckily, this theory was proven after 3 consecutive washes with MeOH, as the resulting pellets showed a white appearance again (Figure 4.4).

We can then conclude that DMSO and MeOH are not useful solvents when doping RhB-based chromophores onto SBA-16 mesoporous particles and that the latter might pose an interesting medium for the reusability of the whole device, a theme to be discussed further.

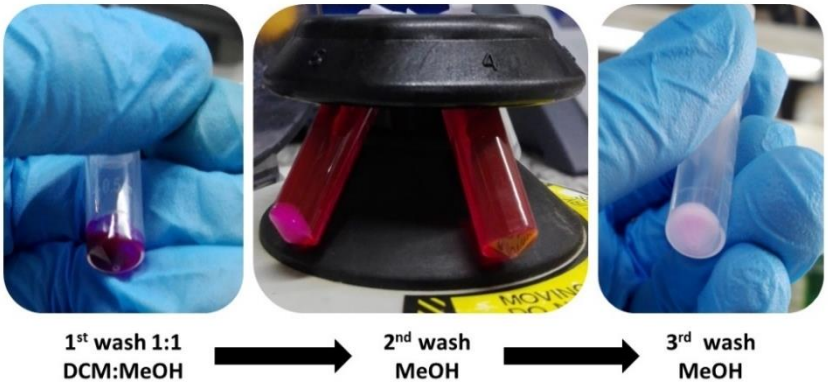

Figure 4.4 | Progression on pellet recovery with consecutive washes with MetOH, or MeOH containing solvents

Therefore, in order to surpass the present drawback, the loading procedure was again tested with Chloroform ($CHCl_3$) as solvent. After several washes in the same solvent, formed pellets kept a dark-purple appearance typical of RhB-based chromophores, confirming the success of the selected loading technique. It is worth noticing that the pellet must be washed as many times as possible till a clear supernatant is obtained. Only then are we able to prove that, after been physical adsorbed, both RhNHS and RhISO prefer silica pore walls over the dispersing medium ($CHCl_3$) and are thus thermodynamically stable.

The effect of doping over SBA-16 nanoparticles stability in solution was also evaluated and its zeta potential measured. Due to measurements material's restrictions and to have a feasible comparison with previous results, the once dry pellets had to be resuspended in deionised H_2O before any measurements. Acquired zeta potentials are as displayed in Table 4.1.

Table 4.1 | Zeta potential of doped SBA-16 M2 T1 samples, with RhISO and RhNHS, in triplicates.

Samples' ID	Zeta Potencial (mV)
SBA-16 M2 RhISO	-37.4 ± 1.5
SBA 16 M2 RhNHS	- 19.8 ± 0.7

A quick comparison with the values of zeta potential obtained for empty pores SBA-16 M2 T1 samples (Table 3.3) lead us to conclude that the internalisation of RhISO has a more stabilizing effect over surface net charge (decreasing from ~ -25 to ~ -37 mV), than that of RhNHS. In fact, the latter produces a slight destabilizing effect, rising its surface potential in approximately 5 mV, placing the resulting nanosystems at the borderline (± 20 mV) for relatively well-dispersed silica-based colloids for biological applications [129]. Unfortunately, particles aggregation might pose a problematic reality.

Nonetheless, based on literature it is known that the templating of silica mesopores results in a rise of surface zeta potential (towards positive values), a consequence on the reduction of free hydroxyl groups along pore walls [10, 150]. Thus, it is safe to admit that the destabilizing effect of RhNHS internalisation is the best confirmation of its successful loading within silica pores. Regarding RhISO, the decrease towards approximately -40 mV might result from a conjugation between pore walls and particle surface functionalisation, as the latter usually results in higher dispersion stability [151]. The presence of isothiocyanate (NCS) groups in RhISO may work as a linking / anchoring agent towards -OH groups at particles' surface, thus creating a preferential stable bonding of RhISO molecules to silica surface.

A spectroscopically analysis on all RhISO and RhNHS supernatants, revealed, after absorbance readings (in triplicates, against a blank of each chromophore in $CHCl_3$), average loading capacities of SBA-16 M2 T1 samples of 44 mg/g and 48 mg/g towards RhNHS and RhISO, respectively.

Therefore, with a now well-established method, the loading of both RhNHS and RhISO compounds onto SBA-16 M2 T2 and T3 samples (with 4 nm and 5 nm of pore diameter, respectively) was sought.

All samples were thoroughly washed with $CHCl_3$ and its supernatants quantified. The in-solution amount of RhNHS, or RhISO, was determined through supernatants absorbance and later application of the Lambert-Beer law. All UV-visible measurements were run against a RhNHS (or RhISO) blank, in the same solvent, from which a linear relationship between absorbance (ABS < 1) and concentration was

verified for a fixed light pathway (1 mm) and constant ε (ε_{RhNHS} = 417,790 $cm^{-1}M^{-1}$ and ε_{RhISO} = 938,020 $cm^{-1}M^{-1}$). Both calibration curves can be found in Figure AIII.3 (**Annex IV**)

Regarding the remaining loaded RhNHS (or RhISO) quantities, these were calculated by a simple mass balance and given by means of loading yields (% L) and loading capacities (LC), in mg_{RhB} / $g_{SBA\text{-}16}$. (Equation 7 and Equation 6).

$$\%\, L = \frac{Rh_i - Rh_d}{Rh_i} \cdot 100$$

Equation 7 | Loading yield (%) formula.

$$LC = \frac{Rh_i - Rh_d}{m_{SBA-16}}$$

Equation 6 | Loading capacity (mg/g) formula.

Where, Rh_i is the initial mass, in milligrams, of RhB-based chromophore, Rh_d the loaded mass of RhB-based chromophore and $m_{SBA\text{-}16}$ the mass, in grams, of SBA-16 M2 sample (each batch with approx. 20 mg). Obtained results are summarised in Table 4.2.

Table 4.2 | Loading yield (% L) and capacity (LC, mg/g) obtained for RhNHS and RhISO doping trials in SBA-16 M2 T2 and T3 samples. Correspondent average (avg.) and standard deviation (*σ*) represented along the respective test. Chromophore and SBA-16 used masses are detailed, between brackets (in mg), bellow its respective LC.

	T2		**T3**	
	% L	**LC (mg/g)**	**% L**	**LC (mg/g)**
RhISO	92	48.72 (1.1mg/20.7mg)	96	65.93 (1.5mg/21.8mg)
	86	40.06 (1.0mg/21.5mg)	91	42.65 (1.0mg/21.4mg)
	83	47.65 (1.2mg/20.8mg)	95	66.66 (1.5mg/21.4mg)
Avg.	87	45.48	94	58.41
σ	4	3.85	2	11.15
RhNHS	74	37.1 (1.0mg/20.0mg)	72	44.78 (1.3mg/21.0mg)
	81	51.86 (1.3mg/20.2mg)	80	42.03 (1.1mg/21.0mg)
	63	29.31 (1.0mg/21.4mg)	67	36.79 (1.1mg/20.1mg)
Avg.	73	39.42	73	41.20
σ	7	9.35	5	3.31

From the collected results, it is noticeable that loading capacities are intrinsically dependent on the type of chromophore used during the loading step, as RhISO was able to dope both SBA-16 T2 and T3 pores with approximately more 10 mg/g than RhNHS. This could be explained by the family of terminal functional substituents present on each of the chromophores, with the NCS group from RhISO favouring stronger bonds with particles' surface and pore walls hydroxyl groups [151]. This contrasts with the simple physical attraction between silica -OH groups and RhNHS molecules that grants a more fragile interaction and equilibrium. Thus, the protection promoted by SBA-16 silica cage-like pores to adsorbed RhNHS molecules is preferable, while surface adsorbed molecules are more exposed to possible attacks from the surrounding medium and are then instable. These results corroborate with the previously reached conclusions on zeta potentials and chromophores interactions with silica particles.

On the other hand, no dependency on pores' diameter is visible, as the average loading capacity for both chromophores seem to reach a single plateau for both pore sizes. In detail, RhISO saturation adsorption point is reached at a value around 50 mg/g, whilst for RhNHS it is reached at approximately 40 mg/g. This lead us to conclude that future protein loading trials will not depend on the loaded amount of chromophores, but rather on the type of chromophore, pore size and accessibility to adsorbed chromophore (for a fixed amount of nanoparticles).

Additionally, it is worth noticing that the results obtained for the loading of RhNHS in T2 samples and RhISO in T3 samples comprise consider wide standard deviations and thus small accuracy (both relative standard deviations – RSD – above 10%).

4.3 Release Trials

In a way to predict the behaviour of the system when proceeding to proteins adsorption in aqueous media, the effect of pH over RhNHS release was also evaluated. For this matter 1mg RhNHS T1 doped samples were resuspended in three buffer solutions, with pH ranging from 4.5 to 8.5 (PBS pH 4.5, PBS pH 7.4 and Tris Base pH 8.5, respectively). 30 minutes and 2h points were collected in order to trace a time dependent release profile.

For these tests, the 44 mg/g average loading capacity of RhNHS in SBA-16 M2 T1 samples was taken as the maximum available RhNHS quantity, per gram of silica nanoparticles, and all absorbances read against RhNHS blanks in each buffer solution. Concentrations and masses of RhNHS were obtained through the Lambert-Beer law and the above-mentioned mass balances. Obtained profiles are as displayed in Figure 4.5.

From Figure 4.5 we can clearly conclude that the release of RhNHS is strongly pH dependent, with a % of release higher for acidic conditions than that observed for basic media; with a pH 4.5 maximum of 22 mg/g (~ 50%) against a clearly lower maximum of 4.4 mg/g (10%) for pH 8.5. A similar behaviour was reported for other rhodamine B doped systems [152, 153] and may be a result of the already reported increase of rhodamine B chromophores solubility in aqueous media at low pH [154]. Nonetheless, electrostatic interactions may also be at work, for it has also been reported in other

encapsulation studies of fluorophores onto SBA-16 pores, that the increase of repulsions between negatively charge groups in silica pores and in fluorophores was associated with a decrease in pH [38]. Moderate release at pH 7.4 is achieved, as only 20 % of the loaded RhNHS is released; corresponding

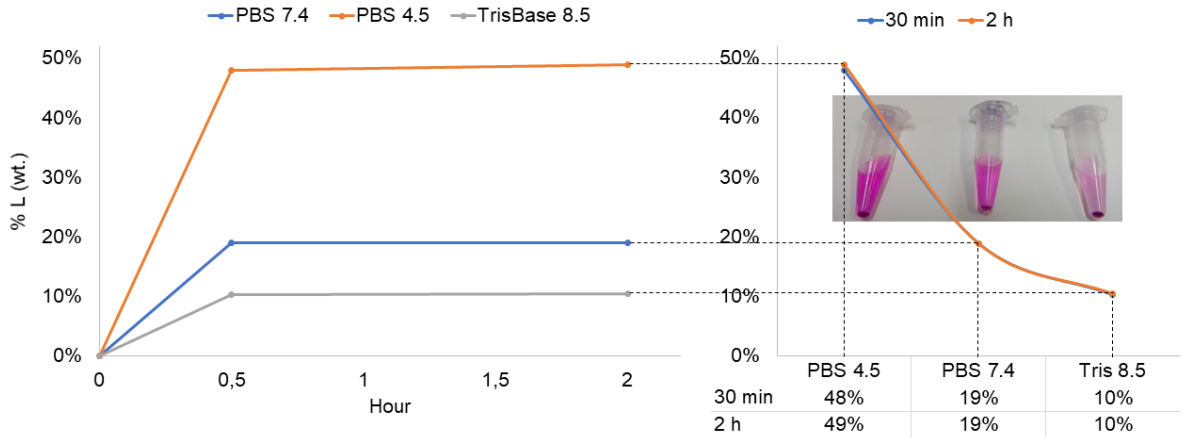

Figure 4.5 | Time dependent **(left)** and pH dependent **(right)** progression of % L RhNHS release profiles in different pH buffers**.** Trials run on 4.5 PBS, 4.7 PBS and Tris base 8.5 buffers.

to maximum of 8.8 mg/g of released RhNHS. This leaves us with a considering amount of encapsulated RhNHS (35.2 mg/g, 60 % of initial RhNHS), available for later interaction with proteins or other biomolecules.

In addition, it is easily perceived that for all pHs a release plateau (saturation point) is reached earlier than the collected 2h and 30 min points, for no significant change in the release percentage is visible after 30 minutes of incubation. This last piece of data was of utter importance to us, since it indicated that for future experiments with biomolecules any extra amount of RhNHS in surrounding media, after 30 min of incubation, results solely from a somewhat interaction between proteins and the designed device. However, a more detailed assay would need the collection of several points below the 30 min. mark.

It is also known from the literature that the hydrolysis of NHS esters is strongly pH dependent, having a half-life of 4 to 5 hours at pH 7.0 (4 ºC) and of 10 minutes at pH 8.5 (0 ºC) [127], the last highly desirable for efficient amide bonds formation. To sum up, NHS-ester crosslinking reactions are most commonly performed in phosphate, carbonate-bicarbonate, HEPES or borate buffers at pH 7.2 to 8.5 for 0.5 to 4 hours at room temperature or 4°C. However, the use of Tris base buffer must be avoided when manoeuvring NHS ester, for the primary amine of Tris base is known to compete with proteins for the amide bond formation [127]. Thus, the search for a compromise between a moderate RhNHS release, similar conditions to that of biological fluids and a relatively effective hydrolysis of NHS groups, sets pH 7.4 media as the holders of the best conditions for future protein extractions experiments.

4.4 Loading of L5 Porphyrin

Extending the system's application towards a more environmental area, with the incorporation of the L5 porphyrin onto the already synthesised SBA-16 M2 silica particles we were able to design a cheap colorimetric device capable of sensing and extracting metal-ions from aqueous media.

The incorporation of this water-soluble porphyrin (L5) followed the already studied loading in $CHCl_3$, and was performed on 20 mg batches of SBA-16 M2 T3 samples. Its preference for aqueous media was instantly observed as no solvation existed when L5 was mixed with the solvent. Additionally, as expected when in presence of silica nanoparticles, a total precipitation and encapsulation of L5 over and onto SBA-16 surface and pores was observed. This was again confirmed after no traces of L5 were found on subsequent $CHCl_3$ washing supernatants (instant acquirement of clear supernatants).

Under the impression of impossible 100% (wt.) loading yields, washes with deionised H_2O lead to the removal of most precipitated porphyrin from the 20 mg batches. Consequent quantification by absorbance of the resulting supernatants, at 505 nm with a known ε =13247,5 ($M^{-1}.cm^{-1}$) and light pathway of 1 cm, allowed for the determination of the in-solution L5 concentration. Loading yields (% L) and loading capacities (LC) were calculated by the above-mentioned mass balance (Equation 7 and Equation 6) and are detailed in the table below (Table 4.3).

Table 4.3 | Obtained loading yields (% L) and capacities (LC, mg/g), for all L5 doping trials in SBA-16 M2 T3 samples. Correspondent average (avg.) and standard deviation (σ) represented along the respective test. Used SBA-16 and L5 masses are also detailed.

m_{L5} (mg)	m_{SBA} (mg)	% L	LC (mg_{L5}/g_{SBA-16})
1.0	20.3	17%	8.44
	20.1	22%	10.80
	20.0	31%	15.36
	20.2	23%	11.39
	20.2	27%	13.29
Avg.		24%	11.86
σ		5%	2.34

It is worth noticing that these measurements were performed at the maximum peak of the first left Q-band (505 nm) of the absorbance spectrum of L5 porphyrin, for this type of band is known to, when in the visible region, suffer intensity of colour shifts according to induced chemical modifications over free-base porphyrins, such as external or central coordination of metal ionic species [155].

As is noticeable in the table above, a 24 % loading yield, corresponding to a 11.86 mg/g loading capacity, was the maximum fraction of the initially used L5 (1 mg) that was kept, physically adsorbed, inside SBA-16 M2 T3 pores. Conversely, the remainder 76 % corresponded to a precipitating excess that was washed away with deionised water. In a quick evaluation of the procedure one would call the methodology inefficient. However, the 24 % loading yield proved, later, to be the right amount of loaded

L5 porphyrin to avoid optical saturation and masking effects when detecting and extraction ionic species from aqueous samples.

4.5 Concluding Remarks

Succinctly, the development of chromophore with relative affinity towards protein interaction was achieved with the synthesis of a rhodamine B-based NHS ester. The NHS ester is the best candidate since it is known to, either in physiological pH 7.4 or under basic conditions (pH 8.5), form stable amide bonds with proteins, with relative speed. Additionally, the near-pure chromophore (DCU-free RhNHS) was confirmed to be successfully adsorbed onto SBA-16 silica nanoparticles' pores with stability enough to allow for the encapsulation of approximately 40 mg/g, a capacity close to the 50 mg/g obtained for a supposedly more strongly adsorbed chromophore (RhISO).

Moreover, not only it was concluded that the sorption of these chromophore species was independent of pore width, with similar loading capacities for T2 (d=4 nm) and T3 (d=5 nm) samples, but also that a plateau of released chromophore was reached in less than 30 min. However, it was also observed that the maximum of released RhNHS is pH dependent, with a release near to 50% (wt.) of loaded RhNHS at pH 4.5. A moderate release in pH 7.4, of about 20% (wt.), was also visible and it is what we think to be the best compromise between an acceptable release, by promoting, in future assays, an equilibrium between the consequent emptying of some pores and the creation of an opportunity for proteins to migrate through the porous net towards the still adsorbed RhNHS molecules.

Again, these conclusions are of utter importance to us, since it indicated that for future experiments with biomolecules any extra amounts of RhNHS in surrounding media, after 30 min of incubation, result solely from the interaction between proteins and the designed device (type of chromophore, pore diameter or accessibility to chromophore), for a fixed pH.

Nonetheless, a recovery pathway for RhNHS doped silicas was also discovered, as it was found that MeOH is an excellent solvent for the near-to-total desorption of RhNHS from SBA-16 pores.

Lastly, the loading of the L5 porphyrin was also successful, after washing the system with deionised water and ensuring that the loaded amount corresponded to real adsorbed molecules of L5. A relatively low 24 % loading yield (approx. 12 mg/g) was optimal for future studies as it avoided optical saturation and masking effects when detecting and extraction ionic species from aqueous contaminated samples.

5

Application of dye-doped mesoporous nanoparticles for extraction of proteins.

With a now tailor-made system, its capacity to extract proteins, selectivity and behaviour were validated against a set of seven model proteins, in PBS buffer solutions. Chromophore (RhNHS and RhISO) and pore size (T2 and T3 samples) effect over the above-mentioned variables was also verified, for incubation times of 30 min and 2h. Protein quantification was achieved by Bradford assay and protein doped-particles' stability described by their zeta potentials. Protein-particle interaction was also confirmed by SDS PAGE electrophoresis.

Keywords: protein, extraction, SBA-16, RhNHS, RhISO, T2 and T3

5.1 Proteins Extraction Quantification

Focusing on the main objective of the present work and moving towards a more applied approach, with a now fully tailor-made system for the extraction of biomolecules and the selection of the best conditions for its trials, tests in biological media were performed and the system's extraction capacity evaluated.

As proof-of-concept, the new SBA-16 nanoparticles, doped with RhNHS and RhISO, were used as novel platforms for the extraction of proteins in real situations. In that way, their ability to load and extract proteins from solutions was achieved by the use of model proteins with different and well-known molecular weights, sizes, shapes and pI values. However before moving to complex biological media such as urine, serum or saliva, pure protein samples were used.

Table 5.1 summarizes all tested proteins and their respective data.

In this work this set was composed of seven selected proteins, being them bovine serum albumin (BSA), lysozyme (LYS), cytochrome c (Cyt C), myoglobin (Myo), haemoglobin (Hb), carbonic anhydrase (CA) and ovalbumin (OVA).

Table 5.1 | Chosen set of proteins for further extraction trials and their correspondent properties.

Protein	pI	MW (kDa)	Hyd. Size (nm)	Dimensions (Å)	Reference
BSA	4.9	66.5	7.3	40 × 40 × 140	[31]
LYS	11.35	14.3	3.2	30 × 30 × 45	[31]
Cyt C	10-10.5	12.0	2.7	25 × 25 × 37	[156]
Myo	6.8	16.9	3.7	21 × 35 × 44	[157]
Hb	6.8	64.5	4.2	60 × 50 × 50	[158]
CA	5.9	29	3.7	40 × 42 × 45	[159]
OVA	4.9	45.0	6.3	70 × 45 × 50	[160]

The influence of pore size over the above mention loading capacities was achieved by testing both small and large pore samples (T2 and T3). All results were compared with SBA-16 blanks (with non-functionalised pores) for both pore sizes.

Proteins were incubated with RhNHS@SBA and RhISO@SBA nanoparticles, in PBS 7.4, on a weight ratio of 1:1, 1:2, 1:4 (protein:Nanoparticle), for incubation times of 30 and 2 hours. Encapsulation efficiency (% L) and loading capacity (mg/g) were determined according to the proceedures detailed in **7.3.8,** and the obtained results, for 30 min samples, gathered in Figure 5.1.

Concerning Figure 5.1, a common tendency was observed. An increase in the amount of protein contributes positively to the amount of adsorbed protein, ranging from ca. 10% to ca. 30-46% in A, from 10% to 30-60% in B and from 15% to 30-50% in C. The same behaviour was noticed for the loading capacity (mg/g). Additionally, for a fixed ratio (1:1), the introduction of a chromophore RhNHS or RhISO favours in a general way the loading of proteins. From all evaluated proteins, there was this common tendency of OVA protein to rank the highest values of % L and loading capacity (mg/g), of about 44-52% and 464-519 mg/g, respectively. However, when nanoparticles were doped with RhNHS and RhISO chromophores there was a clear increase on the loaded amount of BSA, especially for RhNHS (T2: 8%; T2 NHS: 36%; T2 ISO: 29%).

This fact could be attributed to the percentage of NH_2 residues within the protein, since NH_2 groups are known to favour the linkage with NHS groups. As a matter of fact, both proteins BSA and OVA have quite similar percentages of NH_2 residues (BSA: 856 amines in 607 amino acids; OVA: 514 amines in 386 residues) [161], which are in agreement to the abovementioned (Table AIV.1, **Annex IV**). Weather this factor is of utter importance, protein's size, shape and volume also play a significant role. The fact that even without chromophore ovalbumin show high affinity to nanoparticles is proof of that, with OVA having smaller size, volume and a more sphere-like shape than BSA.

Regarding T3 nanoparticles (with larger pores), in Figure 5.2 the same positive behaviour was observed with a general increase of loaded proteins, as well as a preferable affinity of these nanoparticles for ovalbumin (% L 44-50%; loading capacity (mg/g): 440-497, for ratio 1:1).

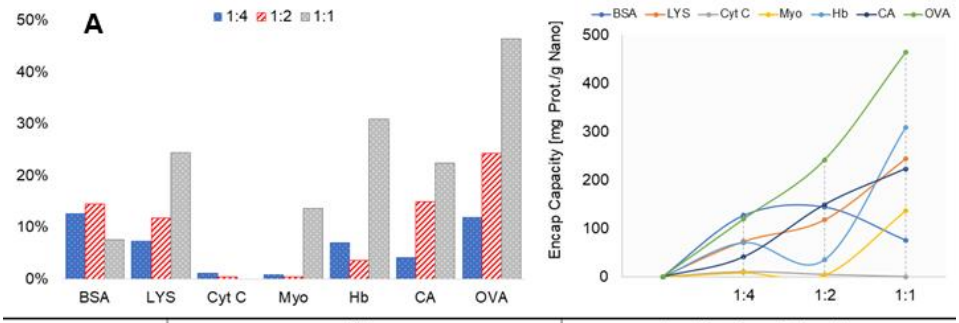

Protein	% L			Loading Capacity (mg/g)		
	1:4	1:2	1:1	1:4	1:2	1:1
BSA	13%	14%	8%	127	144	76
LYS	7%	12%	24%	73	118	244
Cyt C	1%	0%	0%	11	5	0
Myo	1%	0%	14%	9	4	136
Hb	7%	4%	31%	71	36	309
CA	4%	15%	22%	41	150	224
OVA	12%	24%	46%	119	242	464

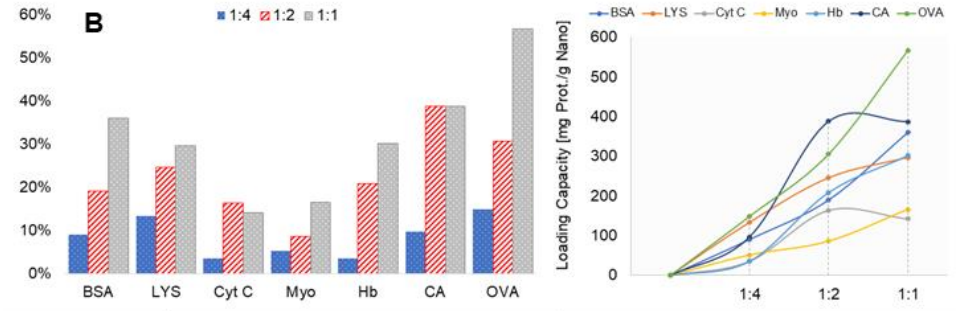

Protein	% L			Loading Capacity (mg/g)		
	1:4	1:2	1:1	1:4	1:2	1:1
BSA	9%	19%	36%	91	191	361
LYS	13%	25%	30%	134	246	297
Cyt C	4%	16%	14%	36	164	142
Myo	5%	9%	17%	52	87	166
Hb	4%	21%	30%	36	209	302
CA	10%	39%	39%	97	388	388
OVA	15%	31%	57%	149	306	567

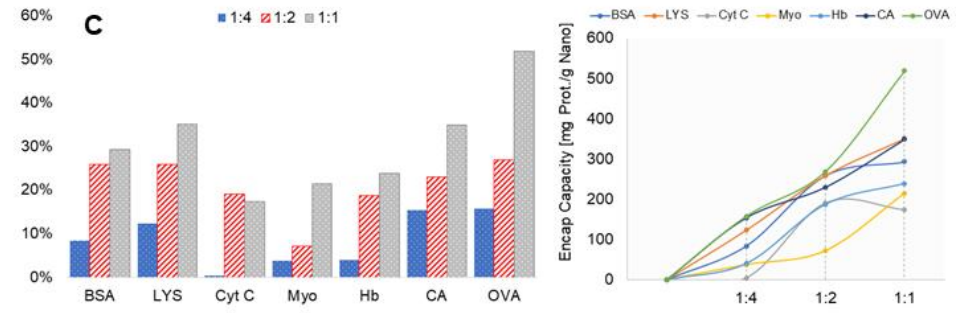

Protein	% L			Loading Capacity (mg/g)		
	1:4	1:2	1:1	1:4	1:2	1:1
BSA	8%	26%	29%	84	259	293
LYS	12%	26%	35%	123	258	350
Cyt C	0%	19%	17%	4	191	174
Myo	4%	7%	21%	37	72	215
Hb	4%	19%	24%	40	187	239
CA	15%	23%	35%	154	230	349
OVA	16%	27%	52%	157	269	519

Figure 5.1 | % L (left) and loading capacities (right) of all 30 min incubations on (A) SBA-16 T2 blank, (B) RhNHS@SBA T2 and (C) RhISO@SBA T2 samples, for Protein : Particle wt. ratios of 1:4, 1:2 and 1:1; after Bradford assay quantification, in PBS 7.4.

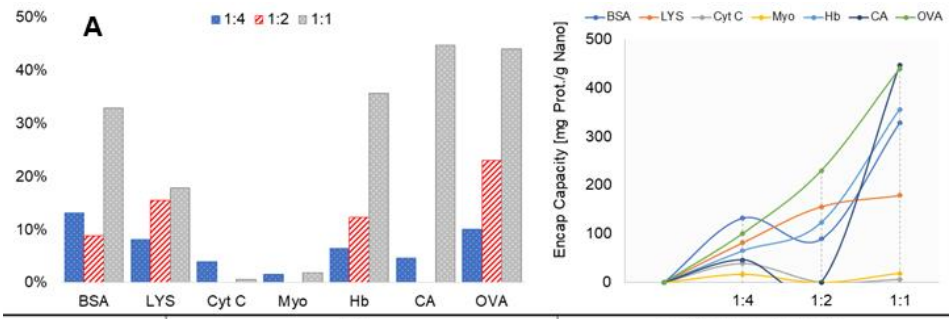

Protein	% L			Loading Capacity (mg/g)		
	1:4	1:2	1:1	1:4	1:2	1:1
BSA	13%	9%	33%	132	89	328
LYS	8%	16%	18%	81	156	179
Cyt C	4%	0%	1%	39	0	6
Myo	2%	0%	2%	16	0	18
Hb	6%	12%	36%	65	123	357
CA	5%	0%	45%	46	0	447
OVA	10%	23%	44%	100	230	440

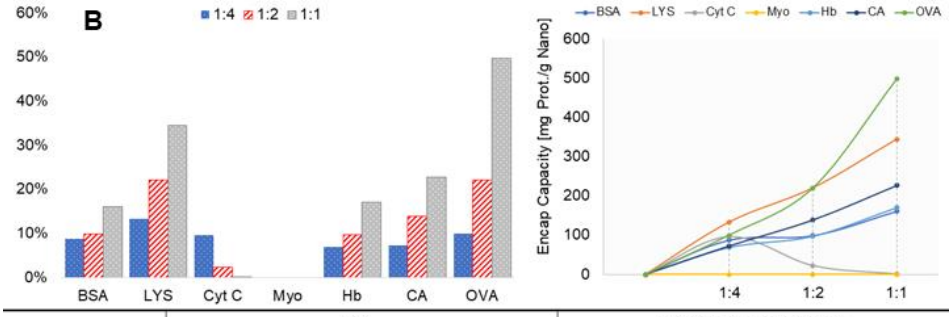

Protein	% L			Loading Capacity (mg/g)		
	1:4	1:2	1:1	1:4	1:2	1:1
BSA	9%	10%	16%	87	99	161
LYS	13%	22%	34%	133	220	344
Cyt C	10%	2%	0%	97	23	1
Myo	0%	0%	0%	0	0	0
Hb	7%	10%	17%	68	97	170
CA	7%	14%	23%	73	139	227
OVA	10%	22%	50%	100	220	497

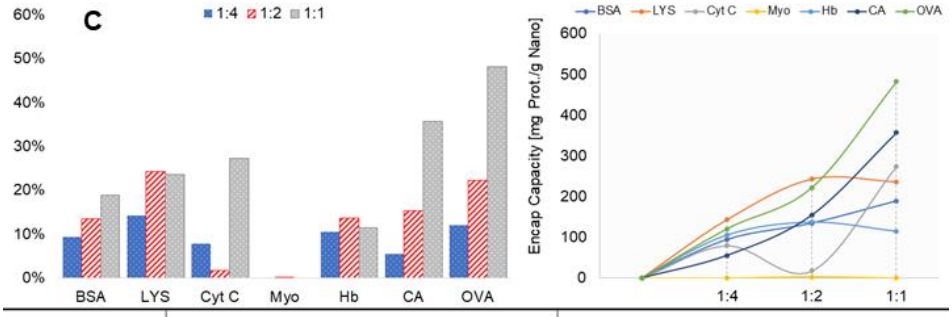

Protein	% L			Loading Capacity (mg/g)		
	1:4	1:2	1:1	1:4	1:2	1:1
BSA	9%	13%	19%	94	135	190
LYS	14%	24%	24%	143	243	236
Cyt C	8%	2%	27%	80	17	274
Myo	0%	0%	0%	0	2	0
Hb	11%	14%	11%	106	137	115
CA	6%	15%	36%	55	154	357
OVA	12%	22%	48%	121	222	482

Figure 5.2 | % L (left) and loading capacities (right) of all 30 min incubations on (A) SBA-16 T2 blank, (B) RhNHS@SBA T3 and (C) RhISO@SBA T3 samples, for Protein : Particle wt. ratios of 1:4, 1:2 and 1:1; after Bradford assay quantification, in PBS 7.4.

Contrary of what was observed in T2 nanoparticles, the introduction of chromophores (RhNHS or RhISO) did not contributed to an increase of loaded proteins. On the other hand, all nanosystems seemed to be more selective, with lower affinities towards Myo and Cyt C, independently from the type of nanoparticles system used (T3, RhNHS@SBA T3, RhISO@SBA T3).

Incubation time of 2 hours (see Figure AIV.1 and Figure AIV.2, **Annex IV**) did not produce significant improvements on the nanoparticles' loading capacity, where in some cases (i.e. Ovalbumin) negative contributions led to a small decrease in the amount of adsorbed proteins.

5.2 Proteins Influence over SBA systems stability

To understand the impact that the adsorption of proteins had over the nanoparticles stability, all pellets were resuspended in deionised water and their zeta potentials measured. It should be noted that due to the presence of ionic species within buffer solutions and consequently formation of oxides over cell's electrodes, resuspension in PBS 7.4 buffer is not applicable.

In a general view, the incubation of proteins onto doped, or non-doped, T2 samples resulted in an increase of stability, with zeta potentials equal or lower than -30.0 ± 1.0 mV, for both 30 min and 2h points. It is also noteworthy that the adsorption of proteins with positive net charge at the experiment's pH of 7.4 (e.g. lysozyme), resulted in slightly more positive zeta potentials, of approx. -10.0 mV. The fact that such result was mainly obtained with RhISO-doped particles, allowed us to confirm the previously stated preference of RhISO molecules for the surface of silica nanoparticles. These results are in accordance with previously reported works [60], where protein-coated silicas' zeta potentials are known to decrease or increase when above or below proteins' isoelectric point, respectively. A full table with all measured mean zeta potentials (from triplicates) can be found on Table AIV.2 (**Annex IV**).

Therefore, we can conclude that, beside pores adsorption, surface adsorption is an ever-present phenomenon with significant influence over our system's stability, that may contribute to the extraction capacity of the herein developed devices. Particularly, when doped with RhISO.

5.3 Particle-Protein Interaction Validation

As a final approach, SBA-16 T2 samples were then used to prove the existence of particle-protein interactions through an electrophoresis analysis detailed in **7.3.7**. Thus, both pellets and supernatants, from 1:4 ratio trials, were run in a SDS 1D-PAGE gel. From the digitalised gels, present in Figure 5.3, we can conclude that our system is indeed capable of extracting proteins, even if not totally, with some selectivity towards particular proteins. Differences between intensities of proteins' characteristic bands in supernatants and pellets show us a discrepancy amid protein quantities in each of the fractions, with darker and lighter bands corresponding to higher and lighter amounts, respectively.

Additionally, the usage of RhISO and RhNHS as anchoring agents within the pores showed no apparent changes over the system's selectivity and extraction capacity, as no substantial changes between bands were observed. Unfortunately, solely by spectroscopic analysis was it possible to determine the

true amount of proteins in each supernatant and pellet fractions and thus, have a thorough understanding.

Both chromophores' behaviours and affinities were also traced under a 365 nm UV lamp, although without success, for no visible bonding between proteins and chromophores existed. As it is possible to observe in Figure AIII.4 (**Annex III**), due to the denaturing effect of the SDS reagent no chromophore was able to remain bonded to proteins, having then run till the bottom of the gels.

This denaturing effect was again confirmed when analysing haemoglobin bands. The acquirement of a 16 kDa band, rather than its characteristic 64 kDa band, proved that during electrophoresis SDS disassembled any existing quaternary of tertiary units, leaving behind secondary structures of smaller molecular weight (Figure 5.3).

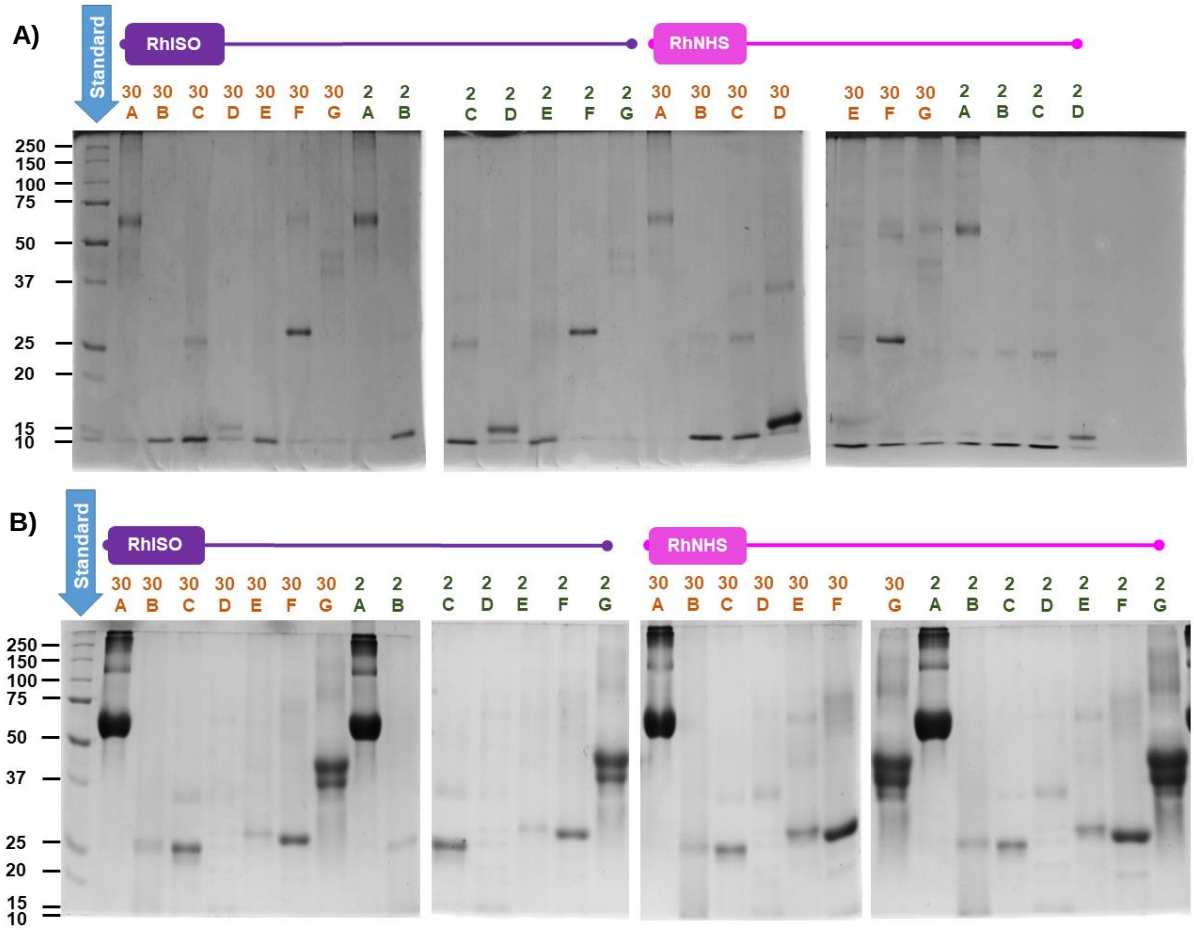

Figure 5.3 | A) Pellets (+20% lightning & +40% contract) and **B)** supernatants (+20% lightning & +20% contract) SDS 1D-PAGE electrophoresis digitalized gels, with 30 min (green) and 2h (orange) 1:4 ratio samples. Where, A = BSA, B = LYS, C = Cyt C, D = Myo, E = Hb, F = CA, G = OVA.

Even though incubation assays were performed for both 30 min and 2h points, only the first were analysed due to their significant analytic importance, since NHS-protein interaction is known to last approximately 30 mins (at the experiment temperature and pH of 7.4) and a fast extraction mechanism is herein aimed. Notwithstanding, 2h points served again to observe any existing time-dependent saturations and / or degradations.

A tracing of both chromophores fluxes was also aimed. Regrettably, a possible masquerading effect by the Bradford reagent-protein complex (max Abs at 559 nm) over existing RhISO and RhNHS peaks (at 550 nm and 556 nm, respectively) made it impossible to quantify any exiting quantities of the latter. Nonetheless, due to its importance towards a full understanding of the mechanisms behind the existing mass transfer and interactions within the developed systems, new incubations studies are being targeted at the moment.

5.4 Concluding Remarks

Concisely, from the above performed trials it is safe to state that the here in developed system was capable of effectively extract proteins from their media, with a positive crescent tendency on the amount of loaded protein (% L), due to increase of available initial protein quantity. A maximum of protein extraction is achieved with ovalbumin, for all cases, with % L and extraction capacities of about 44-52% and 464-519 mg/g, respectively. Conversely, all particles showed a certain non-reactivity towards Myo and Cyt C.

The introduction of chromophores within the system resulted in a general increase of its capability to extract proteins from their media, with a loss of selectivity for smaller doped-pores rather than larger ones, where RhNHS and RhISO introduction played no significant role. The chromophore-particle-protein interaction was hypothesised to be not only size, shape and volume dependent, but also a result of the available NH_2 groups within each protein structure.

It was also concluded that the adsorption of proteins has a stabilizing effect over nanoparticles, with surface adsorption an ever-present and important factor, along with the desired pore adsorption, towards protein extraction. Additionally, an incubation time of 30 minutes showed to be the more appropriate condition when fast extracting proteins, for times above that (i.e. 2h) resulted in either destabilisation or degradation.

Nonetheless, it can be stated that the production of an efficient system capable of hastily extract proteins from certain media has been successfully achieved, and that the introduction of physically adsorbed luminescent probes with affinity towards biological molecules was, as expected, an improvement to the system by increasing its loading capacity. Hence, giving it the opportunity to work as a novel departing material for future applications on separation techniques.

6

Use of dye-doped mesoporous nanoparticles for pollutant detection. Assays in real tap water and urine.

Looking for an environmental application, the already developed system based on L5-doped mesoporous SBA-16 nanoparticles had its ability to sense and extract pollutant ionic species from aqueous media tested. Hg^{2+} ions were the main target of this study, but Pb^{2+} and Cu^{2+} ions, possible competing agent, were also tested. Tests in water were solely made on pure solutions of each metal.

RhNHS-doped mesoporous probes were also tested, against Hg^{2+} ions, in either aqueous or urine samples.

Keywords: L5, porphyrin, Hg^{2+}, sensing, extracting, RhNHS, solid-state

6.1 Detection and Extraction Trials with L5@SBA

Finally, moving towards a more environmental approach, we sought the employment of the so far developed systems of dye-doped mesoporous silica nanoparticles on the sensing and capture of ionic metal pollutant species. The main target of this study was the 2+ ionic form of mercury, known to be accountable for several reported pollution and health issues even at low exposure concentrations. Detection limits of the same magnitude as that reported for other Hg^{2+} porphyrin-based sensing devices [90, 91], were aimed.

For that reason, the use of a new, not yet published, water-soluble porphyrin variant (**L5**) was essential to create a trapping colorimetric solid-state mechanism able to selectively and hastily sense and bind target ionic species. With an heme group this compound is able to, when coordinating a Hg^{2+} ion, change its colour from a brown to a yellowish-green and thus serve as an optical probe towards sensing ions' presence. Additionally, this phenomenon is accompanied by a quenching of the former's fluorescence. Unfortunately, its interaction with Hg^{2+} is not unique and Pb^{2+} and Cu^{2+} are also known to have a certain propensity to bind to this compound and produce similar colorimetric responses. Thus, with L5 compound successfully loaded onto SBA-16 M2 T3 silica nanoparticles we proceeded to its testing in spiked aqueous samples with concentrations ranging from 10^{-2} M to 10^{-6} M.

Notwithstanding, it should be noted that for these trials two approaches were followed: 1) L5-doped SBA-16 (L5@SBA) T3 particles (max. of 50 mg/g) were used on a set of Hg^{2+} concentrations varying from 10^{-2} M to 10^{-6} M; and 2) other L5@SBA T3 particles (max. of 12 mg/g) we applied were employed on narrower gap of concentrations from 10^{-4} M (=50 ppm) to 10^{-5} M (=5 ppm). The last, being also applied against Pb^{2+} and Cu^{2+} solutions, on the same range. Following the protocol thoroughly detailed in **7.4.1**, colorimetric calibration curves and detection limits were determined based on observable colour changes, under both visible and UV radiation, and on the progression of emission spectra for 1 mg L5@SBA batches.

A naked eye-based evaluation on the response of the system when following the first approach, showed a clear formation of a colour gradient from a concentration of 10^{-6} M up till 10^{-2} M. However, as shown in Figure 6.1, a significant change from the characteristic brown colour of L5 was only perceivable at concentrations equal or above to 10^{-4} M, which settled a limit of detection way above that established by EPA, of 20 – 2 ppb (10^{-7} to 10^{-8} M) for drinkable waters [88].

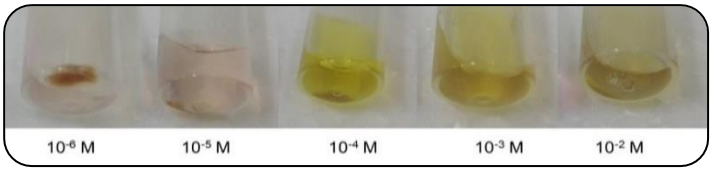

Figure 6.1 | Colorimetric gradient of L5-doped SBA-16 with growing concentrations of Hg^{2+} aqueous solutions.

In a way to overcome this sensibility issue, solid-state emission assays were performed over all dry-pellets, excited at 579 nm (Q-band tail). The once undistinguishable 10^{-5} M and 10^{-6} M samples showed now significant spectral differences with distinct quenching degrees, as it is perceived in Figure 6.2-a. Under a 365 nm UV lamp, a finer, even if just slightly, colour gradient is also perceivable, with total quenching at a concentration of Hg^{2+} of 10^{-3} M (Figure 6.2-b).

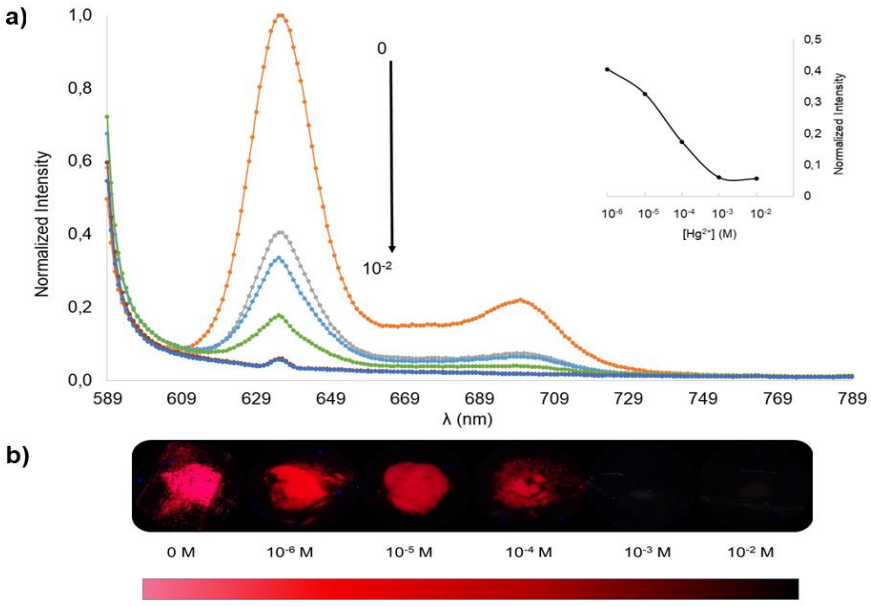

Figure 6.2 | (a) Solid-state emission spectra of L5@SBA upon addition of increasing Hg^{2+}concentrations, at 579 nm; All intensities are normalized for a blank maximum of $5.6x10^6$ csi and presented in a logarithmic scale. **(b)** Photos of L5@SBA in the presence of different Hg^{2+} concentrations, under a 365 nm UV lamp.

From the above spectra, we can also conclude that a saturation / quenching point is reached in between 10^{-4} to 10^{-3} M curves, when most, if not all, L5 coordinating centres are bound to the equivalent number of Hg^{2+} ions.

Nevertheless, fearing that a masquerading effect could be at work for the collected data below 10^{-4} M, due to the relatively large amount of porphyrin used in these trials, we moved to a second approach by going through a narrower range of concentrations with a lower amount of total available L5 porphyrin (Figure 6.3). This tactic also allowed the elimination of the L5 dissolution issue in aqueous solutions, a visible problem in Figure 6.1 that difficults Hg^{2+} extraction by allowing the L5 - Hg^{2+} complex to move freely through the liquid. Thus, the use of new L5@SBA samples with sturdily adsorbed L5 molecules ensured that any coordination or entrapment reactions happened within SBA pores, rather than in the surrounding medium.

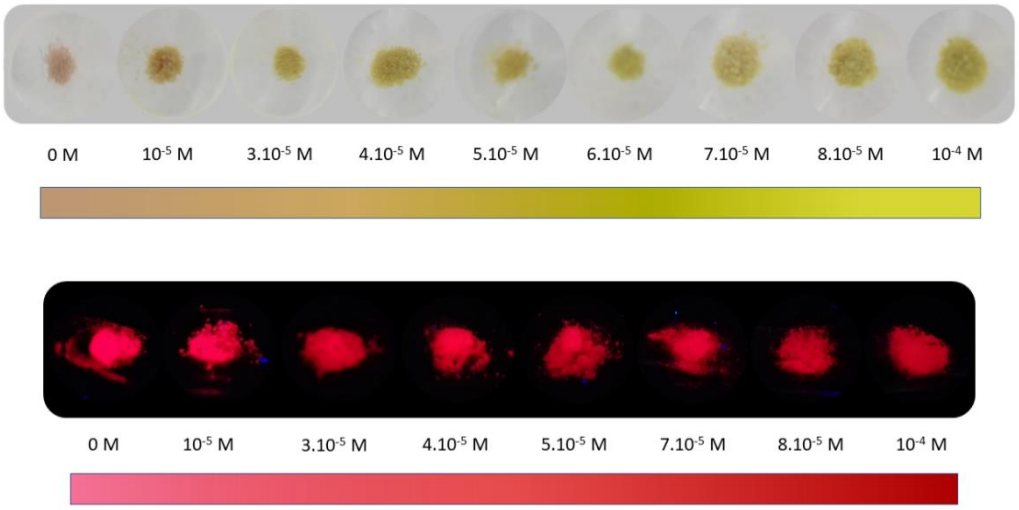

Figure 6.3 | Colorimetric (above) and fluorescent (below) calibration curves of L5@SBA in the presence of different **Hg^{2+}** concentrations, ranging from 5 ppm to 50 ppm. Fluorescence photos acquired under a 365 nm UV lamp.

According to the photos, the system allowed now for a clear progression, at naked-eye, between concentrations of 50 ppm to 5 ppm (10^{-4} to 10^{-5} M, from Hg^{2+} stock solutions of 2mL), something impossible in the above analysis. Besides, we could risk saying that the system has a naked-eye limit of detection (LD) that could reach concentrations below 5 ppm (10^{-5} M), for a significant colorimetric gap is evident between both blank and 5 ppm sample. This could position the system near to most reported high sensitive devices, with sensibilities on the ppb scale, supporting its future application.

Additionally, the clear difference between both 10^{-5} M approaches' pellets is proof of the previously existing masquerading effect. Moreover, UV observations under a 365 nm lamp showed a more finer and steady evolution of fluorescence.

From a spectral point of view, there is an accordance with the previously obtained spectra, with data approximately fitting in the same array of intensities for the same range of concentrations (Figure 6.4). Herein the detection limit was not possible to determine, but through the emission spectra analysis we can estimated that is lower than 5 ppm.

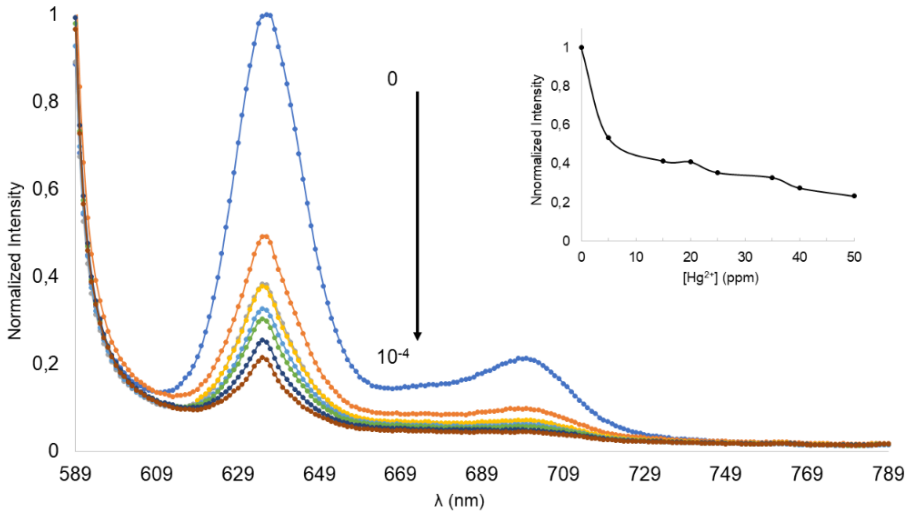

Figure 6.4 | Solid-state fluorescence spectra of L5@SBA upon addition of increasing Hg^{2+}concentrations (5, 15, 20, 25, 35, 40, 50 ppm), under excitation at 579 nm; All intensities are normalized for a L5 blank maximum of $5.6x10^6$ csi.

As mentioned before, previous studies have demonstrated that L5 porphyrin is also colour responsive to Pb^{2+} and Cu^{2+} ions and thus, also due to their impact on the environment, their influence over the developed L5@SBA system was also evaluated. Figure 6.5 is the culmination of all resulting spectra of (A) Pb^{2+}, (B) Cu^{2+} and (C) Hg^{2+} additions over L5@SBA samples, with concentrations ranging from 50 ppm to 5 ppm.

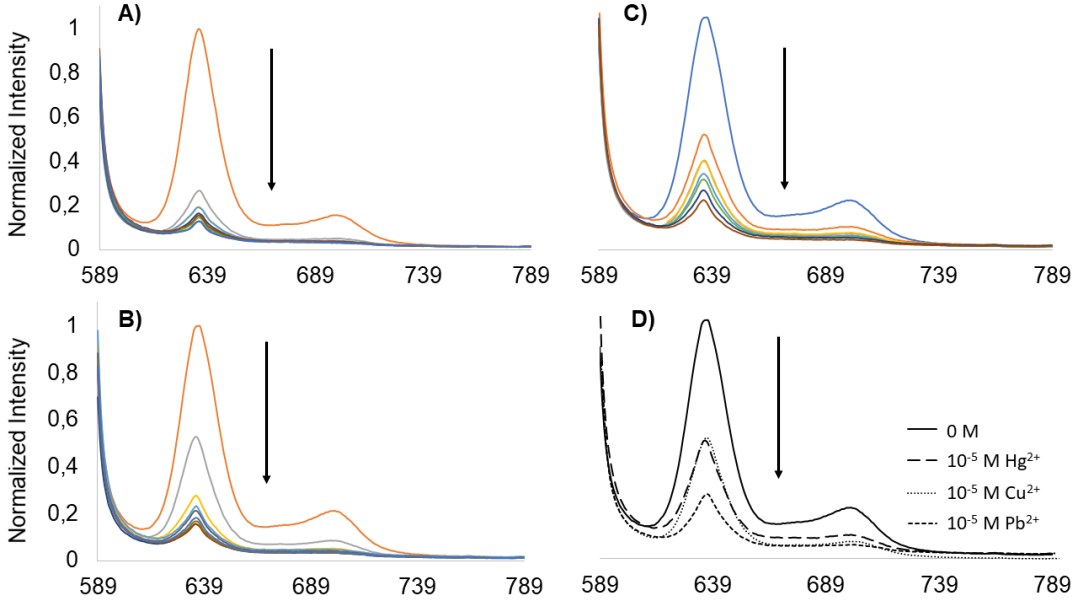

Figure 6.5 | Solid-state emission spectra of L5@SBA upon addition of increasing **(A)** Pb^{2+} **(B)** Cu^{2+} or **(C)** Hg^{2+} concentrations (5, 15, 20, 25, 35, 40, 50 ppm), under excitation at 579 nm with a 2 nm slit. Superimposed spectra after 10^{-5} M solutions addition, of all metals. All intensities are normalized for a L5 blank maximum of $5.6x10^6$ csi.

As shown in Figure 6.5-D, the addition of the same concentration of each metal produces distinct decays on all emission spectra of L5@SBA. Whereas Hg^{2+} and Cu^{2+} produce a diminishing of fluorescence on almost the same degree (normalised emissions of 0.53 and 0.52, respectively), Pb^{2+} induces a more intense weakening of its maximum (with 0.26). Consequently, both ions have a competing character over the binding of Hg^{2+} ions with L5, with Cu^{2+} reacting at same rate as Hg^{2+} and

Pb^{2+} at a higher one. Therefore, on a hypothetical separation assay, i.e a metal-affinity chromatography, the upper fraction and the first to be immobilised would be that contaminated with Pb^{2+}, followed by the competing Cu^{2+} and Hg^{2+} fractions.

Figure 6.6 and Figure 6.7 show the obtained calibration curves for both Pb^{2+} and Cu^{2+}, where a difference in colour is evident, with Pb^{2+} showing a yellowish-green and the Cu^{2+} a light pink when coordinated by L5@SBA.

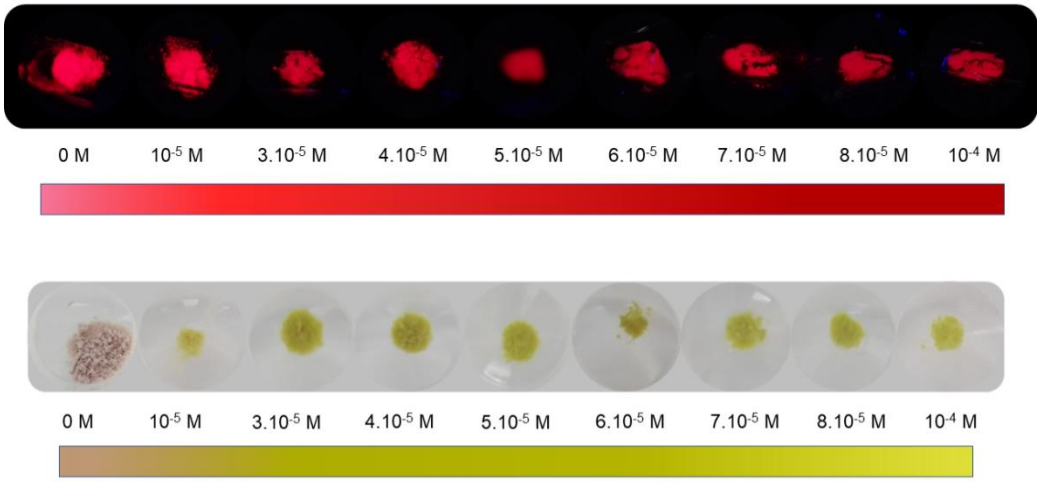

Figure 6.6| Colorimetric (below) and fluorescent (above) calibration curves of L5@SBA in the presence of different **Pb^{2+}** concentrations, ranging from 5 ppm to 50 ppm. Fluorescence photos acquired under a 365 nm UV lamp.

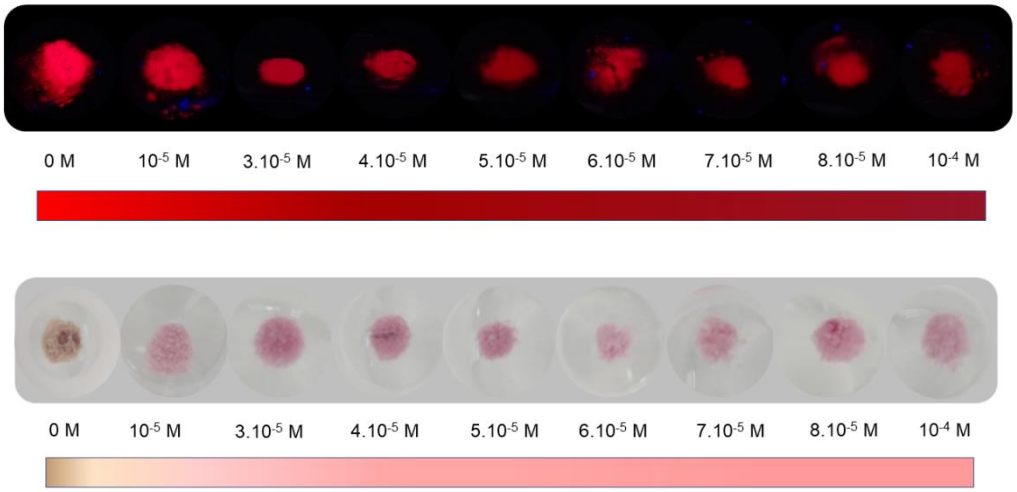

Figure 6.7 | Colorimetric (below) and fluorescent (above) calibration curves of L5@SBA in the presence of different **Cu^{2+}** concentrations, ranging from 5 ppm to 50 ppm. Fluorescence photos acquired under a 365 nm UV lamp.

Naked-eye limits for these metals are undoubtedly below the 10^{-6} M mark, for considerable changes in colour are visible between this and L5@SBA blanks. Future experiments will culminate on determining both limits of detection, by lowering the treated concentrations. Nevertheless, the system's extraction capacity was determined by means of a quantification of the remaining Hg^{2+} (or Pb^{2+}, or Cu^{2+}) quantity in solution through an inductive coupled plasma (ICP) technique. A mean extraction capacity of 86% ±

7% was obtained and the sensibility of the system extended down to in-solution Hg^{2+} concentrations of 1 ppb, below the mark of 2 ppb established by EPA for drinkable waters.

The inclusion of reversible and reusable features on most cleaning and sensing devices has been one of the most critical points when considering a real application and the development of a cheap and efficient device. Therefore, reversibility tests were carried out with the aid of EDTA on the 10^{-2} M Hg^{2+} doped L5@SBA, with consequent additions of 0.5 mL of 10^{-2} M, $2x10^{-2}$ and $3x10^{-3}$ M (1 eq., 2eq. and 3 eq.) EDTA solutions. Unfortunately, no changes in the pellet colour were evident as it kept its yellowish-green shade, meaning that L5 heme group has a stronger coordinating capacity than that of EDTA. Possible future experiments on the system reversibility might rely on the use of HCl solutions, for it has been already reported the possibility to totally revert porphyrins to its original state by a simple dipping in dilute acidic solutions, with further neutralisation of the material [90]. However, silica interaction with acidic conditions might create additional issues, such as degradation.

6.2 Detection and Extraction Trials with RhNHS@SBA

Several systems have also been reported to use Rhodamine B derivatives on the detection and removal of ionic species, namely mercury 2+ or methylmercury 2+, from aqueous media [79, 85, 89]. Hence, a quick check on the previously synthesised RhNHS- and RhISO-doped nanoparticles was made regarding the detection of Hg^{2+} ions in both aqueous or biological media.

Whether RhISO showed no visible changes, RhNHS@SBA particles suffered a clear blueshift in colour at naked-eye, from light pink to yellow, for Hg^{2+} concentrations above 10^{-3} M. The shift was later confirmed with a fluorescence assay, under excitation at 556 nm, and a visualisation under UV light, at 365 nm. The results are summarised in Figure 6.8.

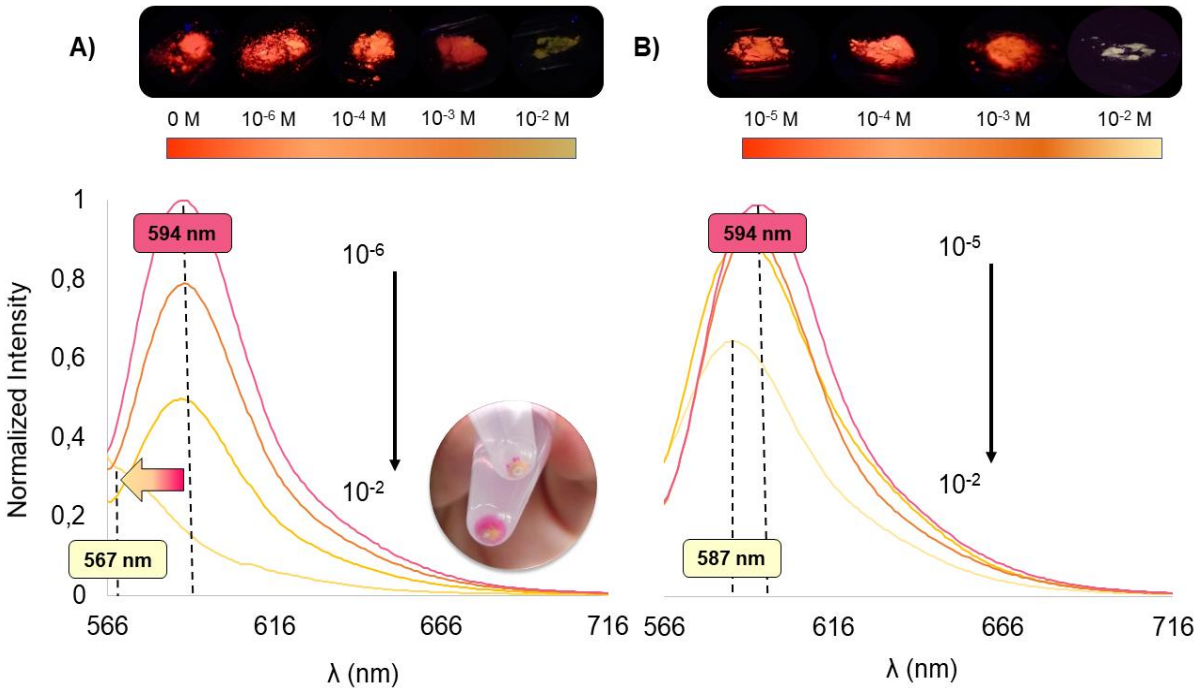

lamp. All intensities are normalized for a maximum of 1x10ᐟ csi.

From the figure above it is also clear the retarding effect of urine in this shifting, with water samples shifting all the away to a maximum at 567 nm and urine ones towards another at 587nm. The cause of this phenomenon may possibly lay on the presence of either biological or ionic competing species in the samples.

Although pH is known to stabilize the NHS group (thus reducing the possibility of any attacks from protein sources) it can also be the foundation of the impeding, as it has also been confirmed, by accident (Figure 6.9), that in acidic media RhNHS shifts at naked-eye from its pink colour to a strong dominant orange. This colorimetric change and increase in intensity have been reported to result from the preference of rhodamine B compounds for its cationic form (with intensive fluorescence) at low pH values [162, 163]. Therefore, it could be supposed the existence of a competition between metal ions coordination and the opening of the coordinating site, responsible for the above-mentioned differences in shifts.

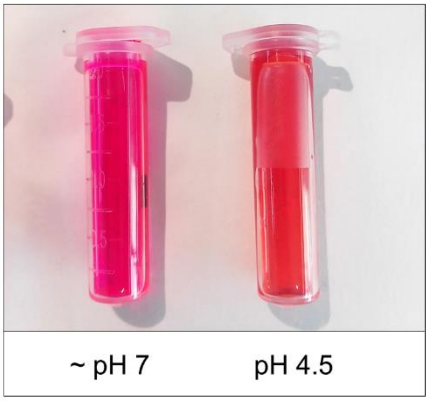

Figure 6.9 | RhNHS colour shift with pH.

Therefore, although a weak naked-eye colorimetric probe, RhNHS@SBA nanoparticles presented itself a good fluorometric device for the detection of Hg^{2+} ions based on the shifting phenomenon, rather than on quenching responses. Its reversibility was also tested with an EDTA wash (1 eq.) and an immediate recovery was visible after fluorescence analysis.

6.3 Concluding Remarks

In light of the obtained results it can be concluded that, despite the integration of the L5 porphyrin within SBA pores, no change in its sensing properties was evident, for the presence of Hg^{2+}, Pb^{2+} and Cu^{2+} ions in solution was able to produce significant colour changes (from its characteristic brown to yellowish-green, light green and light pink, respectively).

Additionally, to avoid masquerading effects and consequent foul quantifications, a limit of loaded porphyrin within SBA pores was confirmed to exist and the developed system able to, at naked-eye, detect concentrations of any of the ionic species down to 5 ppm, with a hypothesised limit of detection at the ppb scale. Thus, going in accordance to the limits established by EPA for drinkable waters and supporting their usage for the effective detection and extraction of toxic ionic metals.

A higher affinity for Pb^{2+} ions was also registered, and future competition assays in complex ionic media will be developed to understand their influence over Hg^{2+} extraction.

RhNHS usage for the detection and extraction of the same species in water, produced slight different results, with a not so significant change, at naked-eye, in colour (pink to yellow, for concentrations above 10^{-3} M) and a strong shift in its emission maximum, from 594 nm to 567 nm. Trials in urine also disclosed the system possible susceptibility to pH and salts concentration, with both favouring additional competing behaviours against Hg^{2+} coordination. Hence, future supplementary trials are to be performed, with further quantification by ICP analysis, and an optimisation of its conditions need.

Finally, while on one hand no reversibility was achieved for L5-doped particles due to the L5 – Hg^{2+} complex high stability, on the other, RhNHS-doped devices displayed an almost immediate reversion, after washing with EDTA. HCl washing was also disclosed to be harmful to the system and no reversibility was achieved by this route.

7

Experimental Procedures

The development of the whole above mentioned study depends on specific materials and synthetic techniques, detailed below.

7.1 Chemicals and Starting Materials

All chemicals were of analytical grade and used as received without further purification.

1,3,5-Trimethylbenzene (TMB, 98%), Hexadecyltrimethylammonium bromide (CTAB, ≥ 98%), Pluronic F127, Trimethylorthosilicate (TMOS), Dichloromethane (DCM, puriss ≥ 99.9%), Methanol (MeOH, 99.8%), Acetone (puriss. ≥ 99.5%), Hydrochloric Acid solution (HCl, puriss. 37%), Bradford Reagent, Sucrose (≥ 99.5% HPLC), D (-) Fructose and D (+) Trehalose dehydrate (from starch, ≥ 99%) were purchased from Sigma-Aldrich.

Rhodamine B Isothiocyanate (RhISO) was supplied by Aldrich and Rhodamine B (RhB) from TCI Europe. Acetonitrile, Dimethylsulfoxide (DMSO) and Ethanol absolute anhydrous (EtOH) were acquired from Carlo Erba Reagents. N-hydroxysuccinimide (NHS) and Ammonium Nitrate (NH_4NO_3, 99.999%) were supplied by Alfa-Aesar and Cicyclohexylcarbodiimide (DCC, ≥ 99%) by Fluka. Chloroform (puriss. 99.0-99.4%) was purchased from Honeywell.

Metallic trifluomethanesulfonate (triflate) species of Mercury (II) (Hg^{2+}, salt), Lead (II) (Pb^{2+}, salt) and Cooper (II) (Cu^{2+}, salt) were obtained from Strem Chemicals and Solchemar, accordingly. Also, SDS-PAGE electrophoresis Laemmli SDS (x1) Buffer solution was bought from Alfa Aeser and Tris Base-Glycine-SDS TGS (x10) Buffer, pH 8.3, was supplied by Bio-Rad.

Proteins used in biological assays were applied as received with no further treatment.

Bovine Serum Albumin (BSA, ≥ 97%), Lysozyme (from chicken egg white), Cytochrome C (from equine heart, ≥ 95%), Myoglobin (from equine heart, ≥ 90%), Haemoglobin (human) and Carbonic Anhydrase (bovine erythrocytes) were purchased from Sigma-Aldrich, while Ovalbumin (albumin from hen egg white) was acquired from Fluka.

Solutions and dissolutions were performed with the use of ultra-purified Millipore Milli-Q® water. Buffer solutions were prepared using Phosphate Buffered Saline 7.4 tables (PBS) and Tris Base 8.5 supplied by Sigma-Aldrich.

A PBS pH 7.4 buffer solution (0.01 M) was prepared from total dissolution of 2 tablets of PBS pH7.4 saline mixture, supplied by Sigma-Aldrich, in 1 L of deionised water. Additionally, a PBS pH 4.5 buffer solution was prepared by adjusting a 0.01 M PBS pH7.4 buffer solution pH with dropwise addition of an 0.01 M HCl aqueous solution. For the formulation of a 0.01 M Tris Base 8.5 buffer solution (total volume = 100 mL) 121,2 mg of Tris Base salt were mixed with 31 µL of a ≥ 37% HCl solution (approx. 12 M, puriss) and deionised water.

7.2 Instrumentation

X-ray diffraction (XRD) was used to identify crystal phases and structural arrangement of the synthesised solids. These analyses were performed with RIGAKU MiniFlex II X-ray diffractometer equipped with a Cu-Kα source (30 KV/15 mA). Measurements were obtained for 2θ angles ranging from 3º to 40º. Structural and binding characterisations were run on a Spectrum Two IR (solid-state FT-IR), from PerkinElmer. Spectral data collected for wave-numbers from 400 to 4000 cm^{-1}.

Particle size distribution and zeta potential quantifications were performed with a Malvern Instruments Zetasizer Helix, from Proteomass – Bioscope facility, with a He-Ne 633 nm laser (max. 100 mW), for emulsions of as-synthesised or modified SBA samples in either DMSO or water solvents. Pore size distribution and surface area determination result from the measurement of N_2 adsorption/desorption, at 77 K, in a Micromeritics ASAP 2010 (Accelerated Surface Area and Porosimetry), at the Laboratory of Analysis from FCT - UNL. Specific surface areas (S_{BET}) were estimated with the BET method [117], using the adsorption data for relative pressures ranging from 0.03 - 0.18 (for T1, T2 & T4 samples) and 0.03 - 0.30 (for T3 & T5 samples) where conditions of linearity were met [117]. Pore size distributions were calculated from the desorption branch of the isotherms using the Barrett-Joyner-Halenda analysis (BJH) [118].Total pore volume was considered the adsorbed volume at $p/p_0 = 0.95$.

Scanning electron micrographs (SEM) were obtained with a high-resolution SEM-FIB microscope Zeiss Auriga CrossBeam System, CENIMAT - FCT.

All centrifugations were carried out on a Montreal Biotech MBI Refrigerated Centrifuge, at 20 ºC and zeta potentials and hydrodynamic radius of particles were measured on a Malvern Instruments Zetasizer Helix.

UV-vis spectra were recorded on a JASCO V-650 and V-630 spectrophotometers and the fluorescence emission spectra on a HORIBA-JOBIN-YVON Fluoromax-4 equipped with an optic fibre. Absorbance assays were also performed at a Nanodrop 1000 Spectrophotometer (ThermoFisher), with a pulsed xenon flash lamp. All equipment from Proteomass – Bioscope facility.

7.3 Synthesis, Functionalisation and Protein Assays

7.3.1 SBA-16 Synthesis & Characterisation

All SBA-16 samples were synthesised by adapted acidic sol-gel routes. Three main synthetic routes were selected as reported by Rivera-Muñoz *et al* [26], dos Santos *et al* [31] and Katiyar *et al* [16] and carried out through the synthesis process, with adaptations.

As detailed by Rivera-Muñoz *et al* [26] (**Method 0**), 0.4 g of pluronic F127 ($PEO_{106}PPO_{70}PEO_{106}$) were dissolved in 3 mL of deionised water, in a rounded bottom vessel, followed by the addition of 10 mL of a 2 M HCl solution. The mixture was stirred (400 rpm) at room temperature till full dissolution of F127. Once a clear solution was obtained, 0.85 g of TEOS were added to and the resulting mixture stirred for 20h, at room temperature.

After the given time, the resulting mixture was subjected to an aging process at 80 ºC (353 K), under continuous stirring, for 24h. The final mixture was washed with deionised water (x1) and methanol (x2), at 6000 rpm each. The solid was finally let dry at air.

In **Method 1** (**M1**), as reported by dos Santos *et al* [31], 0.17 g of pluronic F127 were dissolved in 5.04 mL of a 2 M HCl aqueous solution and stirred (500 rpm), at 50 ºC (323 K). After total dissolution, 0.375 g of TMOS were added, drop-wisely, to the previous mixture and the stirring turned off. The resulting mixture was made rest at static conditions and 50 ºC, for 24h. After the given time, the blend was aged at 80 ºC, for 24h, at static conditions.

Similarly, the final mixture was washed with deionised water (x1) and methanol (x2), at 6000 rpm each, and dried at open air conditions.

Adapted from the synthetic pathway proposed by Katiyar *et al* [16], **Method 2** (**M2**) considers the synthesis of large sized SBA-16 particles with modulating pore sizes. As synthetic procedure, 0.3 of pluronic F127 were firstly dissolved in 6 mL of a 1.5 M HCl solution, into a rounded bottom vessel; forming Solution A. Separately, 0.06 g of CTAB were dissolved, at 35 ºC, in 2.5 mL of deionised water; forming Solution B.

Depending on the targeted pore size, the addition of the swelling agent TMB to the Solution B is an option and ranges on a TMB : F127 ratio of 0 to 0.5 (w/w). As both extremes were tested, 0 and 0.15 g (174 µL, for ρ = 0.864 g/mL) of TMB were added to solution B, accordingly, for the synthesis 6 nm and 12 nm pores.

Once totally dissolved, Solution B was added, along with 2 mL of EtOH (100%), to an already stirring (500 rpm) Solution A, at 35 ºC; forming the Surfactant Solution. To this later solution, 1 mL of TMOS was added, drop-by-drop, and the resulting solution kept under continuous stirring (500 rpm), for 45 minutes at 35 ºC.

Afterwards, the resulting mixture was kept under static conditions at 75 ºC, for approximately 10h. Subsequently, the blend was aged, for 24 h, at a selected temperature in the range of 80 ºC to 120 ºC

(353 K – 393 K), depending on the targeted pore size. As both minimum and maximum pore sizes were tested, temperatures of 80ºC and 120 ºC were used during the aging step. Similarly, the resultant mixture was then washed with deionised water (x1) and methanol (x2), at 6000 rpm, and dried at open air conditions.

It is to note that, all HCl aqueous solutions were prepared, for a maximum volume of 50 mL, from a concentrated HCl solution of 37%. Also, solids total dryness is only achieved after 4 to 5 days.

Template removal, for either Method 0, 1 or 2 samples, was achieved using a template removing solution (TRS) of 60 mg of ammonium nitrate in 20 mL of methanol (or a 3:1 w/v ratio of NH_4NO_3 : MeOH). As-synthesised SBA powders were dissolved in 20 mL of TRS, and submitted to reflux at 100 ºC (373 K) under continuous stirring, for 8h; followed by 8 more hours of continuous stirring at room temperature. The resultant blends are, again, washed with deionised (x1) and methanol (x2), at 6000 rpm, and let dry at air.

Method 2 samples of smaller pore size (TMB : F127 = 0) were denominated as T1, T2 and T4 (replicates), whilst larger pore samples (TMB : F127 = 0.5) T3 and T5 (replicates). Also, all centrifugations were carried out on a MPW-223e laboratory centrifuge, at room temperature.

7.3.2 SBA-16 Surface Functionalisation

Surface functionalisation and further stabilisation (diminishing of aggregation) of SBA-16 M2 T2 particles was achieved by the addition of sugar molecules: namely sucrose, fructose and trehalose.

As proposed by Zhou *et al* [143] a SBA : Sugar ratio of 1:1 (w/w) was firstly tested. From an initial and fixed 5 mg/mL SBA-16 solution (total volume of 1.5 mL, with acetone as dispersing medium), 0.5 mL were mixed with 0.5 mL of each sugar aqueous solution (of also 5 mg/mL) and let stir (300 rpm) at room temperature, for 12h.

After the established time, all mixes were centrifuged (7000 rpm), for 15 min, and pellet and supernatant fractions isolated. The same procedure was repeated for 1:2 and 1:3 ratios with sugar concentrations of 10 mg/mL and 15 mg/mL, respectively.

All pellets were resuspended in deionised water and analysed in a Malvern Instruments Zetasizer Helix, regarding their particle size distribution and zeta potential. Substitution of acetone by ultra-filtered Millipore water as dispersing medium for SBA-16 particles was also tested (following the same procedure) and its results compared with those of acetone.

7.3.3 RhNHS Synthesis & Purification

The synthesis of a N-hydroxysuccinimide (NHS) Rhodamine B derivative chromophore (RhNHS) herein developed is that described by Xu *et al* [148].

Briefly, 0.24 g of Rhodamine were dissolved in 15 mL of Dichloromethane (DCM), followed by the addition of Dicyclohexylcarbodiimide (DCC) and NHS on a molar ratio of 5 (RhB : DCC : NHS, 1:5:5).

The final mixture was stirred at room temperature for 6 days. The reaction was followed thin layer chromatography (TLC) analysis, using as eluent MeOH : DCM 1:9.

Subsequently, the solvent was evaporated and the residue purified by a silica gel column chromatography (eluent: MeOH:DCM 1:9). The resulting fractions were combined and the product, RhNHS, obtained as a purple powder.

Due to the presence of dicyclohexylurea (DCU) salts, a by-product of the RhNHS synthetic reaction, the powder was treated with cooled acetone, followed by DCU extraction through filtration. This last step was performed twice, followed by solvent evaporation under reduced pressure.

Compound **RhNHS** was obtained as purple powder (Yield: 0.245 g, 85 %), ESI-TOF-MS: $[C_{32}H_{34}N_3O_5]^+$, 540.25 m/z. Elemental analysis calculated for $C_{32}H_{44}N_3O_{10}Cl$. $5H_2O$ (FW= 665.27): C, 57.70; H, 6.66; N, 6.31. Found: C, 58.17; H, 6.63; N, 6.19.

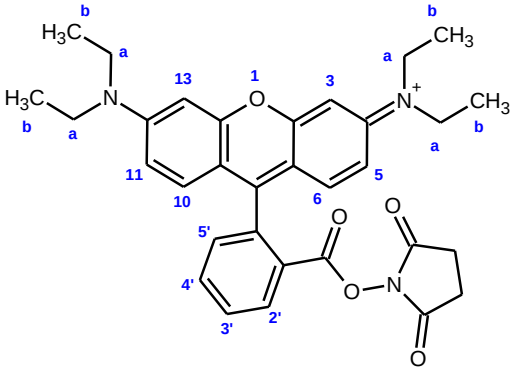

^{1}H NMR Spectrum δ_H ($CDCl_3$, 400 MHz) ppm: 1.3 (s, 12H, Hb), 2.7 (s, 2H, H_{NHS}), 3.5 (s, H8, Ha), 6.8 (s, 2H, H3, H13), 6.9 (m, 1H, H6), 7.1 (m, 2H, H5, H11), 7.3 (m, 1H, H10), 7.8 (m, 3H, H3'-H5') and 8.3 (m, 1H, H2'). ^{13}C NMR Spectrum δ_C ($CDCl_3$, 400 MHz) ppm: 14 (Ca), 48 (Cb), 36.0, 36.6 (C_{NHS}),98, 115, 116, 132, 133, 135, 157, 158, 159, 161 (aromatic C of RhB).

7.3.4 RhNHS Doping of SBA-16 Particles

RhNHS loading into SBA-16 mesopores is promoted by simple physical adsorption interactions between pore's wall and loading molecule. The protocol herein applied follows an adaptation of that proposed by Wang *et al* [149] and is valid for all SBA-16 synthesised samples. A batch of 20 mg of SBA-16 particles (from T1, T2 or T3 samples) was dissolved (with the aid of ultrasonication, if needed) in 1 mL of chloroform ($CHCl_3$) and mixed with 1 mg of RhNHS, also dissolved in 1 mL of $CHCl_3$.

The resulting solution was placed under continuous stirring (350 rpm) for 6h, at room temperature. Once finished, the mixture was washed with $CHCl_3$ (centrifugation at 9500 rpm) till washing supernatants showed a clear/transparent look. Pellet and supernatants were isolated and the last spectroscopically quantified at the Nanodrop. The amount of free RhNHS (λ_{max} = 556 nm), in solution, was given by the Lambert-Beer law, whereas SBA-16 RhNHS loading capacity (mg/g_{SBA}) was determined by mass balance.

The loading of a commercial rhodamine B isothiocyanate (RhISO) was also attained following the same procedure and quantities. Additionally, loading was also tested with the substitution of $CHCl_3$ for DMSO (total volume of 2 mL per batch), but no pellet was formed when washing. 1 mL of MeOH per mL of DMSO was added, to ease pellet formation; however, even though a pellet was formed, no RhNHS remained adsorbed within SBA-16 pores.

The resulting loaded SBA nanoparticles (RhNHS@SBA) were characterised by zeta potential, in order to evaluate the influence of loading molecules over silica nanoparticles stability.

7.3.5 RhNHS Release from SBA-16 Particles

RhNHS release trials, from RhNHS@SBA T1 particles, were performed in PBS pH 4.5, PBS pH 7.4 and Tris Base pH 8.5 buffer solutions. RhNHS release profiles were achieved after 30 min and 2h trials and the same experimental applied during RhISO release.

For each buffer solution, two samples of 2 mg of RhNHS@SBA particles (or RhISO@SBA), were prepared in two eppendorfs (one for 30 min and another for 2h of continuous release). Finally, 1 mL of the respective buffer was added to each sample and let incubate for 30 minutes and 2 hours.

At the end of the selected time, each eppendorf was centrifuged for 5 min (6000 rpm) and its supernatant spectroscopically quantified at the (Nanodrop 1000). RhNHS (λ_{max} = 556 nm), or RhISO (λ_{max} = 550 nm), released amount was obtained through the Lambert-Beer law.

7.3.6 Proteins Adsorption

The absorption of biomolecules was tested in both RhNHS@SBA and RhISO@SBA systems, with both pore sizes T2 (pore size: 3.9 nm) and T3 (pore size: 4.9 nm) taken in consideration. A set of 7 proteins was selected (BSA, lysozyme, cytochrome c, myoglobin, haemoglobin, carbonic anhydrase and ovalbumin) and all absorption tests run on pure single protein aqueous solutions. Distinct Protein : Rh*X*@SBA ratios (with, *X* = NHS or ISO) were also evaluated, namely 1:4, 1:2 and 1:1 ratios.

Additionally, batch absorption experiments were carried out on a Labnet Enduro Mini Mix 3-D Mixer, at 20 ºC.

7.3.6.1 Effect of pH over Loaded Proteins

On a first approach, the effect of pH on proteins uptake was studied, with lysozyme as a model protein.

For this aim, 0.5 mL of an initial 0.5 mg/mL stock solution of Lysozyme, in a selected buffer, were mixed with 0.5 mL of a RhNHS@SBA T1 initial 2 mg/mL stock solution, also in the same buffer. The resulting mixture (total volume of 1 mL) was incubated under continuous shaking at room temperature, for 20h. After the selected time, the mixture was centrifuged (5000rpm, for 5 min) and pellet and supernatant isolated. This procedure was repeated in PBS pH 4.5, PBS pH 4.7 and Tris Base pH 8.5 buffers. The concentration of collected supernatants was quantified at the Nanodrop 1000 Spectrophotometer at 280 nm (the maximum absorption peak of Lysozyme). Lysozyme loaded quantities were obtained through the Lambert-Beer law.

7.3.6.2 Effect of Protein Concentration over the Adsorption Process

For these experiments, different initial concentrations of each protein solution, at a fixed pH of 7.4, were mixed with 2 mg/mL suspensions of Rh*X*@SBA (T2 and T3), for 30 min and 2h. Briefly, 2 mL stock solutions of each protein had to be prepared according to tested ratios and Table 7.1 encloses all weighed amounts of proteins and pipetted volumes of PBS pH 7.4 buffer.

Table 7.1 | Weighted proteins and pipetted buffer volume for each stock solution, according to each Protein : Rh*X*@SBA ratio and initial protein concentration (with, *X* = NHS or ISO).

	1:4 Ratio	**1:2 Ratio**	**1:1 Ratio**
[ ] Prot (mg/mL)	0.5 mg/mL	1.0 mg/mL	2.0 mg/mL
m_{Prot} (mg)	1.0	2.0	4.0
$V_{7.4\ PBS}$	2.0	2.0	2.0

With, Prot = BSA (bovine serum albumin), LYS (lyzosime), Cyt C (cytochrome c), Myo (myoglobin), Hb (haemoglobin), CA (carbonic anhydrase) and OVA (ovalbumin).

Once prepared, 0.5 mL of each protein solution was mixed with 0.5 mL of already prepared 2 mg/mL Rh*X*@SBA T2, or T3, suspensions (in PBS pH 7.4 buffer), in eppendorfs. The resulting mixtures (total volume of 1 mL) were shaken for 30 min and 2 h (distinct samples). After centrifugation at 6000 rpm, for 5 min, both pellets and supernatants were isolated. The supernatants were then submitted to a Bradford assay (see **7.3.8**) for proteins quantification. Figure 7.1 summarizes the whole experimental procedure, pre-centrifugation.

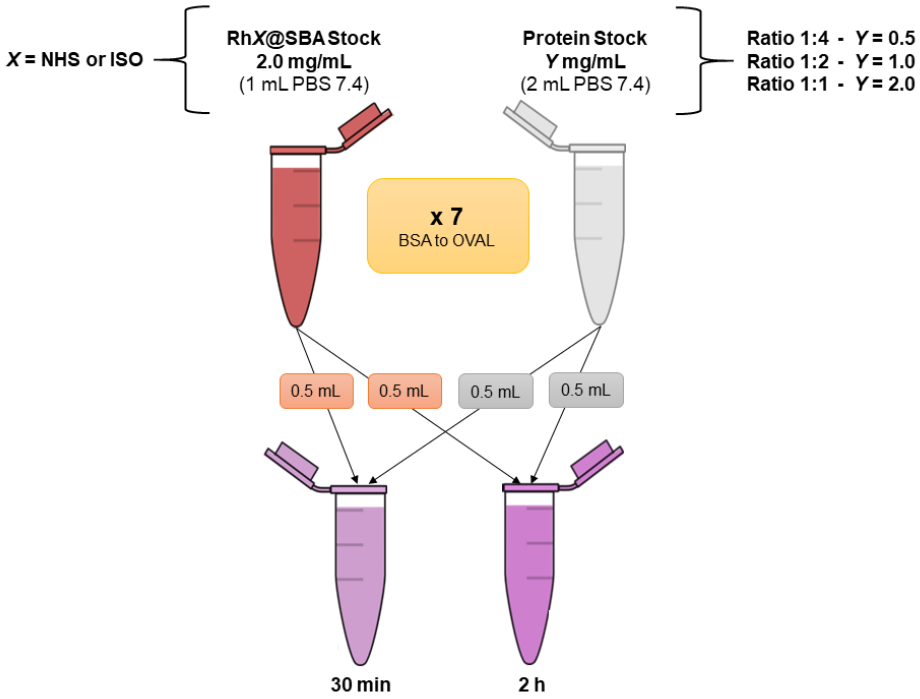

Figure 7.1 | Experimental procedure for proteins adsorption experiments sample preparation.

7.3.7 1D PAGE Electrophoresis

The elaboration of this technique followed the protocol proposed by the BioScope Research Team and was run on a Mini-PROTEAN® Tetra Cell apparat **(Annex V**).

7.3.7.1 Samples Preparation for SDS PAGE

For this technique, only 1:4 incubation ratio RhNHS@SBA T1 and RhISO@SBA T1 pellets and supernatants were analysed, with proteins quantities ranging between 0.058 - 0.25 mg for supernatants and 0.133 - 0.190 mg for pellets.

In a first approach, it was necessary to dry both supernatants and pellets to obtain totally dry protein samples. Whilst supernatants (total volume of 1mL) were directly dried, pellets had to be previously resuspended in 1 mL of deionised water (DI H_2O) and transferred to 1.5 mL eppendorfs for further evaporation to dryness at a UNIVAPO Model H Vacuum Concentrator Centrifuged, with vacuum control gauge and Teflon coated chamber; for 12h.

It is to note that only 0.5 mL of each pellet resuspension were evaporated to dryness and used on the next steps of this technique, for the remainder 0.5 mL were saved for zeta potential analysis.

All dry protein samples (supernatants and pellets) had then to be prepared in a two-way approach, before loading. Firstly, to avoid saturation and formation of protein blurs within gels, proper dilutions of all samples were performed according to protein initial available quantities for analysis. Secondly, to ensure a homogeneous negatively net charge on all proteins, addition of Laemmli SDS-PAGE 1D buffer solution was necessary. Note that, distinct preparations were followed for proteins on both supernatants and pellets

Once dry, proteins present in supernatants (ranging from 0.058 to 0.25 mg) were resuspended in 36 µL of deionised Milli-Q water and mixed vigorously to ensure a homogeneous dissolution. From the resulting solutions, 15 µL of each were pipetted onto new 0.5 mL eppendorfs and mixed with 5 µL of Laemmli SDS-PAGE 1D buffer solution (x4 diluted, for a sample's total volume of 20 µL).

Regarding the already dry pellets (with protein quantities ranging from 0.133/2 to 0.190/2 mg), each was directly resuspended in 20 µL of a 4x diluted solution of Laemmli SDS-PAGE 1D buffer. 5 µL of all samples were then loaded onto the already prepared electrophoresis gels, with protein quantities ranging from 6 – 26 µg and 17 - 24 µg on supernatant and pellet samples, respectively.

7.3.7.2 Samples Loading onto the SDS PAGE

After proper assemble of the cassette sandwich on the electrode apparatus, the inner chamber of the mini-tank was filled with an already prepared Tris Base-Glycine-SDS TGS Buffer, pH 8.3 running buffer. 5 µL of each sample were then slowly loaded with a pipette onto gels' wells, along with a molecular weight calibration standard (Precision Plus Proteins standards on a 4-20% Tris-HCl Criterion™ Gel). Loading schematics are shown in Figure 7.2.

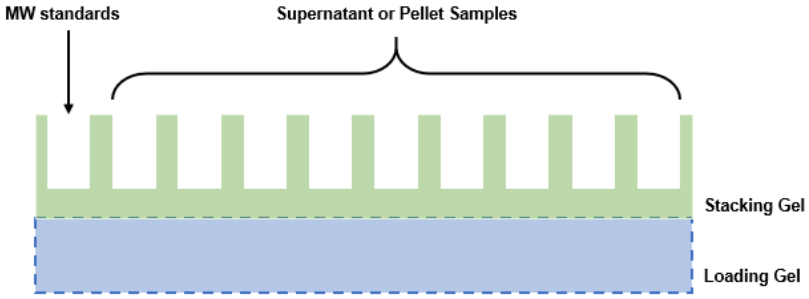

Figure 7.2 | Loading schematics of supernatant or pellet samples on an electrophoresis gel.

Each electrophoresis assay was run for 50 min, at 200 V and 400 mA. After the appointed time, all gels were removed from the Mini-PROTEAN Tetra Cell, washed with DI H_2O and stained with staining solution of Coomassie Blue R-250, for at least 1h.

Finally, after proper staining, gels were distained with DI H_2O for another hour and digitalised at a Genomics Solutions' Propic IV.

7.3.8 Bradford Protein Assay

For the determination of all proteins concentrations, supernatants from all incubation ratios, a 96-well plate spectroscopic methodology, assisted by the colorimetric Bradford reagent, was applied. According to the protocol supplied by the BioScope Research Team (**Annex VI**), for the Bradford Assay, the preparation of a BSA calibration curve from a 100 µg/mL BSA stock solution was needed and followed the schematics of Table 7.2.

Table 7.2 | BSA calibration curve.

[ ] µg/mL	V (µL) of BSA 100 µg/mL	V (µL) of H_2O
0	0	400
1	4	396
5	20	380
10	40	360
15	60	340
20	80	320
25	100	300

The calibration curve was then prepared in a 96-well plate, in duplicates, by loading 150 µL of each solution along with 150 µL of Bradford reagent.

For protein samples, it was necessary to prepare a dilution scheme for each incubation ratio to ensure that all analysed concentrations were within the linear range of the calibration curve of 5 to 20 µg/mL. Dilution schematics for RhNHS@SBA (or RhISO@SBA) T2 and T3 samples of all 1:4, 1:2, and 1:1 incubation ratios are detailed in Table 7.3.

Table 7.3 | Dilution schematics for RhNHS@SBA (or RhISO@SBA) T2 and T3 samples of all 1:4, 1:2, and 1:1 incubation ratios, where $[\,]_{i,\,protein}$ is the maximum protein concentration available in each incubation sample, $[\,]_{dil.,\,protein}$ the aimed diluted concentration for each analysed sample, $V_{protein}$ the volume to pipette from each protein's incubation supernatant and V_{H20} the volume of H_2O to pipette.

	$[\,]_{i,\,protein}$ (µg/mL)	$[\,]_{dil.,\,protein}$ (µg/mL)	$V_{protein}$ (µL)	V_{H20} (µL)	V_T (µL)
Ratio 1:4	250	20	80	920	1000
Ratio 1:2	500	20	40	960	1000
Ratio 1:1	1000	20	20	980	1000

Table 7.3 dilutions were prepared from each supernatant (with PBS 7.4), in deionised Millipore water. Similar to the calibration curve, 150 µL of each dilution was loaded to each well and mixed with 150 µL of Bradford reagent, also in duplicates.

The blue protein-dye (Bradford reagent) complex maximum absorbance, stable to up to 60 minutes, was measured at a CLARIOstar® High Performance Monochromator Multimode Microplate Reader (BMG LABTECH), at 595 nm. Protein concentrations in each well were obtained by comparing collected absorbance data against that of the calibration curve. Through mass balance, both loaded quantity (loading %) of each protein and Rh*X*@SBA (with, *X* = NHS or ISO) loading capacity ($mg_{protein}/g_{RhX@SBA}$) were calculated.

7.4 Fluorescence Porphyrin-Based SBA-16 nanoparticles for metal sensing

Based on the same procedure used for RhNHS loading, a batch of 20 mg of SBA-16 T3 sample was dissolved in 1 mL of $CHCl_3$ and mixed with 1 mg of porphyrin (L5, FW=1198) , also dissolved in 1 mL of $CHCl_3$. The mixture was place under continuous stirring (350 rpm) for 6h, at room temperature. After the appointed time, the resulting mixture was washed in $CHCl_3$, till a clear supernatant was obtained.

Due to the non-soluble character of the L5 compound in $CHCl_3$ and consequent preference for SBA-16 particles and tendency to precipitate, a clear liquid phase was immediately obtained at either the first or second wash. Both pellet and supernatants were then isolated, with the first let to dry at air.

Excess of (precipitated) porphyrin molecules, over SBA-16 surface, were washed after subsequent resuspension of the pellet in deionised water and centrifugation at 9500 rpm. The pellet was washed till a clear supernatant was obtained (usually 3 times) and let to dry at air.

Loaded L5 quantity and SBA-16 T3 loading capacity (mg/g_{SBA}) were determined after water supernatants (total volume of 3 mL) quantification by absorption, with subsequent application of the Lambert-Beer law. Absorbance measurements were performed at the maximum peak of absorption of the first left Q-band of porphyrin spectrum, at 506 nm.

7.4.1 Metallic Ions Detection/Extraction in DI Water

The detection of metallic ions in aqueous media was done with both water washed and non-washed L5@SBA dry powder samples. Additionally, trials with RhNHS@SBA and RhISO@SBA were also performed. Nonetheless, the applied protocol was similar for all cases.

Solid-state tests herein developed focused on a scale of concentrations ranging between 10^{-2} M and 10^{-6} M, for Hg^{2+} alone, and from 10^{-4} M (50 ppm) to 10^{-5} M (5 ppm), for Hg^{2+}, Pb^{2+} and Cu^{2+} ions (Figure 7.3).

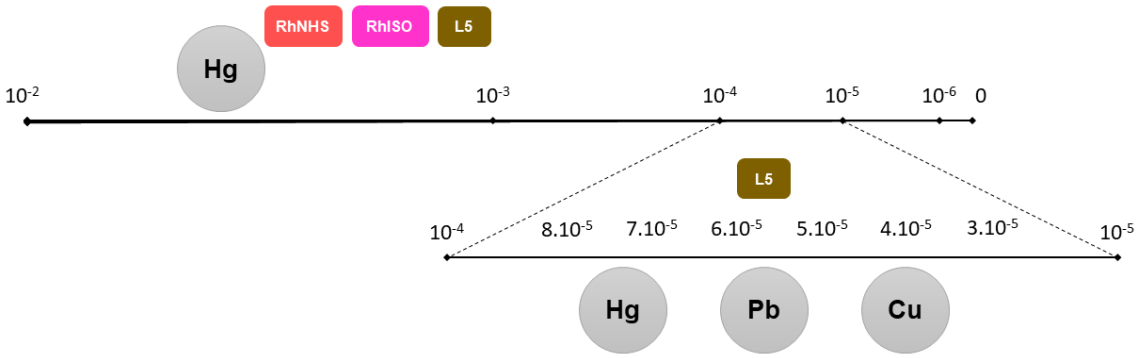

Figure 7.3 | Range of analysed concentrations (in mol/L = M) per type of ionic specie: **Hg** - Hg (II), **Pb** - Pb (II) and **Cu** - Cu (II); and doped chromophore ligand: **RhNHS**, **RhISO** and **L5**.

All metal solutions (of 3mL and 2 mL) were prepared through dilution from stock solutions with concentrations (10^{-2} and 10^{-3} M), in DI H_2O (see Table 7.4).

Table 7.4 | Weighted amount (in mg) of each metallic triflate specie according to aimed concentration and total volume of stock solutions.

	Hg^{2+} Triflate MW = 498.71 g/mol	**Pb^{2+} Triflate MW = 505.34 g/mol**	**Cu^{2+} Triflate MW = 361.68 g/mol**
10^{-2} M	15.0 mg (V_t = 3 mL)	-	-
10^{-3} M	1.0 mg (V_t = 2 mL)	1.5 mg (V_t = 3 mL)	1.0 mg 2.0 (V_t = 3 mL)

10^{-2} to 10^{-6} M dilutions were prepared exclusively from 10^{-2} M Hg^{2+} stock solution, in DI H_2O, with a total volume of 3 mL each (except 10^{-6} M dilution, for pipetting technical reasons). Pipetted volumes are detailed in Table 7.5.

Table 7.5 | Pipetted volumes for the preparation of all 10^{-2} to 10^{-6} M dilutions.

	10^{-2} M	**10^{-3} M**	**10^{-4} M**	**10^{-5} M**	**10^{-6} M**
V_{Hg2+} (µL)	3000	300	30	3	0.5
V_{H20} (µL)	0	2700	2970	2997	4999.5
V_t (µL)	3000	3000	3000	3000	5000

Concerning the elaboration of 10^{-4} to 10^{-5} M (50 – 5 ppm) dilutions, all 10^{-3} M metallic solutions were used as a starting point. For a total volume 2 mL per dilution, pipetted volumes from 10^{-3} M solutions are as displayed in Table 7.6.

Table 7.6 | Pipetted volumes ($V_{i, Metal.Sol}$), from any 10^{-3} M metallic solution (e.g. Hg^{2+}, Pb^{2+} or Cu^{2+}), for the preparation of all 10^{-5} M to 10^{-4} M (5 ppm to 50 ppm) dilutions.

[ ] (ppm)	[ ] (M = mol/L)	$V_{i, Metal.Sol}$ (µL)
0	0	-
5	10^{-5}	20
15	$3x10^{-5}$	60
20	$4x10^{-5}$	80
25	$5x10^{-5}$	100
30	$6x10^{-5}$	120
35	$7x10^{-5}$	140
40	$8x10^{-5}$	160
50	10^{-4}	200

With all dilutions prepared, the detection/extraction of Hg^{2+}, Pb^{2+} and Cu^{2+} in aqueous media was achieved by mixing 0.5 mL of each dilution with 1 mg of the corresponding dry powder sample. As shown in Figure 7.3, while for 10^{-2} to 10^{-6} M Hg^{2+} dilutions all L5@SBA (non-washed with water), RhNHS@SBA and RhISO@SBA dry powders were tested, for Hg^{2+}, Pb^{2+} and Cu^{2+} 10^{-5} to 10^{-4} M dilutions only L5@SBA (water washed) dry powder was tried.

The resulting resuspensions were left to incubate for approximately 2h, before being centrifuged (9500 rpm) and having both supernatants and pellets isolated. Pellets were let to dry at air, for 24h.

With the aid of an external optical-fibre probe, a solid-state emission quantification of all 1mg pellets was accomplished. Emission spectra were traced after samples excitation at a monochromatic light source, with its wavelength corresponding to the maximum absorption peak of the chromophore ligand: 556 / 550 nm for RhNHS@SBA pellets (2 nm slit) and 579 nm for L5@SBA samples (3 nm slit).

Reversibility tests were carried out with the aid of EDTA on the 10-2 M Hg2+ doped L5@SBA, with consequent additions of 0.5mL of 10^{-2} M, $2x10^{-2}$ and $3x10^{-3}$ M (1 eq., 2eq. and 3 eq.) EDTA solutions and pellet changes visually analysed.

7.4.2 Hg^{2+} Spikes Detection/Extraction in Urine

The performance of the above-mentioned RhNHS@SBA dry powders in biological media was tested with the aid of the introduction of known spikes of Hg^{2+} solutions on a urine sample collected from a volunteer subject, at mid-day.

The injected spikes of Hg^{2+} have a range of concentrations broadening from 10^{-2} to 10^{-5} M and its preparation was based on a diluted 1:4 urine : 10^{-2} M Hg^{2+} initial solution, with total volume of 2mL (i.e.

0.5 mL of collected Urine + 1.5 mL of a 10^{-2} M Hg^{2+} solution). All subsequent dilutions, in DI H_2O, have a total volume of 2 mL and pipetted quantities are summarised in Table 7.7.

Table 7.7 | Pipetted volumes for the preparation of all urine : Hg^{2+} 10^{-2} to 10^{-6} M dilutions

	10^{-2} M	**10^{-3} M**	**10^{-4} M**	**10^{-5} M**
$V_{Urine+Hg2+}$ (µL)	2000	200	20	2
V_{H20} (µL)	0	1800	1980	1998
V_t (µL)	2000	2000	2000	2000

Detection and extraction of Hg^{2+} ion within the already prepared urine : Hg^{2+} spiked solutions is achieved by suspending 1 mg of RhNHS@SBA dry powder in 0.5 mL of each spiked solution. The resulting mixture was incubated for 2h, at room temperature, and consequently centrifuged (9500 rpm) on a Montreal Biotech MBI Refrigerated Centrifuge, at 20 ºC. Pellets and supernatants were isolated, and the firsts dried at air.

Solid-state quantification of all pellets was made at a Horiba FluroMax-4 Spectrofluorometer, from Proteomass-Bioscope facility, with the aid of an optical-fibre probe. Samples were excited with a monochromatic radiation at 556 nm, corresponding of the maximum absorption peak of RhNHS chromophore, for a 2 nm slit.

8

General Conclusions & Future Prospects

With this work's objective in mind and reviewing the results as a whole, it is possible to succinctly affirm that the development of a proof of concept of the here in proposed device for the extraction of proteins, with the aid of an external optical NHS-based sensor, was successfully achieved.

Following a 'start from scratch' approach, the initial development of a solid-state support was made through the application of SBA-15 based synthetic pathways, from which the denominated Method 2 proposed by Katiyar *et al* confirmed to be the best approach for the development of cubic-phased mesoporous materials with relatively large porous volume, pore diameters and surface area capable of hosting proteins within its matrix. However, the employment of a set of different variables, i.e. different directing surfactants and silica precursors, resulted in smaller cavities (4-5 nm width) and specific surface areas (343 and 534 cm^2/g) than those reported in the literature. It was hypothesised that a defective template removal might be one of the sources of the issue and future improvements might fall on a more extensive template removal, or even the use of a calcination-extraction conjugated methodology, as proposed by Grudzien *et al* [109]. Notwithstanding, optimisation of the synthetic procedure is one of the future appointed works.

It was also concluded that aggregation is a current issue and a significant drawback for future pores' functionalisation and protein extraction, that must be surpassed. The addition of stabilizing agents, sucrose molecules, was proven to be a satisfactory approach, with lower concentrations favouring the formation of more stable and dispersed nanoparticles, with zeta potentials of ± 30 mV.

Pores functionalisation with RhNHS and its competing agent, RhISO, was successfully attained with loading capacities of 40 and 50 mg/g, respectively, and was proven to be pore size independent, as trials with SBA-16 T2 (d=4 nm) and T3 (d=5 nm) samples produced no significant fluctuations on the total amount of encapsulated chromophore.

Conversely, it was also concluded that the very same molecules' releasing profiles are pH dependent, with acidic conditions favouring protonation and higher percentages of release. Additionally, the existence of plateaus after the 30 minutes' mark, pointed out the importance of working around this limit

where any extra amount of released chromophore, for a fixed pH, results from an additional particle-protein interaction.

Therefore, it was established that the best conditions for protein assays fell on pH 7.4 and incubation times of 30 minutes and 2 hours, where a more sustained chromophore release is visible (release plateau of 20%) and where NHS hydrolysis is known to last approximately 30 minutes, at room temperature.

From proteins' extraction assays it was confirmed the system's capability to extract proteins from their media, with a positive crescent tendency on the amount of loaded protein, due to an increase of available initial protein quantity. A general preference for ovalbumin was also observable, with % L and extraction capacities of about 44-52% and 464-519 mg/g, respectively; in detriment of Myo and Cyt C.

The introduction of chromophores within the system resulted in a general increase of extract proteins, with a loss of selectivity for smaller doped-pores rather than larger ones, where RhNHS and RhISO introduction played no significant role. The chromophore-particle-protein interaction was hypothesised to be not only size, shape and volume dependent, but also a result of the available NH_2 groups within each protein structure. It was also concluded that the adsorption of proteins has a stabilizing effect over nanoparticles, with surface adsorption an ever-present and important factor, along with the desired pore adsorption, towards protein extraction. Additionally, an incubation time of 30 minutes showed to be the more appropriate condition when fast extracting proteins, for times above that (i.e. 2h) resulted in either destabilisation or degradation.

From this work, we can then conclude that the here in initially proposed system was successfully developed and a sustained proof of concept has so far been settle, supporting their application on novel separation / extraction techniques. Notwithstanding, a future optimizing work is needed, going from full characterisation of the system to chromophores' tracing, during protein extraction.

Extending the system's application to a more environmental field, the development of a cationic L5 porphyrin-doped solid-state optical probe for the sensing and extraction of toxic metal ions had proven to be possible, with significant colour changes when in presence of ions like Hg^{2+}, Cu^{2+} and Pb^{2+}. It was concluded that the system could successfully optically identify their presence to concentrations down to 5 ppm and that its naked-eye limit of detection was possibly located on the ppb scale. Quantification assays also confirmed its extraction capacity of about 85% and a responsiveness down to 1 ppb, below the established limit by EPA for drinkable waters.

In-urine and in-water metal sensing tests were successfully performed with RhNHS and an immediate reversion of the system was confirmed after the employment of EDTA. Notwithstanding a more developed study is needed, with a full investigation on the reusability of the system.

Therefore, these attractive results the elaboration of this facile, low cost and solid-state device might prove useful for the development of novel techniques for the *in situ* monitorisation and fast extraction of toxic metal ions from the environment.

References

[1] J.E.R. Vincent Chiola, and Clarence D. Vanderpool, PROCESS FOR PRODUCING LOW-BULK DENSITY SILICA, in: Delaware (Ed.), United States, 1971.
[2] J.S. Beck, J.C. Vartuli, W.J. Roth, M.E. Leonowicz, C.T. Kresge, K.D. Schmitt, C.T.W. Chu, D.H. Olson, E.W. Sheppard, S.B. McCullen, J.B. Higgins, J.L. Schlenker, A new family of mesoporous molecular sieves prepared with liquid crystal templates, Journal of the American Chemical Society, 114 (1992) 10834-10843.
[3] D. Zhao, Triblock Copolymer Syntheses of Mesoporous Silica with Periodic 50 to 300 Angstrom Pores, Science, 279 (1998) 548-552.
[4] D. Zhao, Y. Peidong, H. Qisheng, C. Bradley F, S. Galen D, Topological construction of mesoporous materials, Current Opinion in Solid State and Materials Science, 3 (1998) 111-121.
[5] C.G. Goltner, M. Antonietti, Mesoporous materials by templating of liquid crystalline phases, Advanced Materials, 9 (1997) 431-436.
[6] J. Siefker, P. Karande, M.O. Coppens, Packaging biological cargoes in mesoporous materials: opportunities for drug delivery, Expert opinion on drug delivery, 11 (2014) 1781-1793.
[7] Y. Feng, N. Panwar, D.J.H. Tng, S.C. Tjin, K. Wang, K.-T. Yong, The application of mesoporous silica nanoparticle family in cancer theranostics, Coordination Chemistry Reviews, 319 (2016) 86-109.
[8] T.W. Kim, Slowing, II, P.W. Chung, V.S. Lin, Ordered mesoporous polymer-silica hybrid nanoparticles as vehicles for the intracellular controlled release of macromolecules, ACS nano, 5 (2011) 360-366.
[9] L.P. Singh, S.K. Agarwal, S.K. Bhattacharyya, U. Sharma, S. Ahalawat, Preparation of Silica Nanoparticles and its Beneficial Role in Cementitious Materials, Nanomaterials and Nanotechnology, 1 (2011) 9.
[10] M. Montalti, L. Prodi, E. Rampazzo, N. Zaccheroni, Dye-doped silica nanoparticles as luminescent organized systems for nanomedicine, Chemical Society reviews, 43 (2014) 4243-4268.
[11] J.J. Fripiat, Silanol Groups and Properties of Silica Surfaces, 194 (1982) 165-184.
[12] Z. Yi, L.F. Dumee, C.J. Garvey, C. Feng, F. She, J.E. Rookes, S. Mudie, D.M. Cahill, L. Kong, A New Insight into Growth Mechanism and Kinetics of Mesoporous Silica Nanoparticles by in Situ Small Angle X-ray Scattering, Langmuir : the ACS journal of surfaces and colloids, 31 (2015) 8478-8487.
[13] X. Wang, Y. Zhang, W. Luo, A.A. Elzatahry, X. Cheng, A. Alghamdi, A.M. Abdullah, Y. Deng, D. Zhao, Synthesis of Ordered Mesoporous Silica with Tunable Morphologies and Pore Sizes via a Nonpolar Solvent-Assisted Stöber Method, Chemistry of Materials, 28 (2016) 2356-2362.
[14] D. Zhao, J. Sun, Q. Li, G.D. Stucky, Morphological Control of Highly Ordered Mesoporous Silica SBA-15, Chemistry of Materials, 12 (2000) 275-279.
[15] R. Cademartiri, M.A. Brook, R. Pelton, J.D. Brennan, Macroporous silica using a “sticky” Stöber process, Journal of Materials Chemistry, 19 (2009) 1583.
[16] A. Katiyar, S. Yadav, P.G. Smirniotis, N.G. Pinto, Synthesis of ordered large pore SBA-15 spherical particles for adsorption of biomolecules, Journal of chromatography. A, 1122 (2006) 13-20.
[17] H. Ahmad Alyosef, D. Schneider, S. Wassersleben, H. Roggendorf, M. Weiß, A. Eilert, R. Denecke, I. Hartmann, D. Enke, Meso/Macroporous Silica from Miscanthus, Cereal Remnant Pellets, and Wheat Straw, ACS Sustainable Chemistry & Engineering, 3 (2015) 2012-2021.
[18] C.T. Kresge, M.E. Leonowicz, W.J. Roth, J.C. Vartuli, J.S. Beck, Ordered mesoporous molecular sieves synthesized by a liquid-crystal template mechanism, Nature, 359 (1992) 710-712.
[19] C.-Y. Chen, S.L. Burkett, H.-X. Li, M.E. Davis, Studies on mesoporous materials II. Synthesis mechanism of MCM-41, Microporous Materials, 2 (1993) 27-34.
[20] C.-Y. Chen, H.-X. Li, M.E. Davis, Studies on mesoporous materials, Microporous Materials, 2 (1993) 17-26.
[21] J.S. Yu, Method for recycling of silica waste and method for preparing nanoporous or spherical materials, in, Google Patents, 2011.
[22] Q. Huo, D.I. Margolese, U. Ciesla, P. Feng, T.E. Gier, P. Sieger, R. Leon, P.M. Petroff, F. Schüth, G.D. Stucky, Generalized synthesis of periodic surfactant/inorganic composite materials, Nature, 368 (1994) 317-321.
[23] Y.-D. Chiang, H.-Y. Lian, S.-Y. Leo, S.-G. Wang, Y. Yamauchi, K.C.W. Wu, Controlling Particle Size and Structural Properties of Mesoporous Silica Nanoparticles Using the Taguchi Method, The Journal of Physical Chemistry C, 115 (2011) 13158-13165.

[24] Y. Wan, D. Zhao, On the controllable soft-templating approach to mesoporous silicates, Chemical reviews, 107 (2007) 2821-2860.
[25] M.V. Juliana Jorge, Gustavo Rocha de Castro, Marco Antonio Utrera Martines, Synthesis parameters for control of mesoporous silica nanoparticles (MSNs), Biointerface Research in Applied Chemistry, 6 (2016) 5.
[26] E.M. Rivera-Munoz, R. Huirache-Acuna, Sol gel-derived SBA-16 mesoporous material, International journal of molecular sciences, 11 (2010) 3069-3086.
[27] D.D. Lovingood, J.R. Owens, M. Seeber, K.G. Kornev, I. Luzinov, Controlled microwave-assisted growth of silica nanoparticles under acid catalysis, ACS applied materials & interfaces, 4 (2012) 6875-6883.
[28] J.R. Owens, D. Lovingood, Controlled microwave assisted synthesis of functionalized silica nanoparticles, in, Google Patents, 2014.
[29] G. Wanka, H. Hoffmann, W. Ulbricht, Phase Diagrams and Aggregation Behavior of Poly(oxyethylene)-Poly(oxypropylene)-Poly(oxyethylene) Triblock Copolymers in Aqueous Solutions, Macromolecules, 27 (1994) 4145-4159.
[30] R. Zana, Micellization of amphiphiles: selected aspects, Colloids and Surfaces A: Physicochemical and Engineering Aspects, 123-124 (1997) 27-35.
[31] S.M.L. dos Santos, K.A.B. Nogueira, M. de Souza Gama, J.D.F. Lima, I.J. da Silva Júnior, D.C.S. de Azevedo, Synthesis and characterization of ordered mesoporous silica (SBA-15 and SBA-16) for adsorption of biomolecules, Microporous and Mesoporous Materials, 180 (2013) 284-292.
[32] M. Mesa, L. Sierra, B. López, A. Ramirez, J.-L. Guth, Preparation of micron-sized spherical particles of mesoporous silica from a triblock copolymer surfactant, usable as a stationary phase for liquid chromatography, Solid State Sciences, 5 (2003) 1303-1308.
[33] C.-L. Lin, Y.-S. Pang, M.-C. Chao, B.-C. Chen, H.-P. Lin, C.-Y. Tang, C.-Y. Lin, Synthesis of SBA-16 and SBA-15 mesoporous silica crystals templated with neutral block copolymer surfactants, Journal of Physics and Chemistry of Solids, 69 (2008) 415-419.
[34] B. Li, F. Li, S. Bai, Z. Wang, L. Sun, Q. Yang, C. Li, Oxygen evolution from water oxidation on molecular catalysts confined in the nanocages of mesoporous silicas, Energy & Environmental Science, 5 (2012) 8229.
[35] H.-P. Boehm, The Chemistry of Silica. Solubility, Polymerization, Colloid and Surface Properties, and Biochemistry. Von R. K. Iler. John Wiley and Sons, Chichester 1979. XXIV, 886 S., geb. £ 39.50, Angewandte Chemie, 92 (1980) 328-328.
[36] M. Mesa, L. Sierra, J. Patarin, J.-L. Guth, Morphology and porosity characteristics control of SBA-16 mesoporous silica. Effect of the triblock surfactant Pluronic F127 degradation during the synthesis, Solid State Sciences, 7 (2005) 990-997.
[37] W.J. Stevens, K. Lebeau, M. Mertens, G. Van Tendeloo, P. Cool, E.F. Vansant, Investigation of the morphology of the mesoporous SBA-16 and SBA-15 materials, The journal of physical chemistry. B, 110 (2006) 9183-9187.
[38] H. Chaudhuri, S. Dash, S. Ghorai, S. Pal, A. Sarkar, SBA-16: Application for the removal of neutral, cationic, and anionic dyes from aqueous medium, Journal of Environmental Chemical Engineering, 4 (2016) 157-166.
[39] Y. Hu, Z. Zhi, Q. Zhao, C. Wu, P. Zhao, H. Jiang, T. Jiang, S. Wang, 3D cubic mesoporous silica microsphere as a carrier for poorly soluble drug carvedilol, Microporous and Mesoporous Materials, 147 (2012) 94-101.
[40] H. Sun, Q. Tang, Y. Du, X. Liu, Y. Chen, Y. Yang, Mesostructured SBA-16 with excellent hydrothermal, thermal and mechanical stabilities: modified synthesis and its catalytic application, Journal of colloid and interface science, 333 (2009) 317-323.
[41] Y. Wang, Q. Zhao, N. Han, L. Bai, J. Li, J. Liu, E. Che, L. Hu, Q. Zhang, T. Jiang, S. Wang, Mesoporous silica nanoparticles in drug delivery and biomedical applications, Nanomedicine : nanotechnology, biology, and medicine, 11 (2015) 313-327.
[42] C. Yu, B. Tian, J. Fan, G.D. Stucky, D. Zhao, Nonionic Block Copolymer Synthesis of Large-Pore Cubic Mesoporous Single Crystals by Use of Inorganic Salts, Journal of the American Chemical Society, 124 (2002) 4556-4557.
[43] F. Kleitz, T.W. Kim, R. Ryoo, Phase domain of the cubic Im3m mesoporous silica in the EO106PO70EO106-butanol-H2O system, Langmuir : the ACS journal of surfaces and colloids, 22 (2006) 440-445.
[44] M. Mesa, L. Hoyos, L. Sierra, Effect of the porosity and hydrothermal stability of SBA-16 type mesoporous silica on the characteristics of their carbon replicas, 174 (2008) 361-364.

[45] C.-F. Cheng, Y.-C. Lin, H.-H. Cheng, S.-M. Liu, H.-S. Sheu, Rapid Crystallization of High Quality Cubic Sillica SBA-16 Nanoporous Material, Chemistry Letters, 33 (2004) 262-263.
[46] Z. Cao, X. Zhang, C. Xu, A. Duan, R. Guo, Z. Zhao, Z. Wu, C. Peng, J. Li, X. Wang, Q. Meng, The Synthesis of Al-SBA-16 Materials with a Novel Method and Their Catalytic Application on Hydrogenation for FCC Diesel, Energy & Fuels, 31 (2017) 805-814.
[47] M. Naghiloo, M. Yousefpour, M.S. Nourbakhsh, Z. Taherian, Functionalization of SBA-16 silica particles for ibuprofen delivery, Journal of Sol-Gel Science and Technology, 74 (2015) 537-543.
[48] B. Nohair, P.t.H. Thao, V.T.H. Nguyen, P.Q. Tien, D.T. Phuong, L.G. Hy, S. Kaliaguine, Hybrid Periodic Mesoporous Organosilicas (PMO-SBA-16): A Support for Immobilization ofd-Amino Acid Oxidase and Glutaryl-7-amino Cephalosporanic Acid Acylase Enzymes, The Journal of Physical Chemistry C, 116 (2012) 10904-10912.
[49] Z. Li, J.C. Barnes, A. Bosoy, J.F. Stoddart, J.I. Zink, Mesoporous silica nanoparticles in biomedical applications, Chemical Society reviews, 41 (2012) 2590-2605.
[50] W.H. Li, G. Zheng, Photoactivatable fluorophores and techniques for biological imaging applications, Photochemical & photobiological sciences : Official journal of the European Photochemistry Association and the European Society for Photobiology, 11 (2012) 460-471.
[51] J.M. Rosenholm, C. Sahlgren, M. Linden, Towards multifunctional, targeted drug delivery systems using mesoporous silica nanoparticles--opportunities & challenges, Nanoscale, 2 (2010) 1870-1883.
[52] L. Wang, W. Zhao, W. Tan, Bioconjugated silica nanoparticles: Development and applications, Nano Research, 1 (2008) 99-115.
[53] J. Tu, A.L. Boyle, H. Friedrich, P.H. Bomans, J. Bussmann, N.A. Sommerdijk, W. Jiskoot, A. Kros, Mesoporous Silica Nanoparticles with Large Pores for the Encapsulation and Release of Proteins, ACS applied materials & interfaces, 8 (2016) 32211-32219.
[54] D.M. Schlipf, S.E. Rankin, B.L. Knutson, Pore-size dependent protein adsorption and protection from proteolytic hydrolysis in tailored mesoporous silica particles, ACS applied materials & interfaces, 5 (2013) 10111-10117.
[55] Y. Yuan, M.R. Oberholzer, A.M. Lenhoff, Size does matter: electrostatically determined surface coverage trends in protein and colloid adsorption, Colloids and Surfaces A: Physicochemical and Engineering Aspects, 165 (2000) 125-141.
[56] K. Kaczmarski, J.C. Bellor, Effect of particle-size distribution and particle porosity changes on mass-transfer kinetics, Acta Chromatographica, (2003) 16.
[57] C. Liu, Y. Guo, Q. Hong, C. Rao, H. Zhang, Y. Dong, L. Huang, X. Lu, N. Bao, Bovine Serum Albumin Adsorption in Mesoporous Titanium Dioxide: Pore Size and Pore Chemistry Effect, Langmuir : the ACS journal of surfaces and colloids, 32 (2016) 3995-4003.
[58] E.L. Pastor, E. Reguera-Nunez, E. Matveeva, M. Garcia-Fuentes, Pore size is a critical parameter for obtaining sustained protein release from electrochemically synthesized mesoporous silicon microparticles, PeerJ, 3 (2015) e1277.
[59] A.M. Puziy, O.I. Poddubnaya, A. Derylo-Marczewska, A.W. Marczewski, M. Blachnio, M.M. Tsyba, V.I. Sapsay, D.O. Klymchuk, Kinetics of protein adsorption by nanoporous carbons with different pore size, Adsorption, 22 (2015) 541-552.
[60] K. Rezwan, L.P. Meier, L.J. Gauckler, Lysozyme and bovine serum albumin adsorption on uncoated silica and AlOOH-coated silica particles: the influence of positively and negatively charged oxide surface coatings, Biomaterials, 26 (2005) 4351-4357.
[61] J. Ethève, P. Déjardin, Adsorption Kinetics of Lysozyme on Silica at pH 7.4: Correlation between Streaming Potential and Adsorbed Amount, Langmuir : the ACS journal of surfaces and colloids, 18 (2002) 1777-1785.
[62] P. Schuck, H. Zhao, The Role of Mass Transport Limitation and Surface Heterogeneity in the Biophysical Characterization of Macromolecular Binding Processes by SPR Biosensing, 627 (2010) 15-54.
[63] A. Kondo, J. Mihara, Comparison of Adsorption and Conformation of Hemoglobin and Myoglobin on Various Inorganic Ultrafine Particles, Journal of colloid and interface science, 177 (1996) 214-221.
[64] A. Kondo, S. Oku, K. Higashitani, Structural changes in protein molecules adsorbed on ultrafine silica particles, Journal of colloid and interface science, 143 (1991) 214-221.
[65] P. Satzer, F. Svec, G. Sekot, A. Jungbauer, Protein adsorption onto nanoparticles induces conformational changes: Particle size dependency, kinetics, and mechanisms, Engineering in life sciences, 16 (2016) 238-246.
[66] M. Lundqvist, I. Sethson, B.H. Jonsson, Protein adsorption onto silica nanoparticles: conformational changes depend on the particles' curvature and the protein stability, Langmuir : the ACS journal of surfaces and colloids, 20 (2004) 10639-10647.

[67] S.M. Ullrich, T.W. Tanton, S.A. Abdrashitova, Mercury in the Aquatic Environment: A Review of Factors Affecting Methylation, Critical Reviews in Environmental Science and Technology, 31 (2001) 241-293.
[68] G.J. Myers, P.W. Davidson, B. Weiss, Methyl mercury exposure and poisoning at Niigata, Japan, SMDJ Seychelles Medical and Dental Journal, Vol 7 (2004).
[69] M.E. Ramírez Requelme, J.F.F. Ramos, R.S. Angélica, E.S. Brabo, Assessment of Hg-contamination in soils and stream sediments in the mineral district of Nambija, Ecuadorian Amazon (example of an impacted area affected by artisanal gold mining), Applied Geochemistry, 18 (2003) 371-381.
[70] C.R. Walters, V.S. Somerset, J.J. Leaner, J.M. Nel, A review of mercury pollution in South Africa: current status, Journal of environmental science and health. Part A, Toxic/hazardous substances & environmental engineering, 46 (2011) 1129-1137.
[71] N. Steckling, S. Bose-O'Reilly, P. Pinheiro, D. Plass, D. Shoko, G. Drasch, L. Bernaudat, U. Siebert, C. Hornberg, The burden of chronic mercury intoxication in artisanal small-scale gold mining in Zimbabwe: data availability and preliminary estimates, Environmental health : a global access science source, 13 (2014) 111.
[72] I. Erni, G. Geier, Kinetics of Extremely Fast Ligand Exchange Reactions with Methylmercury(II)-complexes of 1-Methylpyridine-2-thione and 1-Methyl-quinaldine-4-thione: Rate-Equilibria Correlations, Helvetica Chimica Acta, 62 (1979) 1007-1015.
[73] G. Liu, Y. Cai, N. O'Driscoll, ENVIRONMENTAL CHEMISTRY AND TOXICOLOGY OF MERCURY, JOHN WILEY & SONS, INC., New Jersey, 2012.
[74] U.S.G. Survey, Mercury in U.S. Coal—Abundance, Distribution, and Modes of Occurrence, in: U.S.D.o.t. Interior, U.S.G. Survey (Eds.), U.S. Geological Survey, 2001.
[75] L.E. Kerper, N. Ballatori, T.W. Clarkson, Methylmercury transport across the blood-brain barrier by an amino acid carrier., American Journal of Physiology, (1992).
[76] A.L. Choi, P. Weihe, E. Budtz-Jorgensen, P.J. Jorgensen, J.T. Salonen, T.P. Tuomainen, K. Murata, H.P. Nielsen, M.S. Petersen, J. Askham, P. Grandjean, Methylmercury exposure and adverse cardiovascular effects in Faroese whaling men, Environmental health perspectives, 117 (2009) 367-372.
[77] E. Guallar, M.I. Sanz-Gallardo, P. van't Veer, P. Bode, A. Aro, J. Gomez-Aracena, J.D. Kark, R.A. Riemersma, J.M. Martin-Moreno, F.J. Kok, M. Heavy, G. Myocardial Infarction Study, Mercury, fish oils, and the risk of myocardial infarction, The New England journal of medicine, 347 (2002) 1747-1754.
[78] P. Hultman, H. Hansson-Georgiadis, Methyl mercury-induced autoimmunity in mice, Toxicology and applied pharmacology, 154 (1999) 203-211.
[79] W. Huang, C. Song, C. He, G. Lv, X. Hu, X. Zhu, C. Duan, Recognition preference of rhodamine-thiospirolactams for mercury(II) in aqueous solution, Inorganic chemistry, 48 (2009) 5061-5072.
[80] A. Apilux, W. Siangproh, N. Praphairaksit, O. Chailapakul, Simple and rapid colorimetric detection of Hg(II) by a paper-based device using silver nanoplates, Talanta, 97 (2012) 388-394.
[81] T. Ye, C. He, Y. Qu, Z. Deng, Y. Jiang, M. Li, X. Chen, A simple colorimetric device for rapid detection of Hg2+ in water, The Analyst, 137 (2012) 4131-4134.
[82] K. Bera, A.K. Das, M. Nag, S. Basak, Development of a rhodamine-rhodanine-based fluorescent mercury sensor and its use to monitor real-time uptake and distribution of inorganic mercury in live zebrafish larvae, Analytical chemistry, 86 (2014) 2740-2746.
[83] G.H. Chen, W.Y. Chen, Y.C. Yen, C.W. Wang, H.T. Chang, C.F. Chen, Detection of mercury(II) ions using colorimetric gold nanoparticles on paper-based analytical devices, Analytical chemistry, 86 (2014) 6843-6849.
[84] Y. Ding, Y. Tang, W. Zhu, Y. Xie, Fluorescent and colorimetric ion probes based on conjugated oligopyrroles, Chemical Society reviews, 44 (2015) 1101-1112.
[85] Z. Wang, M. Yang, C. Chen, L. Zhang, H. Zeng, Selectable Ultrasensitive Detection of Hg(2+) with Rhodamine 6G-Modified Nanoporous Gold Optical Sensor, Scientific reports, 6 (2016) 29611.
[86] Y. Jiao, L. Zhang, P. Zhou, A rhodamine B-based fluorescent sensor toward highly selective mercury (II) ions detection, Talanta, 150 (2016) 14-19.
[87] W.H. Organization, Guidelines for Drinking-water Quality - Mercury in Drinking-water, in: W.H. Organization (Ed.) WHO/SDE/WSH/05.08/10, 2005.
[88] EPA, Mercury Compounds, in: U.S.E.P. Agency (Ed.), United States Environmental Protection Agency, 2016.
[89] M. De la Cruz-Guzman, A. Aguilar-Aguilar, L. Hernandez-Adame, A. Banuelos-Frias, F.J. Medellin-Rodriguez, G. Palestino, A turn-on fluorescent solid-sensor for Hg(II) detection, Nanoscale research letters, 9 (2014) 431.

[90] X. Liu, X. Liu, M. Tao, W. Zhang, A highly selective and sensitive recyclable colorimetric Hg2+ sensor based on the porphyrin-functionalized polyacrylonitrile fiber, J. Mater. Chem. A, 3 (2015) 13254-13262.
[91] L. Sun, Y. Li, M. Sun, H. Wang, S. Xu, C. Zhang, Q. Yang, Porphyrin-functionalized Fe3O4@SiO2 core/shell magnetic colorimetric material for detection, adsorption and removal of Hg2+ in aqueous solution, New Journal of Chemistry, 35 (2011) 2697.
[92] L.L. Hench, J.K. West, The sol-gel process, Chemical reviews, 90 (1990) 33-72.
[93] C.J. Brinker, G.W. Scherer, CHAPTER 1 - Introduction, in: Sol-Gel Science, Academic Press, San Diego, 1990, pp. xvi-18.
[94] C.J. Brinker, G.W. Scherer, CHAPTER 2 - Hydrolysis and Condensation I: Nonsilicates, in: Sol-Gel Science, Academic Press, San Diego, 1990, pp. 20-95.
[95] C.J. Brinker, G.W. Scherer, CHAPTER 3 - Hydrolysis and Condensation II: Silicates, in: Sol-Gel Science, Academic Press, San Diego, 1990, pp. 96-233.
[96] C.J. Brinker, G.W. Scherer, CHAPTER 4 - Particulate Sols and Gels, in: Sol-Gel Science, Academic Press, San Diego, 1990, pp. 234-301.
[97] C.J. Brinker, G.W. Scherer, CHAPTER 5 - Gelation, in: Sol-Gel Science, Academic Press, San Diego, 1990, pp. 302-355.
[98] C.J. Brinker, G.W. Scherer, CHAPTER 6 - Aging of Gels, in: Sol-Gel Science, Academic Press, San Diego, 1990, pp. 356-405.
[99] C.J. Brinker, G.W. Scherer, CHAPTER 7 - Theory of Deformation and Flow in Gels, in: Sol-Gel Science, Academic Press, San Diego, 1990, pp. 406-451.
[100] C.J. Brinker, G.W. Scherer, CHAPTER 8 - Drying, in: Sol-Gel Science, Academic Press, San Diego, 1990, pp. 452-513.
[101] C.J. Brinker, G.W. Scherer, CHAPTER 9 - Structural Evolution during Consolidation, in: Sol-Gel Science, Academic Press, San Diego, 1990, pp. 514-615.
[102] C.J. Brinker, G.W. Scherer, CHAPTER 10 - Surface Chemistry and Chemical Modification, in: Sol-Gel Science, Academic Press, San Diego, 1990, pp. 616-672.
[103] C.J. Brinker, G.W. Scherer, CHAPTER 11 - Sintering, in: Sol-Gel Science, Academic Press, San Diego, 1990, pp. 674-742.
[104] C.J. Brinker, G.W. Scherer, CHAPTER 12 - Comparison of Gel-derived and Conventional Ceramics, in: Sol-Gel Science, Academic Press, San Diego, 1990, pp. 744-785.
[105] C.J. Brinker, G.W. Scherer, CHAPTER 13 - Film Formation, in: Sol-Gel Science, Academic Press, San Diego, 1990, pp. 786-837.
[106] C.J. Brinker, G.W. Scherer, CHAPTER 14 - Applications, in: Sol-Gel Science, Academic Press, San Diego, 1990, pp. 838-880.
[107] A.S.d.S.d. Almeida, Síntese de sílicas mesoporosas contendo nanopartículas de TiO2 e adsorção de bases quinoidais, in: Inorganic chemistry, Faculty of Sciences and Technology of NOVA University of Lisbon, 2011.
[108] Copyright A2 - Brinker, C. Jeffrey, in: G.W. Scherer (Ed.) Sol-Gel Science, Academic Press, San Diego, 1990, pp. iv.
[109] R.M. Grudzien, B.E. Grabicka, M. Jaroniec, Effective method for removal of polymeric template from SBA-16 silica combining extraction and temperature-controlled calcination, J. Mater. Chem., 16 (2006) 819-823.
[110] K. Byrappa, T. Adschiri, Hydrothermal technology for nanotechnology, Progress in Crystal Growth and Characterization of Materials, 53 (2007) 117-166.
[111] M. Birkholz, Principles of X-ray Diffraction, in: W.-V.V.G. Co (Ed.) Thin Film Analysis by X-Ray Scattering, 2006.
[112] D.B. Williams, The Transmission Electron Microscope, in: S.S.B. Media (Ed.) Transmission Electron Microscopy, New York, 1996.
[113] J. Goldstein, D.E. Newbury, P. Echlin, D.C. Joy, A.D. Romig Jr., C.E. Lyman, C. Fiori, E. Lifshin, Scanning Electron Microscopy and X-Ray Microanalysis: A Text for Biologists, Materials Scientists, and Geologists, Springer Science & Business Media, 2012.
[114] M.I. Limited, ZETASIZER NANO Series PERFORMANCE, SIMPLICITY, VERSATILITY, in, 2017.
[115] Introduction to NMR spectroscopy, in, Royal Society of Chemistry 2013, 2016.
[116] Nuclear Magnetic Resonance Spectroscopy Theoretical Principles, in, Sheffield Hallam University, 2015.
[117] S. Brunauer, P.H. Emmett, E. Teller, Adsorption of Gases in Multimolecular Layers, Journal of the American Chemical Society, 60 (1938) 309-319.

[118] E.P. Barrett, L.G. Joyner, P.P. Halenda, The Determination of Pore Volume and Area Distributions in Porous Substances. I. Computations from Nitrogen Isotherms, Journal of the American Chemical Society, 73 (1951) 373-380.
[119] G. Pirngruber, Characterization of porous solids - Characterization of Catalysts and Surfaces: Physisorption and pore size analysis, in, Innovation Energie Environnement, Innovation Energie Environnement 2016.
[120] K.S.W. Sing, R.T. Williams, Physisorption Hysteresis Loops and the Characterization of Nanoporous Materials, Adsorption Science & Technology, 22 (2016) 773-782.
[121] M.M. Bradford, A rapid and sensitive method for the quantitation of microgram quantities of protein utilizing the principle of protein-dye binding, Analytical Biochemistry, 72 (1976) 248-254.
[122] S.R. Gallagher, One-dimensional SDS gel electrophoresis of proteins, Current protocols in cell biology, Chapter 6 (2007) Unit 6 1.
[123] S.R. Gallagher, One-dimensional SDS gel electrophoresis of proteins, Current protocols in molecular biology, Chapter 10 (2006) Unit 10 12A.
[124] B.J. Smith, SDS polyacrylamide gel electrophoresis of proteins, Methods in molecular biology, 32 (1994) 23-34.
[125] C. Proteomics, 1D SDS-PAGE, IEF, in, 2017.
[126] Y. Wei, R. Laurent, J.-P. Majoral, A.-M. Caminade, Synthesis and characterization of phosphorus-containing dendrimers bearing rhodamine derivatives as terminal groups, Arkivoc, 2010 (2010) 318.
[127] H. Mojarradi, Coupling of substances containing a primary amine to hyaluronan via carbodiimide-mediated amidation, in: Department of Biochemistry and Organic Chemistry, Uppsala University, 2010, pp. 44.
[128] E. Valeur, M. Bradley, Amide bond formation: beyond the myth of coupling reagents, Chemical Society reviews, 38 (2009) 606-631.
[129] S. Honary, F. Zahir, Effect of Zeta Potential on the Properties of Nano-Drug Delivery Systems - A Review (Part 2), Tropical Journal of Pharmaceutical Research, 12 (2013).
[130] T. Benamor, L. Vidal, B. Lebeau, C. Marichal, Influence of synthesis parameters on the physico-chemical characteristics of SBA-15 type ordered mesoporous silica, Microporous and Mesoporous Materials, 153 (2012) 100-114.
[131] M. Kruk, M. Jaroniec, S.H. Joo, R. Ryoo, Characterization of Regular and Plugged SBA-15 Silicas by Using Adsorption and Inverse Carbon Replication and Explanation of the Plug Formation Mechanism, The Journal of Physical Chemistry B, 107 (2003) 2205-2213.
[132] J.P. Thielemann, F. Girgsdies, R. Schlogl, C. Hess, Pore structure and surface area of silica SBA-15: influence of washing and scale-up, Beilstein journal of nanotechnology, 2 (2011) 110-118.
[133] N. Lang, A. Tuel, A Fast and Efficient Ion-Exchange Procedure To Remove Surfactant Molecules from MCM-41 Materials, Chemistry of Materials, 16 (2004) 1961-1966.
[134] B. Karolewicz, M. Gajda, J. Pluta, A. Górniak, The effect of Pluronic F127 on the physicochemical properties and dissolution profile of lovastatin solid dispersions, Journal of Thermal Analysis and Calorimetry, 123 (2015) 2283-2290.
[135] M. Zhang, Y. Wu, X. Feng, X. He, L. Chen, Y. Zhang, Fabrication of mesoporous silica-coated CNTs and application in size-selective protein separation, Journal of Materials Chemistry, 20 (2010) 5835.
[136] M. Niculaua, B.I. Cioroiu, A.M. Tomoiaga, M.E. Cioroiu, M.I. Lazar, ASSESSMENT OF SBA-16 ADSORPTION CAPACITY TOWARDS ACTIVE SUBSTANCES WITH DIFFERENT CHEMICAL STRUCTURES, Cellulose Chem. Technol., 51 (2017) 11.
[137] M. Espanol, G. Mestres, T. Luxbacher, J.B. Dory, M.P. Ginebra, Impact of Porosity and Electrolyte Composition on the Surface Charge of Hydroxyapatite Biomaterials, ACS applied materials & interfaces, 8 (2016) 908-917.
[138] Y.K. Bae, O.H. Han, Removal of copolymer template from SBA-15 studied by 1H MAS NMR, Microporous and Mesoporous Materials, 106 (2007) 304-307.
[139] L. Qin, ELUCIDATION OF THE FORMATION OF CUBIC MESOPOROUS SILICAS, in: Chemical School, The University of Manchester, The University of Manchester, 2013.
[140] M.A. Rida, F. Harb, Synthesis and Characterization of Amorphous Silica Nanoparitcles from Aqueous Silicates Uisng Cationic Surfactants, Journal of Metals, Materials and Minerals, Vol.24 (2014) pp.37-42.
[141] G.-M. Gao, H.-F. Zou, D.-R. Liu, L.-N. Miao, G.-J. Ji, S.-C. Gan, Influence of surfactant surface coverage and aging time on physical properties of silica nanoparticles, Colloids and Surfaces A: Physicochemical and Engineering Aspects, 350 (2009) 33-37.

[142] S. Srinivasachari, Y. Liu, G. Zhang, L. Prevette, T.M. Reineke, Trehalose click polymers inhibit nanoparticle aggregation and promote pDNA delivery in serum, J Am Chem Soc, 128 (2006) 8176-8184.
[143] J. Zhou, K.W. Jayawardana, N. Kong, Y. Ren, N. Hao, M. Yan, O. Ramström, Trehalose-Conjugated, Photofunctionalized Mesoporous Silica Nanoparticles for Efficient Delivery of Isoniazid into Mycobacteria, ACS Biomaterials Science & Engineering, 1 (2015) 1250-1255.
[144] A. Sizovs, L. Xue, Z.P. Tolstyka, N.P. Ingle, Y. Wu, M. Cortez, T.M. Reineke, Poly(trehalose): sugar-coated nanocomplexes promote stabilization and effective polyplex-mediated siRNA delivery, J Am Chem Soc, 135 (2013) 15417-15424.
[145] H.P. Lundgren, C.H. Binkley, Application of rhodamine-B to interaction studies in proteins and simple model systems, Journal of Polymer Science, 14 (1954) 139-158.
[146] I. Moreno-Villoslada, M. Jofre, V. Miranda, R. Gonzalez, T. Sotelo, S. Hess, B.L. Rivas, pH dependence of the interaction between rhodamine B and the water-soluble poly(sodium 4-styrenesulfonate), The journal of physical chemistry. B, 110 (2006) 11809-11812.
[147] I. AAT Bioquest, Classic Reactive Fluorescent Labeling Dyes & Their Applications in: I. AAT Bioquest (Ed.) Product Technical Information Sheet CA, February 2010
[148] P. Xu, E.A. Van Kirk, Y. Zhan, W.J. Murdoch, M. Radosz, Y. Shen, Targeted charge-reversal nanoparticles for nuclear drug delivery, Angew Chem Int Ed Engl, 46 (2007) 4999-5002.
[149] Y. Wang, Y. Yan, J. Cui, L. Hosta-Rigau, J.K. Heath, E.C. Nice, F. Caruso, Encapsulation of water-insoluble drugs in polymer capsules prepared using mesoporous silica templates for intracellular drug delivery, Adv Mater, 22 (2010) 4293-4297.
[150] X. Huang, N.P. Young, H.E. Townley, Characterization and Comparison of Mesoporous Silica Particles for Optimized Drug Delivery, Nanomaterials and Nanotechnology, (2014).
[151] L. Bergman, Influence of surface functionalization on the behavior of silica nanoparticles in biological systems, in: Department of Chemical Engineering, Åbo Akademi University, Åbo, Finland, 2014.
[152] Z. Chen, Z. Li, Y. Lin, M. Yin, J. Ren, X. Qu, Biomineralization inspired surface engineering of nanocarriers for pH-responsive, targeted drug delivery, Biomaterials, 34 (2013) 1364-1371.
[153] Y. Zhang, C. Fu, Y. Li, K. Wang, X. Wang, Y. Wei, L. Tao, Synthesis of an injectable, self-healable and dual responsive hydrogel for drug delivery and 3D cell cultivation, Polym. Chem., 8 (2017) 537-544.
[154] G. Wang, Sillica Nanoporous Materials Adsorption and Release Study, in: Chemistry, Syracuse University, College of Arts and Sciences, 2012.
[155] T. Hashimoto, Y.-K. Choe, H. Nakano, K. Hirao, Theoretical Study of the Q and B Bands of Free-Base, Magnesium, and Zinc Porphyrins, and Their Derivatives, The Journal of Physical Chemistry A, 103 (1999) 1894-1904.
[156] Sigma-Aldrich, Cytochrome C, in: Sig,a-Aldrich Enzyme Explorer, 2017.
[157] Y. Chen, V. Lykourinou, T. Hoang, L.J. Ming, S. Ma, Size-selective biocatalysis of myoglobin immobilized into a mesoporous metal-organic framework with hierarchical pore sizes, Inorganic chemistry, 51 (2012) 9156-9158.
[158] H.P. Erickson, Size and shape of protein molecules at the nanometer level determined by sedimentation, gel filtration, and electron microscopy, Biological procedures online, 11 (2009) 32-51.
[159] T.L. Bucholz, M.K. Hulvey, J.P. Reardon, B.M. Rambo, D.C. Pulvirenti, L.E. Weber, A. Zaks, Development of an Organosilica Coating Containing Carbonic Anhydrase for Applications in CO2 Capture, in: Novel Materials for Carbon Dioxide Mitigation Technology, Elsevier, 2015, pp. 117-147.
[160] B. Bhandari, Food Materials Science and Engineering, Wiley-Blackwell, 2012.
[161] UniProt, UniProtKB results, in, 2017.
[162] Q.A. Best, R. Xu, M.E. McCarroll, L. Wang, D.J. Dyer, Design and investigation of a series of rhodamine-based fluorescent probes for optical measurements of pH, Organic letters, 12 (2010) 3219-3221.
[163] P. Cui, X. Jiang, J. Sun, Q. Zhang, F. Gao, A water-soluble rhodamine B-derived fluorescent probe for pH monitoring and imaging in acidic regions, Methods and applications in fluorescence, 5 (2017) 024009.

Annex I

All synthesised SBA-16 particles IR spectra are shown below, with (a) indicating templated and (b) non-templated samples.

SBA-16 M0 particles

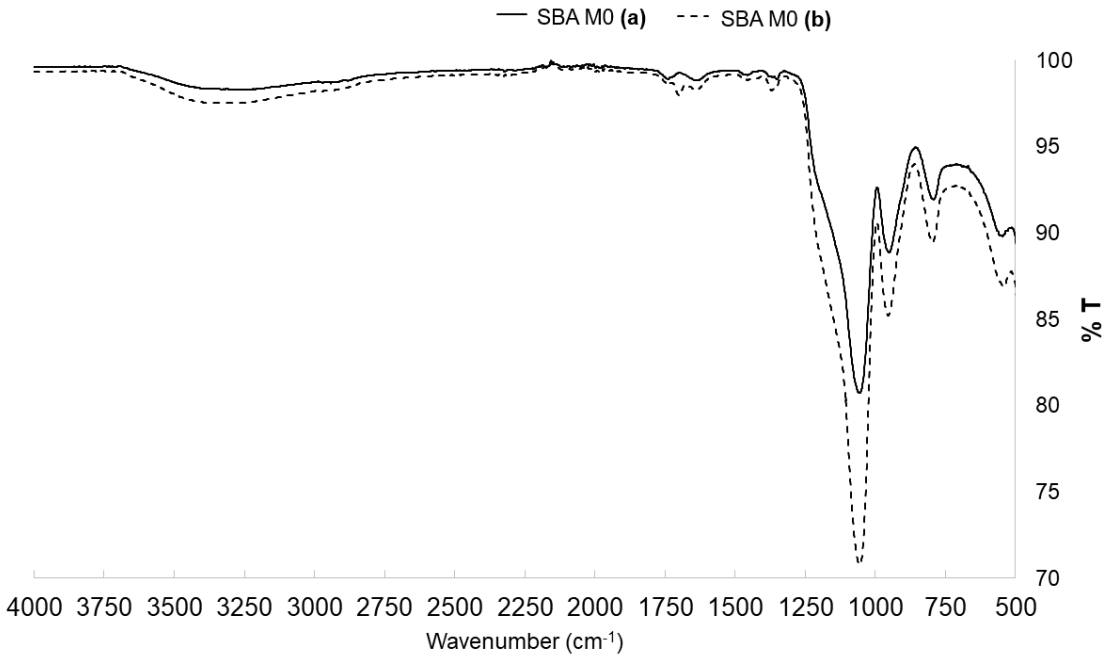

SBA-16 M1 particles

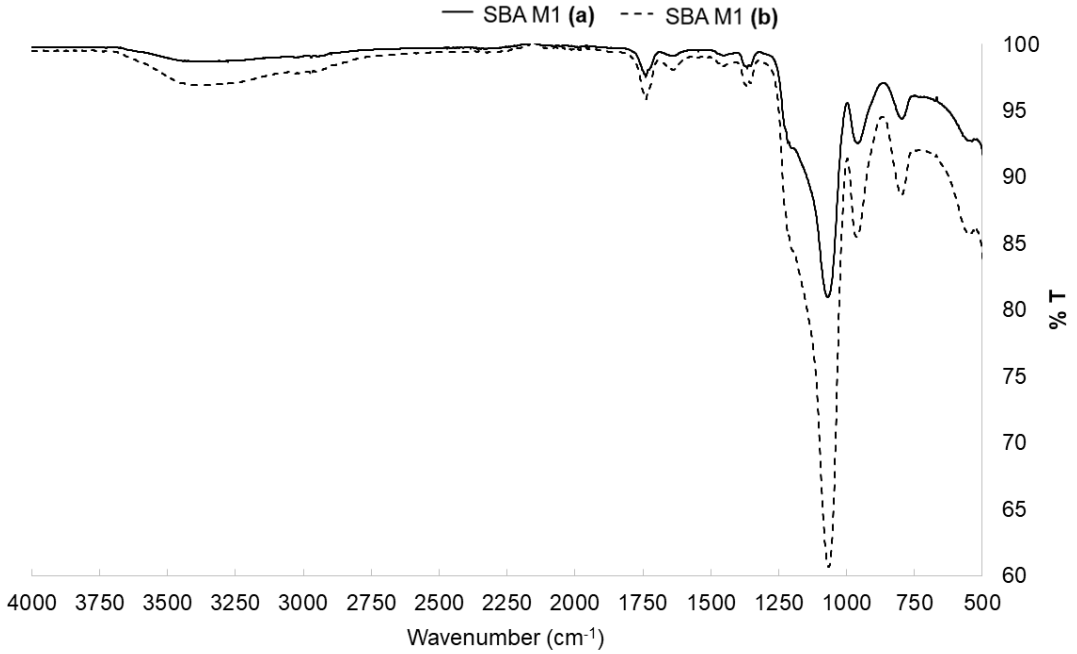

SBA-16 M2 T2 particles

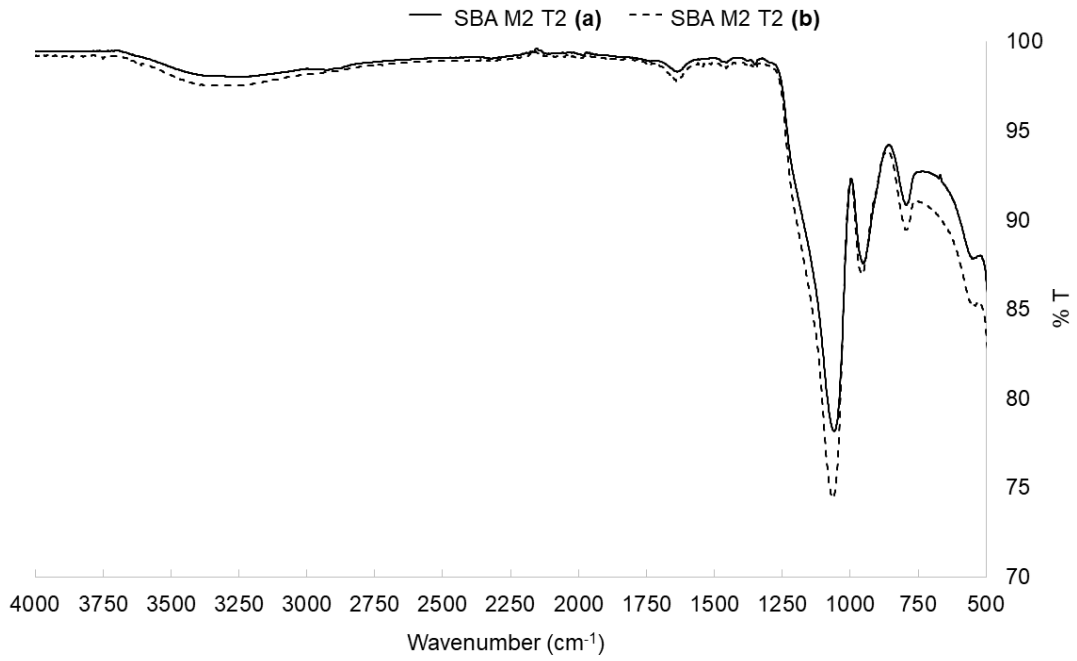

SBA-16 M2 T3 particles

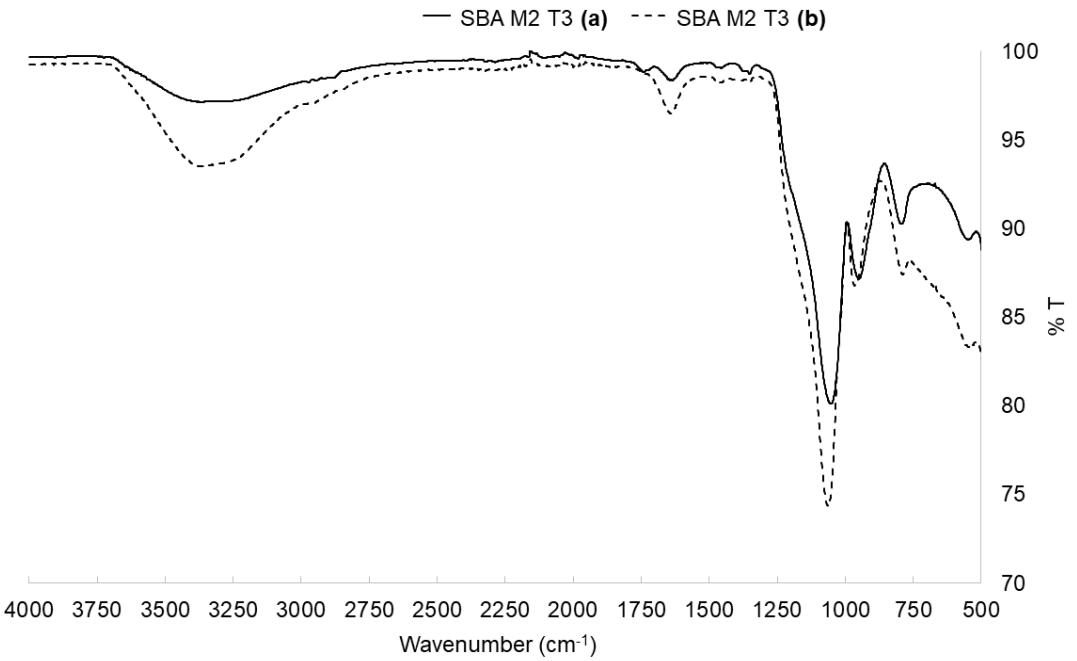

SBA-16 M2 T4 particles

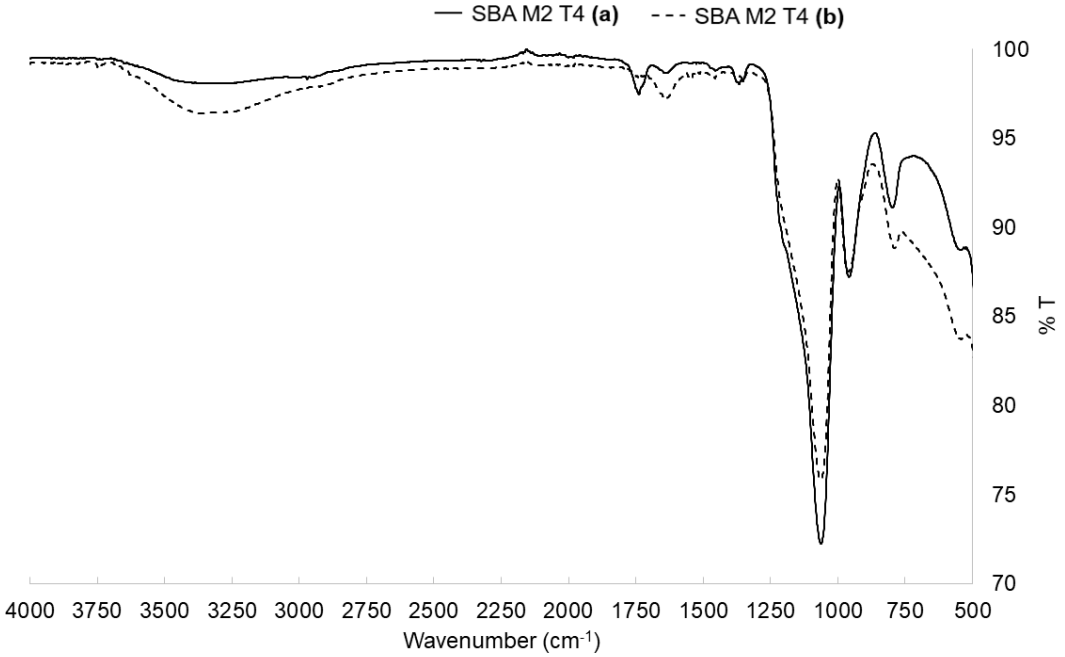

SBA-16 M2 T5 particles

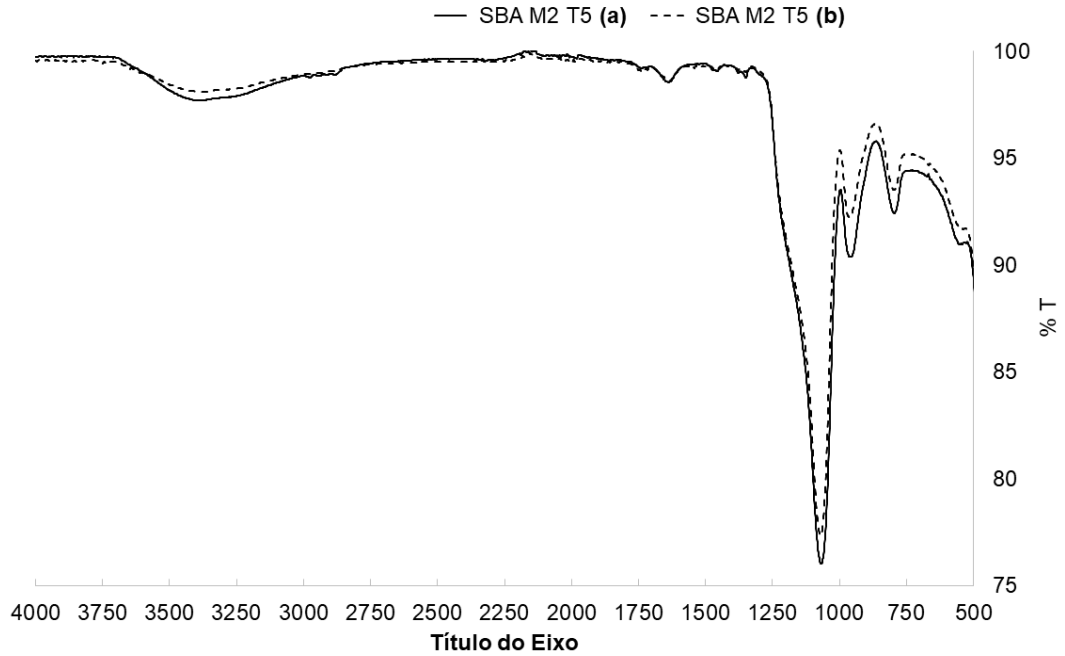

Annex II

SBA-16 M2 T1 sample N_2 isotherm (**A**) and pore size distribution (**B**) – adsorption and (**C**) - desorption:

(A)

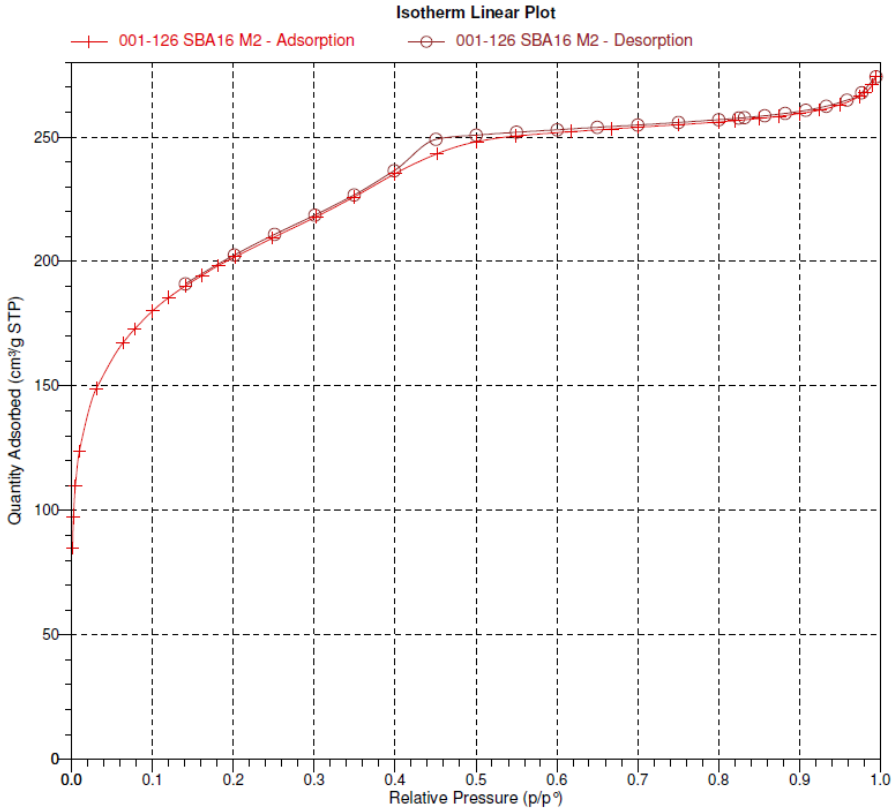

(B)

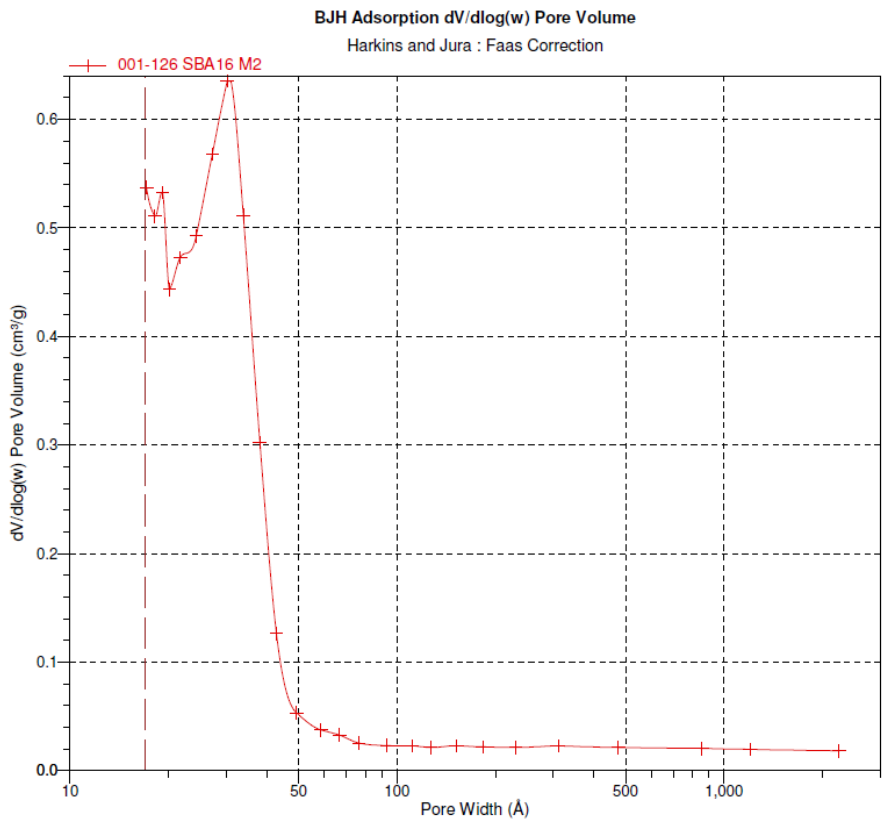

(C)

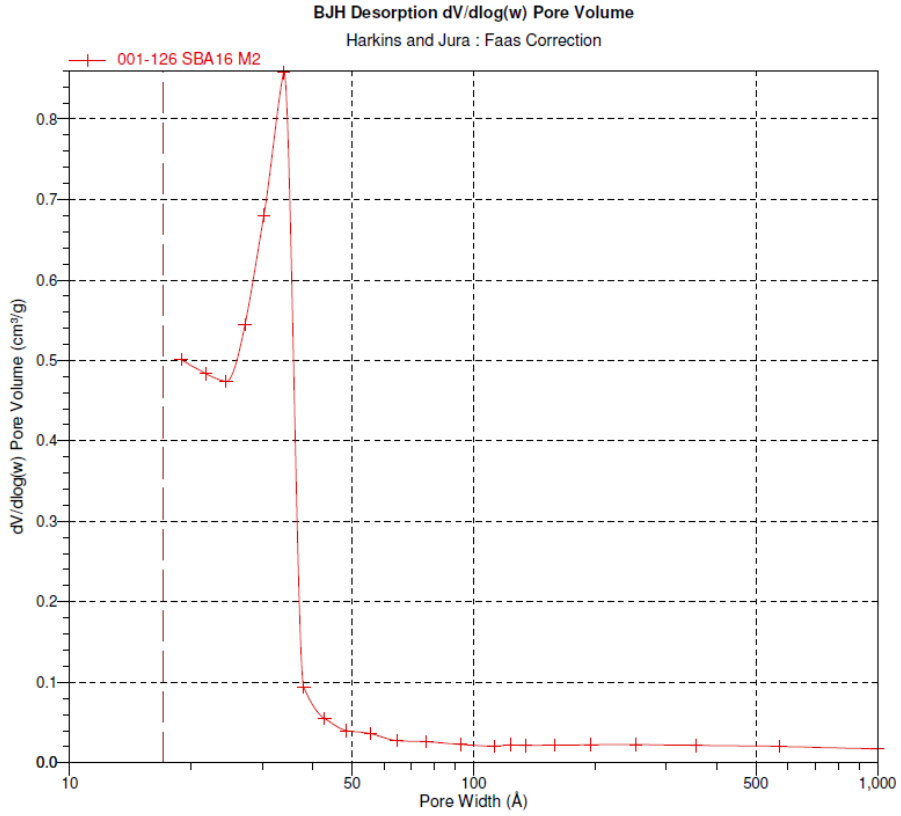

SBA-16 M2 T2 sample N_2 isotherm (**D**) and pore size distribution (**E**) – adsorption and (**F**) - desorption:

(D)

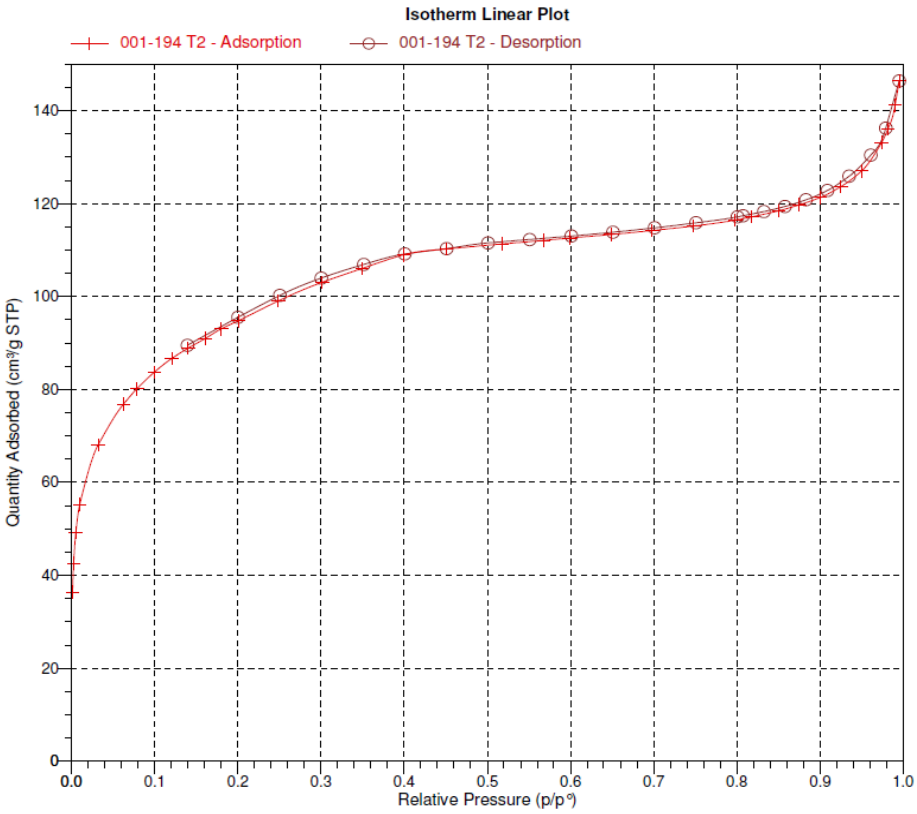

(E)

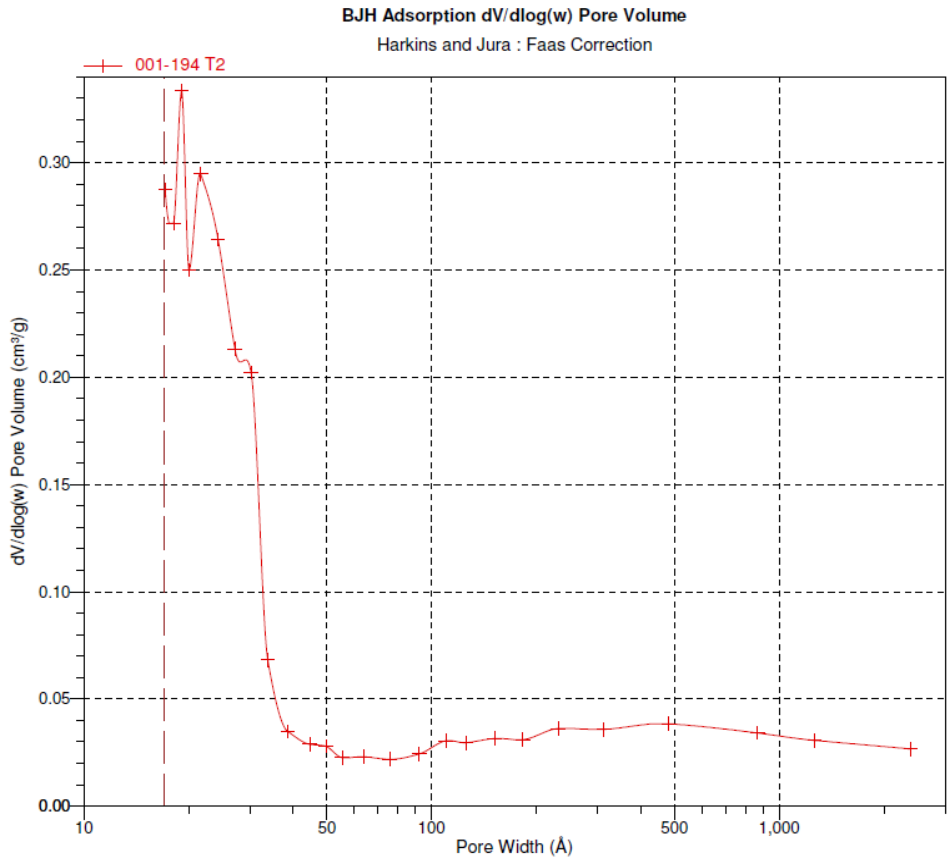
BJH Adsorption dV/dlog(w) Pore Volume
Harkins and Jura : Faas Correction
001-194 T2
dV/dlog(w) Pore Volume (cm³/g)
0.30
0.25
0.20
0.15
0.10
0.05
0.00
10
50
100
500
1,000
Pore Width (Å)

(F)

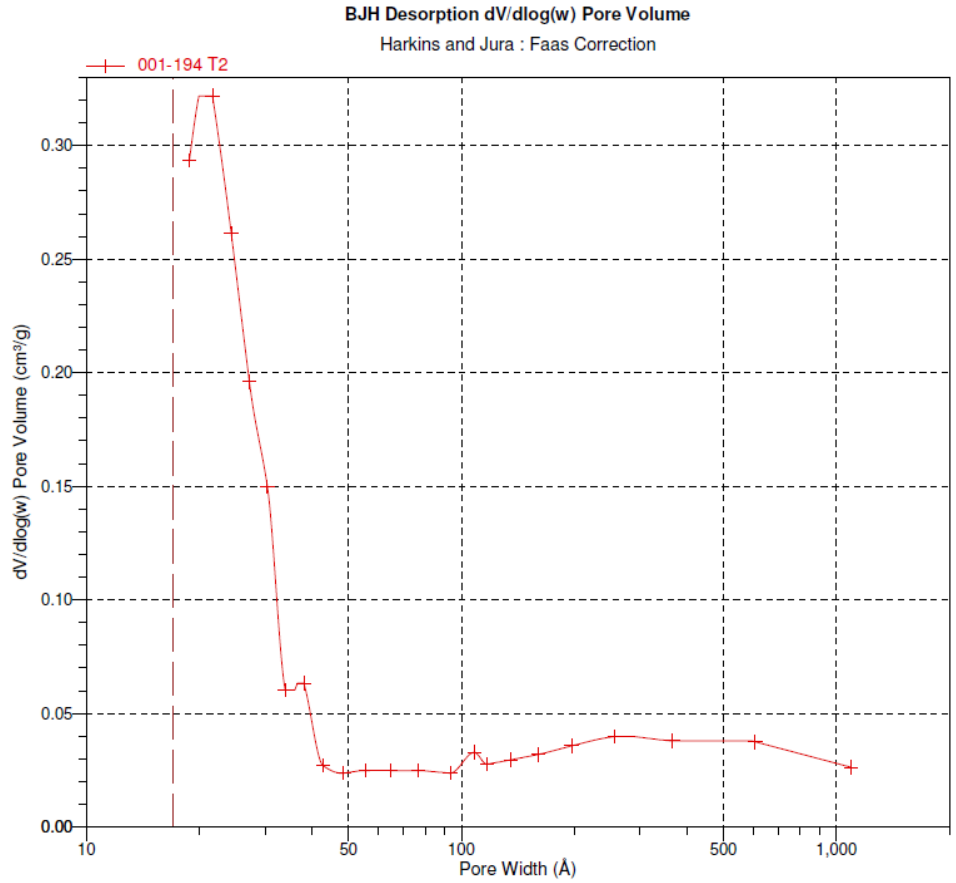
BJH Desorption dV/dlog(w) Pore Volume
Harkins and Jura : Faas Correction
001-194 T2
dV/dlog(w) Pore Volume (cm³/g)
0.30
0.25
0.20
0.15
0.10
0.05
0.00
10
50
100
500
1,000
Pore Width (Å)

SBA-16 M2 T3 sample N_2 isotherm (**G**) and pore size distribution (**H**) – adsorption and (**I**) - desorption:

(G)

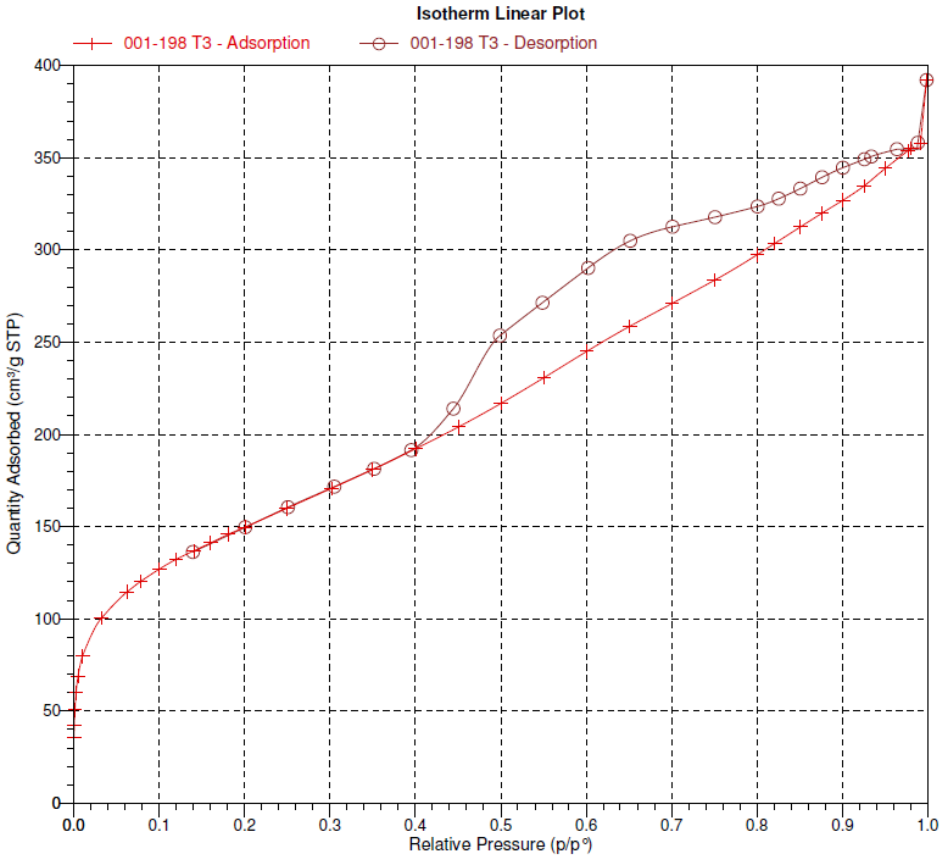

(H)

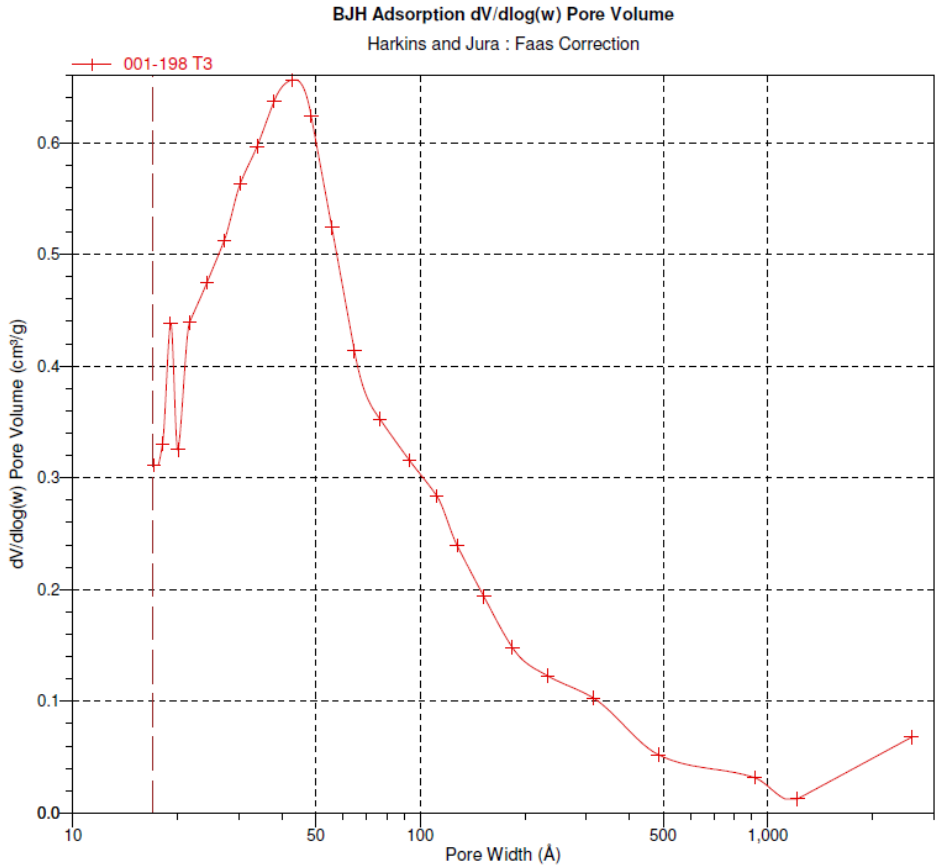

(I)

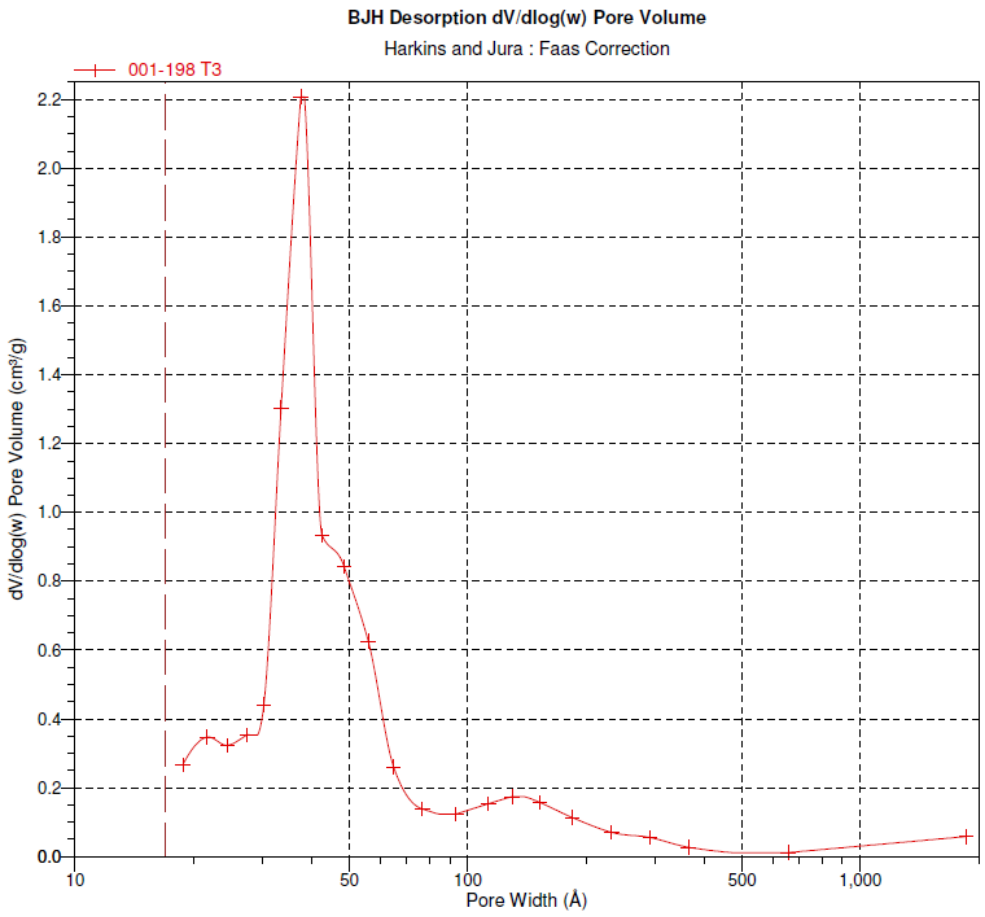
BJH Desorption dV/dlog(w) Pore Volume
Harkins and Jura : Faas Correction
001-198 T3
dV/dlog(w) Pore Volume (cm³/g)
Pore Width (Å)
2.2
2.0
1.8
1.6
1.4
1.2
1.0
0.8
0.6
0.4
0.2
0.0
10
50
100
500
1,000

Annex III

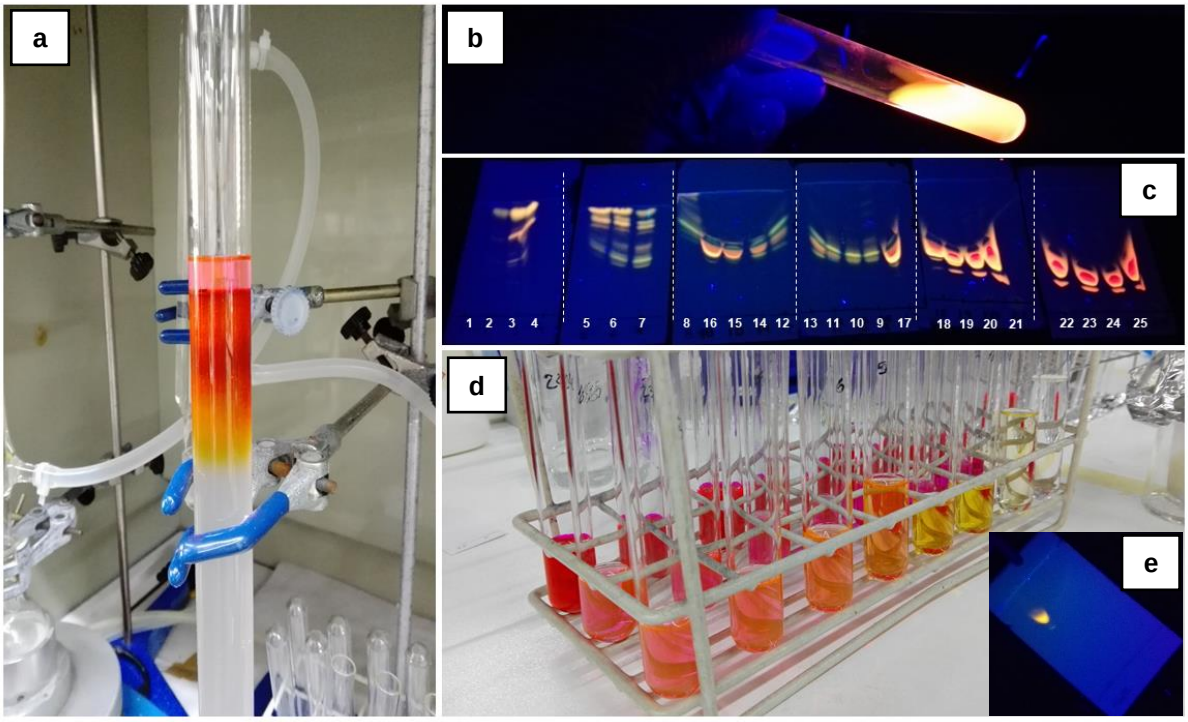

Figure AIII.1 | Silica bed chromatography (a) column and recovered fractions under (b) UV 365 nm lamp and (d) visible light. Corresponding TLC plaques to (c) during-chromatography fractions, with respective numbering (under UV lamp), and to (e) final recovered product, after evaporation to dryness.

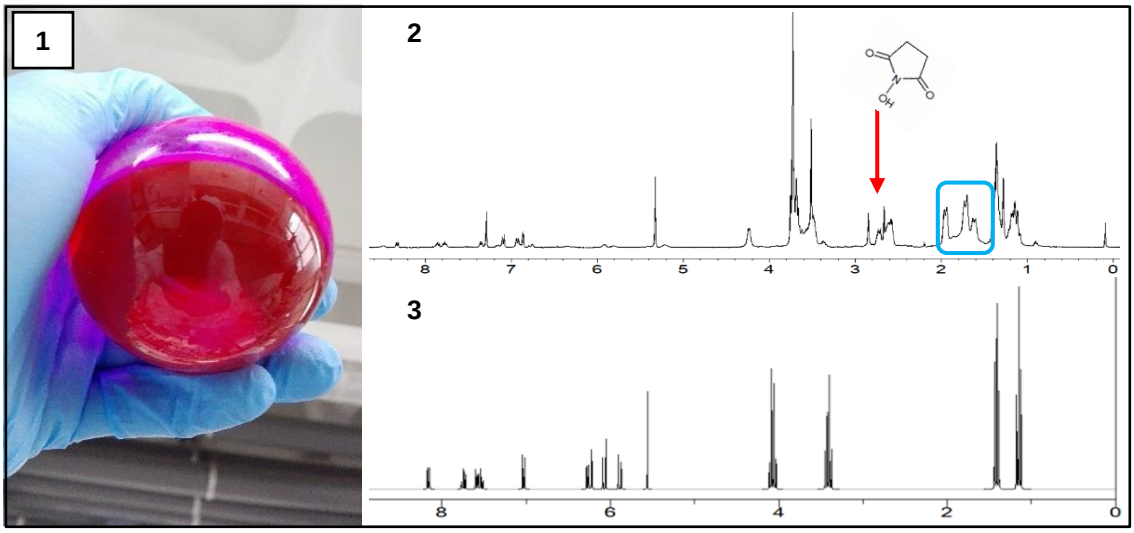

Figure AIII.2 | (1) Pre-washed RhNHS product with DCU salt impurity. Comparison between (2) experimental and (3) theoretical ^{1}H NMR spectra, with NHS peak highlighted, in red, and DCU interfering peaks, in blue.

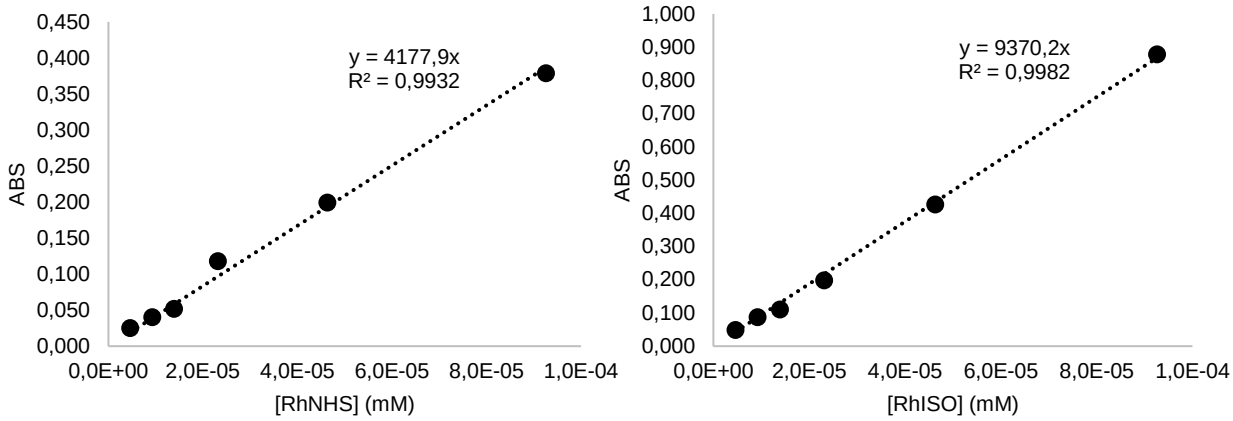

Figure AIII.3 | (Left) RhNHS and **(Right)** RhISO calibration curves in $CHCl_3$, for l = 1mm.

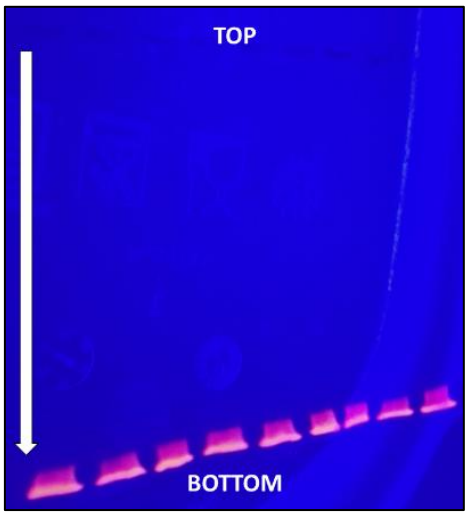

Figure AIII.4 | Under UV photo of an 1D-PAGE electrophoresis gel with RhB-based chromophore fluorescently highlighted.

Annex IV

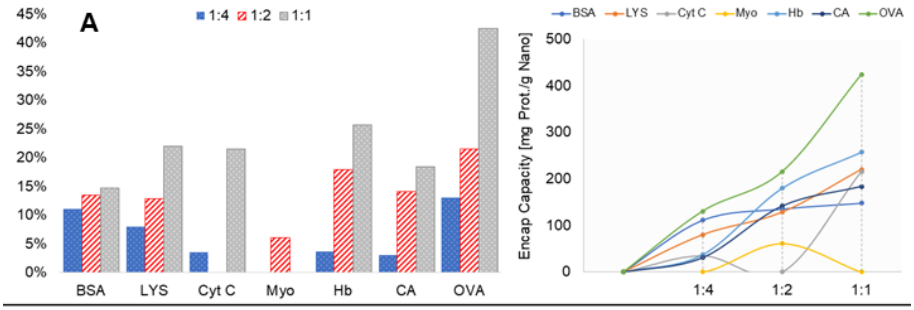

Protein	% L			Loading Capacity (mg/g)		
	1:4	1:2	1:1	1:4	1:2	1:1
BSA	11%	14%	15%	111	135	148
LYS	8%	13%	22%	80	128	220
CYT C	4%	0%	22%	35	0	216
MYO	0%	6%	0%	0	61	0
HEM	4%	18%	26%	37	180	258
CA	3%	14%	18%	31	142	184
OVAL	13%	22%	42%	131	216	425

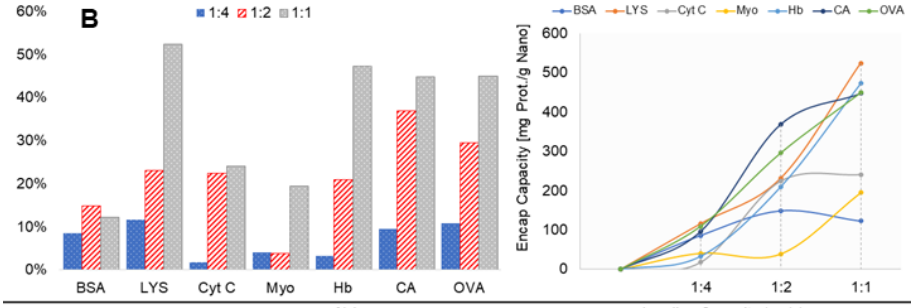

Protein	% L			Loading Capacity (mg/g)		
	1:4	1:2	1:1	1:4	1:2	1:1
BSA	9%	15%	12%	86	149	123
LYS	12%	23%	52%	116	232	525
CYT C	2%	22%	24%	18	225	242
MYO	4%	4%	20%	41	39	195
HEM	3%	21%	47%	33	210	474
CA	10%	37%	45%	96	369	448
OVAL	11%	30%	45%	109	296	450

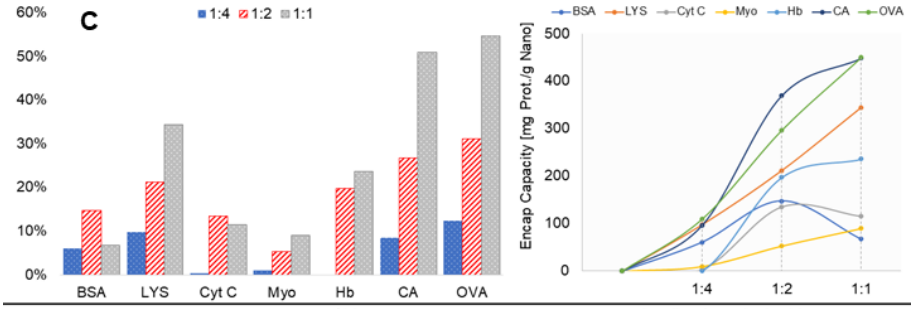

Protein	% L			Loading Capacity (mg/g)		
	1:4	1:2	1:1	1:4	1:2	1:1
BSA	6%	15%	7%	61	147	67
LYS	10%	21%	34%	97	211	344
CYT C	0%	13%	12%	3	135	115
MYO	1%	5%	9%	9	53	90
HEM	0%	20%	24%	0	197	236
CA	9%	27%	51%	85	266	508
OVAL	12%	31%	55%	123	311	546

Figure AIV.1 | % L (left) and loading capacities (right) of all 2 h incubations on (A) SBA-16 T2 blank, (B) RhNHS@SBA T3 and (C) RhISO@SBA T3 samples, for Protein : Particle wt. ratios of 1:4, 1:2 and 1:1; after Bradford assay quantification, in PBS 7.4.

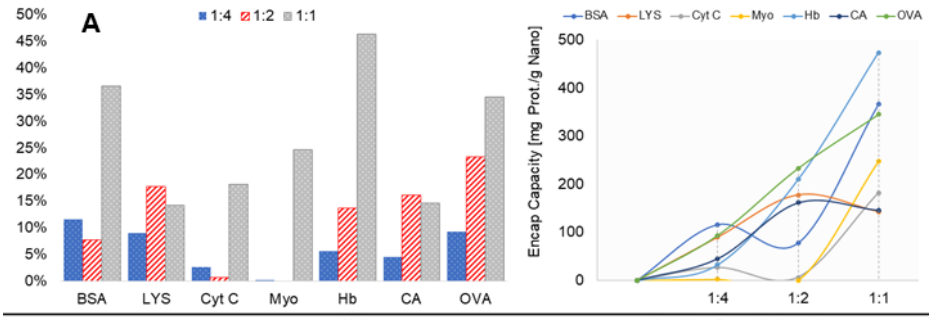

Protein	% L			Loading Capacity (mg/g)		
	1:4	1:2	1:1	1:4	1:2	1:1
BSA	9%	18%	14%	90	178	143
LYS	3%	1%	18%	27	7	182
CYT C	0%	0%	25%	2	0	247
MYO	6%	14%	46%	56	137	464
HEM	4%	16%	15%	45	162	146
CA	9%	23%	35%	93	233	346
OVAL	0%	0%	0%	0	0	0

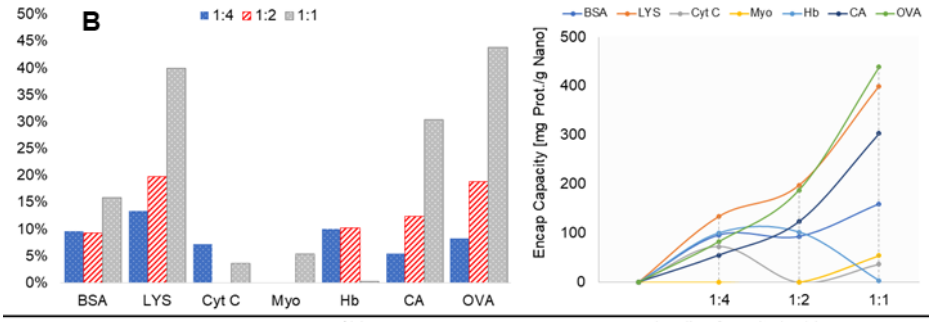

Protein	% L			Loading Capacity (mg/g)		
	1:4	1:2	1:1	1:4	1:2	1:1
BSA	10%	9%	16%	96	93	159
LYS	13%	20%	40%	134	197	399
CYT C	7%	0%	4%	72	0	36
MYO	0%	0%	5%	0	0	54
HEM	10%	10%	0%	100	102	3
CA	6%	12%	30%	55	124	303
OVAL	8%	19%	44%	83	188	439

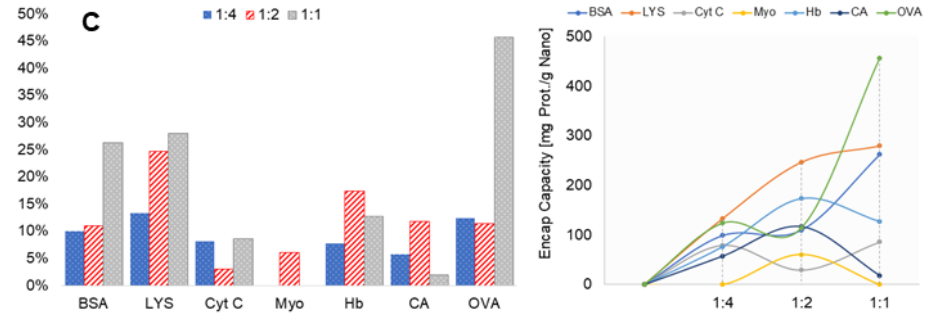

Protein	% L			Loading Capacity (mg/g)		
	1:4	1:2	1:1	1:4	1:2	1:1
BSA	10%	11%	26%	99	110	262
LYS	13%	25%	28%	133	247	280
CYT C	8%	3%	9%	81	29	86
MYO	0%	6%	0%	0	61	0
HEM	8%	17%	13%	77	173	127
CA	6%	12%	2%	58	118	19
OVAL	12%	11%	46%	124	114	456

Figure AIV.2 | % L (left) and loading capacities (right) of all 2 h incubations on (A) SBA-16 T2 blank, (B) RhNHS@SBA T3 and (C) RhISO@SBA T3 samples, for Protein : Particle wt. ratios of 1:4, 1:2 and 1:1; after Bradford assay quantification, in PBS 7.4.

Table AIV.1 | Amino Acids (AA) and NH_2 residues distribution per model protein. Data from UniProt [161]

AA	NH_2 residues/ AA	Bovine Serum Albumin (BSA)			Lysozyme (LYS)			Cytochrome C (Cyt C)			Myoglobin (Myo)			Heamoglobine (Hb)			Carbonic Anhydrase (CA)			Ovalbumin (OVA)		
		Num. AA	% AA	Num. NH_2 residues	Num. AA	% AA	Num. NH_2 residues	Num. AA	% AA	Num. NH_2 residues	Num. AA	% AA	Num. NH_2 residues	Num. AA	% AA	Num. NH_2 residues	Num. AA	% AA	Num. NH_2 residues	Num. AA	% AA	Num. NH_2 residues
Ala	1	48	7.9%	48	14	9.5%	14	6	5.7%	6	15	9.7%	15	15	10.2%	15	21	8.0%	21	35	9.1%	35
Arg	4	26	4.3%	104	12	8.2%	48	2	1.9%	8	2	1.3%	8	3	2.0%	12	8	3.1%	32	15	3.9%	60
Asn	2	14	2.3%	28	14	9.5%	28	5	4.8%	10	2	1.3%	4	6	4.1%	12	18	6.9%	36	17	4.4%	34
Asp	2	40	6.6%	80	7	4.8%	14	3	2.9%	6	8	5.2%	16	7	4.8%	14	15	5.7%	30	14	3.6%	28
Cys	1	35	5.8%	35	9	6.1%	9	2	1.9%	2	0	0.0%	0	2	1.4%	2	1	0.4%	1	6	1.6%	6
Gln	2	20	3.3%	40	3	2.0%	6	3	2.9%	6	6	3.9%	12	3	2.0%	6	9	3.4%	18	15	3.9%	30
Glu	1	59	9.7%	59	2	1.4%	2	9	8.6%	9	13	8.4%	13	8	5.4%	8	13	5.0%	13	33	8.5%	33
Gly	1	17	2.8%	17	13	8.8%	13	12	11.4%	12	15	9.7%	15	13	8.8%	13	17	6.5%	17	19	4.9%	19
His	3	17	2.8%	51	1	0.7%	3	3	2.9%	9	11	7.1%	33	9	6.1%	27	11	4.2%	33	7	1.8%	21
Ile	1	15	2.5%	15	7	4.8%	7	6	5.7%	6	9	5.8%	9	0	0.0%	0	10	3.8%	10	25	6.5%	25
Leu	1	65	10.7%	65	15	10.2 %	15	6	5.7%	6	17	11.0 %	17	18	12.2%	18	24	9.2%	24	32	8.3%	32
Lys	2	60	9.9%	120	6	4.1%	12	19	18.1%	38	19	12.3 %	38	11	7.5%	22	18	6.9%	36	20	5.2%	40
Met	1	5	0.8%	5	3	2.0%	3	3	2.9%	3	3	1.9%	3	2	1.4%	2	1	0.4%	1	17	4.4%	17
Phe	1	30	4.9%	30	4	2.7%	4	4	3.8%	4	7	4.5%	7	8	5.4%	8	11	4.2%	11	20	5.2%	20
Pro	1	28	4.6%	28	3	2.0%	3	4	3.8%	4	4	2.6%	4	7	4.8%	7	19	7.3%	19	14	3.6%	14
Ser	1	32	5.3%	32	11	7.5%	11	0	0.0%	0	5	3.2%	5	5	3.4%	5	26	10.0%	26	38	9.8%	38
Thr	1	34	5.6%	34	7	4.8%	7	10	9.5%	10	7	4.5%	7	7	4.8%	7	9	3.4%	9	15	3.9%	15
Trp	2	3	0.5%	6	6	4.1%	12	1	1.0%	2	2	1.3%	4	2	1.4%	4	6	2.3%	12	3	0.8%	6
Tyr	1	21	3.5%	21	3	2.0%	3	4	3.8%	4	2	1.3%	2	3	2.0%	3	7	2.7%	7	10	2.6%	10
Val	1	38	6.3%	38	7	4.8%	7	3	2.9%	3	7	4.5%	7	18	12.2%	18	17	6.5%	17	31	8.0%	31
Pyl	0	0	0.0%	0	0	0.0%	0	0	0.0%	0	0	0.0%	0	0	0.0%	0	0	0.0%	0	0	0.0%	0
Sec	0	0	0.0%	0	0	0.0%	0	0	0.0%	0	0	0.0%	0	0	0.0%	0	0	0.0%	0	0	0.0%	0
Total AA		607			147			105			154			147			261			386		
Total NH_2 residues		856			221			148			219			203			373			514		
FW		69293			16239			11833			17083			15998			28822			42881		
Total negatively charged residues (Asp + Glu):		99			9			12			21			15			28			47		
Total positively charged residues (Arg + Lys):		86			18			21			21			14			26			35		

Table AIV.2 | Chosen set of proteins for further extraction trials and their correspondent properties (ZP – Zeta Potential; Mob – Mobility; Cond – Conductivity).

Ratio	Sample	ZP (mV)	σ (mV)	Mob (μmcm/Vs)	Cond (mS/cm)
1 : 4 Ratio	RhISO@SBA T1 HEM 1:4 30 min	-23.6	0.7	-1.8	0.7
	RhISO@SBA T1 HEM 1:4 2 h	-33.4	0.9	-2.6	0.2
	RhISO@SBA T1 CA 1:4 30 min	-33.3	1.0	-2.6	0.4
	RhISO@SBA T1 CA 1:4 2 h	-32.4	1.2	-2.5	0.3
	RhNHS@SBA T1 CA 1:4 30 min	-34.6	0.7	-2.7	0.3
	RhNHS@SBA T1 CA 1:4 2 h	-30.9	0.3	-2.4	0.2
	SBA T1 LYS 1:4 30 min	-33.8	1.1	-2.6	0.3
	SBA T1 LYS 1:4 2 h	-35.8	0.5	-2.8	0.2
	SBA T1 HEM 1:4 2 h	-38.1	0.8	-3.0	0.3
	SBA T1 HEM 1:4 2 h	-37.9	1.8	-3.0	0.3
1 : 2 Ratio	RhISO@SBA T1 LYS 1:2 30 min	-37.7	3.2	-3.0	0.2
	RhISO@SBA T1 LYS 1:2 2 h	-14.0	0.8	-1.1	0.3
	RhNHS@SBA T1 MYO 1:2 30 min	-26.9	0.9	-2.1	0.7
	RhNHS@SBA T1 MYO 1:2 2 h	-32.8	0.2	-2.6	0.3
	RhNHS@SBA T1 HEM 1:2 30 min	-20.1	1.4	-1.6	0.5
	RhNHS@SBA T1 HEM 1:2 2 h	-32.3	0.3	-2.5	0.8

	RhNHS@SBA T1 CA 1:2 30 min	-26.5	1.3	-2.1	0.6
	RhNHS@SBA T1 CA 1:2 2 h	-36.1	2.0	-2.8	0.4
	RhNHS@SBA T1 OVAL 1:2 30 min	-30.7	1.0	-2.4	0.3
	RhNHS@SBA T1 OVAL 1:2 2 h	-32.4	1.0	-2.5	0.4
	SBA T1 LYS 1:2 30 min	-30.5	0.5	-2.4	0.2
	SBA T1 LYS 1:2 2 h	-5.6	0.6	-0.4	0.2
1 : 1 Ratio	RhISO@SBA T1 BSA 1:1 30 min	-28.3	0.8	-2.2	0.3
	RhISO@SBA T1 BSA 1:1 2 h	-35.5	0.6	-2.8	0.2
	RhISO@SBA T1 LYS 1:1 30 min	-12.0	1.2	-0.9	0.2
	RhISO@SBA T1 LYS 1:1 2 h	-4.9	0.9	-0.4	0.2
	RhNHS@SBA T1 BSA 1:1 30 min	-29.0	0.3	-2.3	0.2
	RhNHS@SBA T1 BSA 1:1 2 h	-30.5	1.1	-2.4	0.3
	RhNHS@SBA T1 LYS 1:1 30 min	-40.4	0.9	-3.2	0.1
	RhNHS@SBA T1 LYS 1:1 2 h	-37.1	0.8	-2.9	0.2
	SBA T1 BSA 1:1 30 min	-30.1	1.0	-2.4	0.2
	SBA T1 BSA 1:1 2 h	-29.2	1.3	-2.3	0.1
	SBA T1 LYS 1:1 30 min	-36.7	0.9	-2.9	0.2
	SBA T1 LYS 1:1 2 h	-37.5	0.9	-2.9	0.2

Annex V

Stock Solutions

The preparation of each stock solution (solution I, solution II, solution III, running buffer, 10% APS, sample (Laemmli SDS-PAGE) 1D buffer solution and staining solution Coomassie R-250) is thoroughly described in Table AV.2, except for 10% SDS solution that was diluted from an initial 20% SDS stock solution.

With all stock solutions prepared, the formulation of both stacking and running gel is detailed in Table AV.1 Note that, compositions (in mL and µL) on Table correspond to the preparation of two 4% acrylamide stacking gels and two 12% of acrylamide running gels.

Table AV.1 | Volumetric composition of a 4 mL monomer solution for stacking gel and a 10 mL monomer solution for running gel.

Stock Solution	**Stacking Gel**	**Running Gel**	
% acrylamide	4	12	
Solution I	-	2.5	mL
Solution II	1	-	
Solution III (acrylamide/bisacrylamide) (37.5:1)	0.52	4	
SDS 10%	0.04	0.1	
H2O Milli-Q	2.48	3.4	
APS 10 %	30	70	µL
TMED	2	5	

Gel Cassette Preparation

With all Mini-PROTEAN® Tetra Cell components neatly washed (with deionised water) and assembled, we proceeded to the preparation of the running gel monomer solution. The solution was smoothly introduced in the cassette apparatus and immediately overlaid with a 50% (v/v) butanol / 5% SDS solution, to prevent mixing with air. Polymerisation of the running gel lasted up to 30 minutes.

After removing both butanol / SDS solution and post-polymerisation formed water, the already prepared stacking gel monomer solution was introduced over the running gel interface and let polymerize. A comb, with desired wells' dimensions, was also introduced onto the cassette apparatus at the same time (in this case, a 10-welled comb of 10 mm each was chosen). After stacking gel polymerisation, the comb was gently removed and all wells rinsed with deionised water.

Table AV.2 | Stocks solution preparation table

Solution	Reagents	Quantity	Comments
Solution I (running gel)	Tris Base	27.23 g	1.5M Tris-HCl, pH = 8.8
	HCl conc.	until pH 8.8	
	H_2O	until 150 ml	
Solution II (stacking gel)	Tris Base	6.06 g	0.5M Tris-HCl, pH 6.8
	HCl conc.	until pH 6.8	
	H_2O	until 100 ml	
10% SDS	SDS	10 g	-
	H_2O	until 100 ml	
10% APS	Ammonium persulphate	0.1 g	-
	H_2O	until 1 ml	
Running buffer (Tris-glycine)	Tris base	30.3 g	pH = 8.3
	Glycine	144.1 g	
	SDS	10 g	Dilute 1: 10 before use
	H_2O	until 1000 ml	
Sample buffer (SDS-PAGE)	Solution II	1.25 ml	Store at -20ºC
	10% SDS	2 ml	
	β-mercaptoethanol	0.5 ml	Add 1:1 to protein mixture
	Glycerol	2.5 ml	
	Bromophenol blue (0.5% w/v)	0.2 ml	
	H_2O	3.55 ml	
Staining solution Coomassie R-250	Coomassie Blue R-250	0.25 g	0.1% Coomassie Blue R-250
	Glacial acetic acid	12.5 ml	5% Glacial acetic acid
	Methanol	75 ml	30% Methanol
	H_2O	until 250 mL	
Distaining solution I	Glacial acetic acid	50 ml	5% Glacial acetic acid
	Methanol	300 ml	30% Methanol
	H_2O	until 1000 ml	
Distaining solution II	Glacial acetic acid	35 ml	5% Glacial acetic acid
	Methanol	25 ml	5% Methanol
	H_2O	until 500 ml	

Annex VI

BRADFORD ASSAY USING A 96-WELL PLATE

1. REAGENTS AND STOCK SOLUTIONS

Prepare a stock solution I of BSA (2 mg/mL in MQ-water, weight 2 mg of BSA and add 1mL of water).

From the stock solution I (2 mg/mL BSA) take 25 µL and add 475 µL of MQ-water in order to obtain a BSA solution of 100 µg/mL (Stock solution II). Prepare aliquots of the stock solution II and store the solution at -20ºC.

Calibration Curve:

Conc. µg/mL	Volume (µL) of BSA 100 µg/mL	Volume (µL) of H_2O
0	0	400
1	4	396
5	20	380
10	40	360
15	60	340
20	80	320
25	100	300

Using an ELISA plate prepare the calibration curve (at least in duplicates) by loading 150 µL of the solution prepared according to the table 1 and 150 µL of Bradford reagent.

Preparation of the unknown samples: For protein samples with unknown concentrations, it may be necessary to prepare a dilution scheme to ensure the concentration is within the linear range of 5–20 µg/ml. Please have in mind that buffers can affect the performance of the Bradford assay. For example Bradford assay is compatible with Urea lower than 3M. For further information please refer to Technical bulletin from Sigma ref. B6916.

To each well being used, add 150 µL of the sample (appropriate dilution) and 150µL of the Bradford Reagent and mix on a microplate-shaker for ~30 seconds. Let the samples incubate at room temperature for 20 minutes.

Then measure the absorbance at 590nm. The protein-dye complex is stable up to 60 minutes. The absorbance of the samples must be recorded before the 60-minute time limit and within 10 minutes of each other.

Plot the net absorbance vs. the protein concentration of each standard.

Determine the protein concentration of the unknown sample(s) by comparing the ABS values against the standard curve.

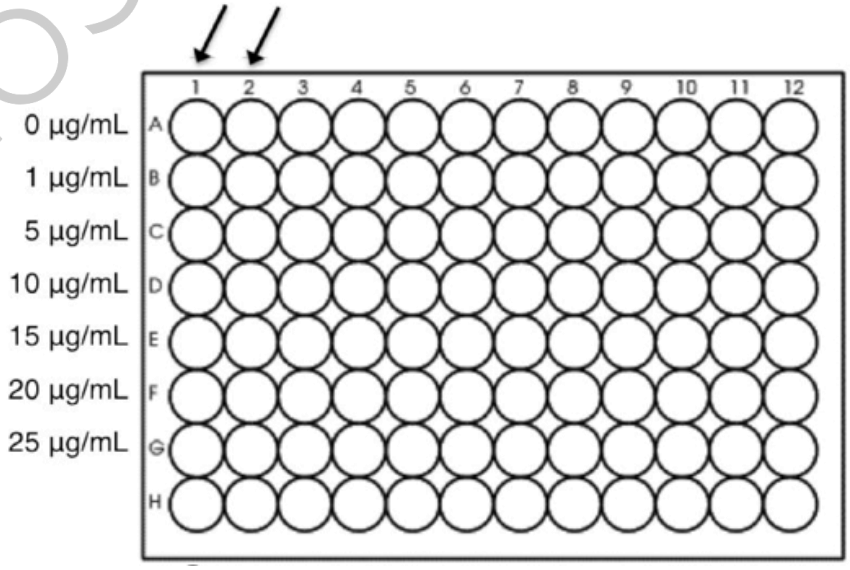

BioScope Research Team **Date: 2012.08.18 Version 2.1**

Written by: H.M.Santos

Approved by: J.L.Capelo